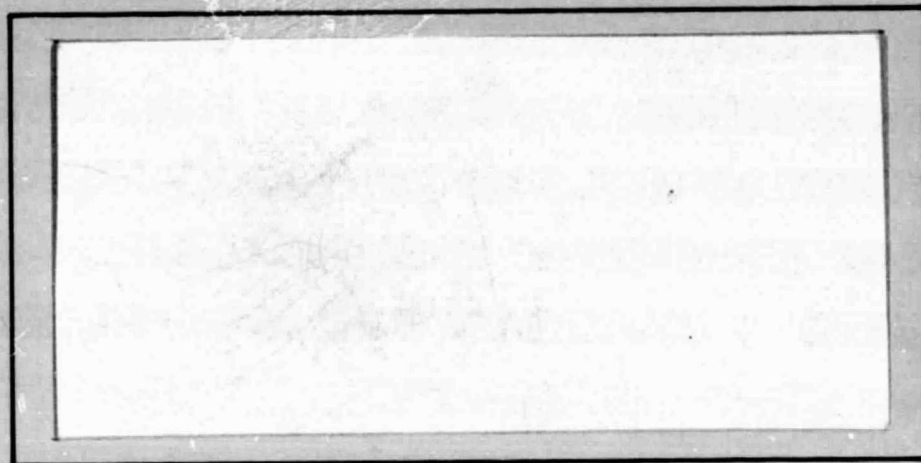


N O T I C E

THIS DOCUMENT HAS BEEN REPRODUCED FROM
MICROFICHE. ALTHOUGH IT IS RECOGNIZED THAT
CERTAIN PORTIONS ARE ILLEGIBLE, IT IS BEING RELEASED
IN THE INTEREST OF MAKING AVAILABLE AS MUCH
INFORMATION AS POSSIBLE

DRA



science Applications, INC.

(NASA-CR-164784) PLANETARY RADAR STUDIES

N82-10972

Final Report (Planetary Science Inst.)

157 p HC A08/MF A01

CSSL 03B

Unclas

G3/91 15035



FINAL REPORT
PLANETARY RADAR STUDIES

NASW3383

SAI 1-142-078-S1

30 April 1981

T.W. Thompson (Principal Investigator)

J.A. Cutts (Co-Investigator)

Planetary Science Institute
Science Applications, Inc.
283 South Lake Avenue
Suite 218
Pasadena, CA 91101
(213) 449-4955

	<u>PAGE</u>
INTRODUCTION.....	1
TASK I: Radar Signatures of Lunar and Venus Craters.....	2
TASK II: High Resolution Radar Mapping of the Moon.....	7
SUMMARY.....	13
ACKNOWLEDGEMENTS.....	14
FIGURE 3.1: 70cm Radar Map Data Flow.....	11
TABLE 3.1: Arecibo Moon Opportunities 02-14 May 1981.....	9
TABLE 3.2: Arecibo Data, December 1978 Observations.....	9
APPENDIX A: Comparison of Radar Images of Craters on Venus and the Moon: Evidence for a Steady-State Venus Crater Population, J.A. Cutts, T.W. Thompson and B.H. Lewis (Manuscript submitted to ICARUS)	
APPENDIX B: Lunar Craters with Radar Bright Ejecta, T.W. Thompson, S.H. Zisk, R.W. Shorthill, P.H. Schultz and J.A. Cutts (Revised manuscript accepted for publication in ICARUS)	
APPENDIX C: Infrared and Radar Signatures of Lunar Craters: Implications about Crater Evolution, T.W. Thompson, J.A. Cutts, R.W. Shorthill and S.H. Zisk (Reprint from Proc. of the Conf. on the Lunar Highlands Crust, Pergamon Press)	
APPENDIX D: DPS and LPSC Meeting Abstracts	
APPENDIX E: Infrared-Radar Crater Catalog on SAI's DEC-10 Computer	

INTRODUCTION

A proposal entitled "Planetary Radar Studies: Venus Crater Signatures and High Resolution Lunar Maps" was submitted to NASA's Lunar and Planetary Program on 07 August 1979. This proposal was accepted by the LPRP peer review and was funded for one year starting on 01 May 1980. This is the Final Report on this effort. The work described here was divided into the following tasks:

TASK 1: Radar Signatures of Lunar and Venusian Craters

Generate a catalog of lunar and radar anomalies to provide a base for comparison with Venusian radar images; investigate the relations between lunar radar anomalies and regolith processes; form a consortium to compare lunar and Venusian radar images of craters.

TASK 2: Generation of 70cm Wavelength Radar Maps

Obtain a limb-to-limb calibration of 70cm lunar radar echoes; obtain six high resolution radar maps of the lunar surface using the 430MHz radar at the Arecibo Observatory.

Current work is based upon three previous studies.

NASA contract NASW 3117, Lunar Megaregolith Properties from Remote Sensing Data, was completed in Oct. 1978 and provided the funds which generated the catalog of 1310 infrared and radar craters. Results of this study were published in The Moon and the Planets. NASA Contract NASW 3205, Lunar Radar Backscatter Studies, was completed in October 1979

and provided the funds which supported Arecibo radar observations in December 1978. These observations provide a valuable data base for generation of computer software for routine radar mapping of the lunar surface under current funding. Lastly, the proposer was a Visiting Scientist at the Lunar and Planetary Institute (LPI) for five weeks during the spring of 1980. This appointment was part of a joint effort with Richard W. Shorthill (University of Utah Research Institute) and Peter H. Schultz (LPI) and yielded the manuscript on Lunar Craters with Radar Bright Ejecta, which has been accepted for publication in ICARUS. In addition to these past efforts, a continuation of this work was proposed to NASA's Lunar and Planetary program in August 1980. This was accepted and will provide a continuation to the work described here.

With this history of these past efforts, we now describe the progress on the two tasks mentioned above. Sections I and II describe Tasks I and II respectively, while all work is summarized in Section III.

TASK I: Radar Signatures of Lunar and Venus Craters

Progress on this task has proceeded in a number of study areas. The study of the evolution of Venusian craters was the subject of a manuscript (See Appendix A) which has been accepted for publication in Icarus. A second manuscript on lunar craters with radar bright ejecta was also accepted for publication (Appendix B) in Icarus. This complements a paper on the evolution of the infrared and radar signatures of lunar crater interiors recently published in the Proceedings of the Lunar Highland Crust Conference (see Appendix C). These studies of Venus and lunar craters were also presented at the Division of Planetary Sciences (DPS) meeting in Tucson, Arizona in October 1980 and at the 12th Lunar and Planetary Science Conference (LPSC) in Houston, Texas in March 1981 (see abstracts in Appendix D). Our paper on the Venusian craters at the DPS meeting was one of only four papers which discussed Venusian surface properties at the meeting. In addition to these scientific publications, two infrared/radar crater catalogs were compiled on Science Application's DEC-10 computer in La Jolla (see Appendix E).

One important aspect of our work is understanding how the radar signatures of craters evolve with geologic time. The evolution of the radar signatures of Venus craters may have analogies to those of lunar craters. The evolution of lunar craters appears to be driven in large part by meteoritic

bombardment, which gardens the lunar surface and destroys the rocks which create enhanced radar backscatter. This evolution is size dependent as smaller craters lose their signatures faster than larger craters. This is illustrated in the lunar case where size-frequency distributions of radar-bright craters and visual craters are compared. The distributions of radar-bright craters deviate from production distributions derived from surface photography.

Venus crater populations also deviate from a production distribution, based upon Arecibo earth-based radar data published by Don Campbell and Barbara Burns of Cornell. Gardening by meteroids is not applicable for the Venus case because of the thick Venus atmosphere. An alternate crater erasure process on Venus may be deposition of dust layers. Smaller craters will have smaller rubble which is buried sooner than larger rubble associated with larger craters. A possible source of these dust layers may be the insertion of fine grained debris into the atmosphere by large impacts equivalent to those which formed the larger craters on the moon. To study this, we have simulated Venus impacts with a Monte Carlo computer model where the impactors would have a lunar production curve if no atmosphere existed. In addition, we assumed that each impact would inject a small percentage of the ejecta into the atmosphere and subsequently deposit this, a fine-particle dust layer. This model yields

a good fit between the predicted and observed populations of Venus as described further in Appendix A.

The study of Venus cratering can be accomplished only via the interpretation of radar images. This, in turn, will rely in part upon the interpretation of lunar craters, where the radar signatures are complemented by a host of observables at other wavelengths and a well understood body of photogeological interpretation. Since the interpretation of the lunar radar signatures has a number of elements common with the eventual interpretation of the VOIR images from Venus, the continued refinement of the lunar radar interpretation is needed. We have made progress here.

Recent study of the radar signatures of lunar craters has taken two somewhat different paths - crater interiors and crater exteriors. The recent study of crater interiors was just published as an article in The Proceedings of Lunar Highlands Crust Conference. (A reprint of that article is included here as Appendix C.) We also conducted a study of crater ejecta with strong 3.8cm radar enhancements. (This, as mentioned above, was initiated under the auspices of the Visiting Scientist Program at the Lunar and Planetary Institute and it was continued under the current funding effort.) Our progress here is represented by a manuscript which was just accepted for publication in ICARUS. (See Appendix B.)

Continued study of the radar signatures of lunar craters will be enhanced by our computer cataloging effort. In particular, the two catalogs described in Appendix E have been installed on the disk data sets of SAI's DEC-10 computer in La Jolla, California. That computer is accessible via a telephone in our Pasadena office.

In summary, we have made progress in study of both Venusian and lunar craters via their radar signatures. These have resulted in the scientific papers and meeting presentations given in the Appendices A through D. Much of the scientific data for these papers resides as two infrared/radar catalogs described in detail in Appendix E.

TASK II: High Resolution Radar Mapping of the Moon

The long range goal of this task is to produce new 70cm radar maps of the moon with substantial improvement in resolution and radarmetric control over the existing 70cm radar data, obtained originally in the late 1960's. This is a multi-year effort, where the current funding will emphasize a complete data reduction of test data for Mare Serenitatis and the Plato area which was acquired in December 1978. In addition, follow-on funding will allow observations in May 1981 which will emphasize a limb-to-limb calibration and high resolution mapping in opposite polarizations of six lunar areas. All of the 70cm data will come from radar observations at the Arecibo Observatory, Arecibo, Puerto Rico.

Progress in this task has taken two paths. First, acquisition of a new data is being planned for May 1981. A proposal to the Arecibo Observatory for the observing time has been accepted. A few pre-observation tasks, such as ephemeris development, are underway. Second, data from the December 1978 observations of Mare Serenitatis and Plato is currently being analyzed with software on Science Applications' PDP11/70 computer in Sorrento Valley, Calif. This is important since it constructs the computer program library necessary for the eventual reduction of the May 1981 and subsequent data acquisitions.

New radar observations at Arecibo were originally proposed for February 1981. These were postponed until May 1981 for a number of reasons. The equipment at Arecibo has to be upgraded so that an auxillary antenna can receive both senses of circular polarization. That upgrading has not gone as fast as expected; so the observations in May 1981 rather than February 1981 will have a better chance of success. In addition, data reduction on the Dec. 1978 data sets for Mare Serenitatis and Plato has also lagged. Postponing of new observations until May 1981 allowed a few more months to be spent on the current data set. This, we feel, also increases the chances for our success in May 1981. In addition, observations in May will fall at the beginning of new funding on a follow-on effort and much of this follow-on will be devoted to these new observations. (Scheduled observations in May 1981 are given in Table 3.1.)

In addition to acquiring new data, this portion of study has a goal of reducing data from the December 1978 observations of Mare Serenitatis and Plato. A summary of these observations are given in Table 3.2. The production of radar maps from these data requires a number of computer programs; shown in Figure 3.1. The first program (CHKTAPE) processed the raw data to verify that further processing is necessary. These produce the printouts shown in the first Quarterly Report.

ARECIBO MOON
 OPPORTUNITIES
 02-14 MAY 1981

TABLE 3.1

DAY	TRANSIT GMT	TRANSIT AST	DECLINATION (NORTH)
SAT 02 May 81	15:00	11:00	3°15'*
SUN 03 May 81	16:00	12:00	8°45'
MON 04 May 81	17:00	13:00	13°35'*
TUE 05 May 81	18:00	14:00	17°25'
WED 06 May 81	19:00	15:00	19°55'*
THU 07 May 81	20:00	16:00	20°55'*
FRI 08 May 81	21:00	17:00	20°30'*
SAT 09 May 81	22:00	18:00	18°40'*
SUN 10 May 81	22:45	18:30	16°00'*
MON 11 May 81	23:20	19:30	12°30'*
TUE 12 May 81	24:15	20:15	8°25'
WED 13 May 81	25:00	21:00	4°15'

*Scheduled Observations

TABLE 3.2: SUMMARY OF DECEMBER 1978 70cm RADAR
OBSERVATIONS OF THE MOON

DATE	TARGET	NUMBER OF MAG TAPES	NUMBER OF SPECTRA
16 Dec. 78	MARE SERENITATIS	2	36
18 Dec. 78	PLATO AREA	5	58

The second processing program (GETSDISK) converts raw tape data to a disk data set for further processing. A check program, CHKSDISK, verifies that the disk data is OK before further processing is attempted. The next major program, GETSDOP, produces a raw delay-Doppler map of echo power by spectral analysis of raw time samples stored on the disk data set. Program GETSDOP produces a magnetic tape, which is verified by a check program, CHKSDOPT.

The next major program, GETSNORM, processes the raw delay-Doppler map of echo power to produce a normalized map of lunar echo power. In particular, this echo normalization includes; (1) a subtraction of background noise, (2) echo power adjustment to account for expected power differences from the moon's average scattering behavior, and (3) echo power adjustments to account for antenna gain and scattering area variations inherent in the geometry of the radar observations. Echo variations after these adjustments must arise from differences in the physical properties of the lunar surface. All of the computer programs shown in Figure 3.1 exist and have been applied to the Mare Serenitatis data from the Dec. 1978 observations.

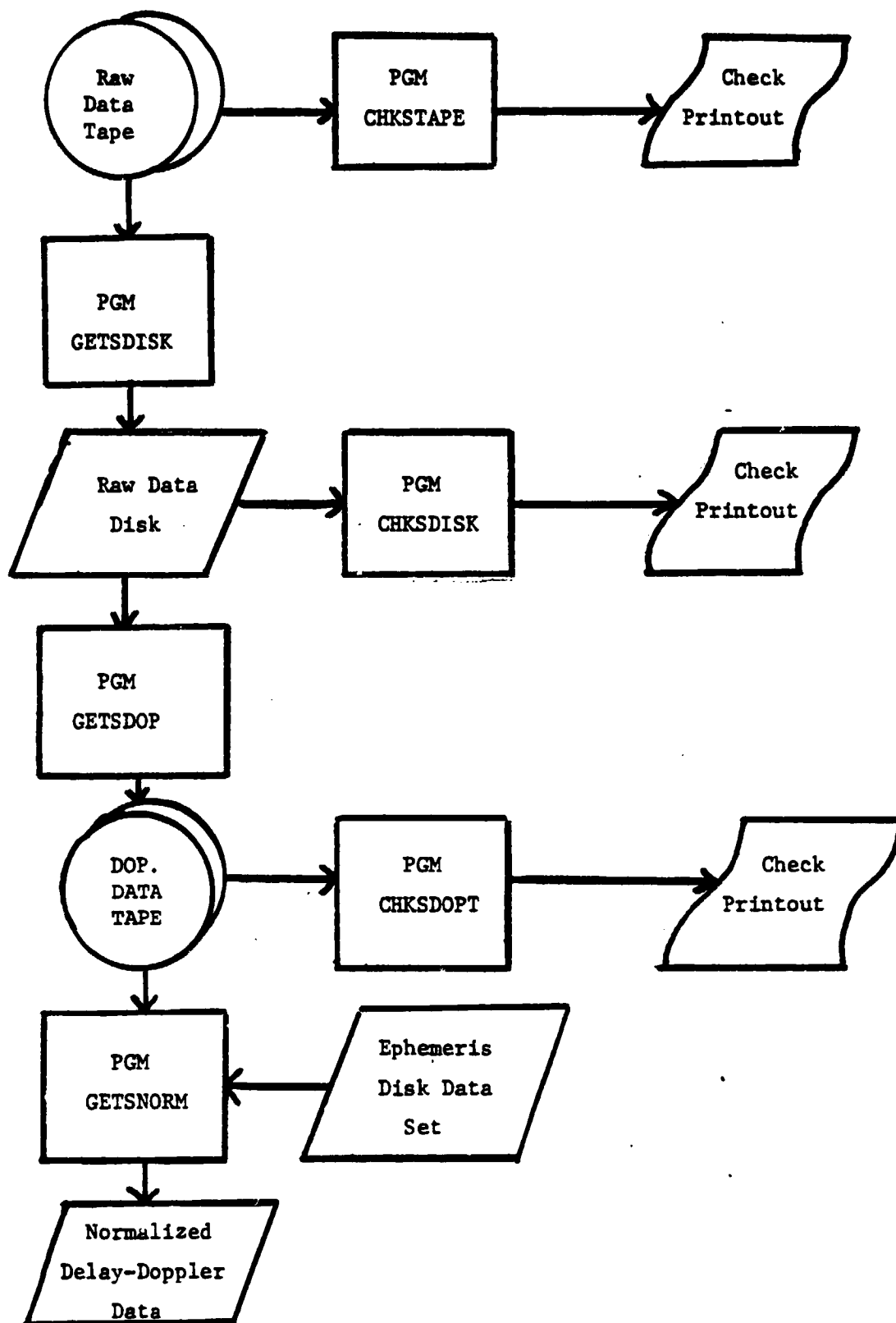


FIGURE 3.1: Data Flow for 70cm Radar Map Production from Arecibo data.

In summary, we have generated the computer software needed for generating 70cm radar maps from Arecibo radar data. We have applied these programs to the Mare Serenitatis data set. In addition, we have firm plans for new observations in May 1981 during the first of the month of the extension of our current contract.

SUMMARY

(I) Progress:

Task 1: Radar Signatures of Lunar and Venus Craters

- (1) Lunar Crater Evolution paper published in the Proceedings of the Lunar Highland Crust
- (2) Venus Crater paper presented at DPS meeting
- (3) Lunar Crater paper presented at the DPS and LPSC meetings
- (4) Manuscript on Lunar Craters with Radar Bright Ejecta accepted for publication in ICARUS
- (5) Manuscript on a comparison of radar images of Venusian and lunar craters accepted by ICARUS
- (6) Two crater catalogs converted to Disk Data Sets on SAI's DEC-10 computer

Task 2: Generation of 70cm Wavelength Radar Maps

- (7) Generation of Radar Map Production Programs for analysis of the Dec. 1978 data of Plato and Mare Serenitatis
- (8) Application of these computer programs to the Mare Serenitatis data from Dec. 1978
- (9) Definition of an observing program at the Arecibo Observatory for May 1981

ACKNOWLEDGEMENTS

Much of the data reduction described in this report would not have happened without the unflagging efforts of Mr. Blake Lewis and Mr. Steve Schlipf. Blake produced the software for the Monte Carlo models in the Venus Crater Study as well as the plotting routines which produced the plots in the Lunar Crater Ejecta paper. Steve Schlipf produced the catalog of craters with radar bright ejecta and thoroughly checked the entries in this catalog against the original data.

APPENDIX A

COMPARISON OF RADAR IMAGES OF
CRATERS ON VENUS AND THE MOON:
EVIDENCE FOR A STEADY-STATE VENUS
RADAR CRATER POPULATION *

James A. Cutts (1)

Thomas W. Thompson (1)

Blake H. Lewis (1)

(2) Planetary Science Institute
Science Applications, Inc.
283 South Lake Avenue, Suite 218
Pasadena, California 91101

For Submittal to:

Icarus

November 1980

13 Figures

2 Tables

Pages

PSI Contribution #142

*Accepted for publication in ICARUS

ABSTRACT

The surface of Venus viewed in Arecibo radar images has a small population of bright ring shaped features. The features are interpreted as the ejecta deposits of impact craters: an enhanced population of blocks or unusual surface roughness which scatters radar signals more effectively than the crater floors or surrounding terrains. The small population of these radar bright ring structures on Venus resembles the population of radar bright haloes associated with the ejecta deposits of young craters on the moon. This suggests that the Venus radar ejecta signatures, like the lunar signatures, have short lifetimes. The lifetime of crater radar signatures on Venus may be controlled by the global precipitation of suspended debris from very large cratering events. This process obliterates contrasts in roughness and blockiness. Other effects of large cratering events such as regional scale eolian disturbances may provide a better explanation of the very low observed crater population at small crater diameters. Depositional and erosional effects associated with cratering may have had a profound influence on the evolution of the Venusian lowlands.

INTRODUCTION

Cratering of planetary surfaces by impacting meteoroidal bodies is a ubiquitous process on those solar system bodies with solid surfaces. Impact craters have been recognized on the earth's surface and photographed on the surfaces of Mercury, Moon, Mars and the satellites of Jupiter and Saturn. In recent years the cloud shrouded surface of Venus has been imaged with radar and circular features have been revealed on the surface of that planet.

In images taken at low radar illumination angles (1° to 8°) with the Goldstone 12.6 cm radar, slopes dictate the magnitude and character of the signal returns and near circular features with inward sloping margins have been recognized and interpreted as impact craters (Rumsey et al., 1976; Saunders and Malin, 1976). In images obtained over a much broader range of illumination angles (10° to 70°) at 12.5 cm by the Arecibo Observatory, a large number of bright ring-shaped features between 20 and 150 km in diameter have been detected and have been tentatively identified as impact craters (Campbell et al., 1976, 1979; Campbell and Burns, 1980).

Abundances of the annular features seen in the Arecibo images are much lower than the photogeologically determined abundances of impact craters on many planetary surfaces of intermediate age such as the lunar maria and the martian plains. This could be accounted for by very active geologic processes on

Venus resurfacing the planet comparatively rapidly, and Campbell and Burns (1980) cite a representative age of 600 million years for the Venusian surface. However, Saunders and Malin (1976) report very dense crater populations comparable to those in the most heavily cratered areas of the Moon and Mars using the Goldstone radar data whose response to crater rim slopes is like that of visual images under low sun conditions. Moreover, Schaber and Boyce (1977) also report a population of dark floored impact basins on Venus more dense than that on Moon or Mercury and infer that atmosphere related erosion on Venus has been orders of magnitude lower than on the Earth. These results appear to be quite inconsistent with those of Campbell and Burns (1980).

The comparatively poor resolution of the Arecibo radar data may mean that many of the impact craters present are not seen, so that the age inferred from these data is an underestimate. Another view (Campbell and Burns 1980) is that many of these bright annular features are not craters but volcanoes; this would imply that the age of most of the Venus surface is even less than that cited above. However, these explanations do not exhaust the range of possible interpretations of the data and does not answer the fundamental apparent contradiction of the Goldstone and Arecibo data on crater populations.

The purpose of this paper is to reinterpret the bright annular features in the Arecibo images in the context of some recent investigations of the radar appearance of lunar craters (Thompson et al., 1978; Thompson et al., 1980a; Thompson et al., 1980b). Although the environment of Venus is very different from that of the atmosphereless Moon, the two bodies have at least one important characteristic in common -- a stable crust in which craters have been recorded and preserved. In addition, there is a rich collection of photogeological and thermal infrared observation to supplement 70 cm and 3.8 cm radar observations of lunar craters, permitting a reasonably detailed understanding of the formation and evolution of lunar crater radar signatures.

Our major thesis is that the bright ring shaped features seen in the Arecibo images of Venus contain information about the process of crater formation of Venus and about the rate at which the surface is being modified by depositional or erosional processes. We propose that the bright ring features on the Venus surface are the radar expression of the ejecta deposits of very young craters. Our contention is that the bright ring population have a steady state population established by mutual obliteration of craters.

COMPARISON OF RADAR CHARACTERISTICS
OF LUNAR CRATERS WITH
VENUSIAN BRIGHT ANNULAR FEATURES

In their comparison of the bright ring features in the Arecibo images with the radar signatures of lunar craters, Campbell and Burns (1980) noted that the lack of adequate analysis of craters in the lunar radar data base seriously hindered useful comparisons. Here we consider the Venus observations in light of our own recent investigations of 3.8 cm and 70 cm radar and infrared signatures of lunar craters (Thompson et al., 1980a,b). We also discuss the radar signature from lunar craters in terms of surface properties and inferences drawn about the mechanism of emplacement of ejecta materials by the cratering event.

On the moon, we have divided our studies into analyses of crater floor and interior properties (Thompson et al., 1980a) and properties of the ejecta deposit (Thompson et al., 1980b). No data yet exist for the Moon at 12.6 cm, the wavelength of the Arecibo radar observations. For this reason, we discuss both the 3.8 cm and 70 cm radar observations which bracket the 12.6 cm wavelength of the Venus data. We also consider thermal infrared data, which help to distinguish between roughness and blockiness of the ejecta. These properties are not well discriminated by the radar data alone.

Lunar Crater Floors

The 3.8 cm and 70 cm radar and thermal infrared signatures of the floors of freshly formed lunar craters are found to be significantly enhanced relative to the average properties of either lunar mare or upland surfaces (Thompson et al., 1980a). Studies of the lunar crater population indicate that with increasing exposure time on the lunar surface the radar and infrared signatures fade. The infrared signature is first to go; in small craters ($D < 10$ km) the 3.8 cm signatures follow and finally the 70 cm signatures disappear, but the order of disappearance is reversed in larger craters (Thompson et al., 1980a). The lifetimes of the radar signatures of crater floors are found to be several billion years.

Lunar Crater Ejecta

Freshly formed lunar craters are surrounded by a broad halo of enhanced 3.8 cm radar brightness which can extend to between 10 and 20 crater radii from the crater rim (Thompson et al., 1980b)(Fig. 1). The initial size of the thermal infrared halo is not well defined by the existing data except for craters larger than about 10 km but appears to be slightly smaller than the 3.8 cm halo. The 70 cm halo is very much smaller and extends to less than one crater diameter from the rim. The size and the brightness of each type of halo appears to change with exposure on the lunar surface. These changes are evidently most rapid

for the IR ejecta signature, least so for the 70 cm ejecta signatures, and intermediate for the 3.8 cm ejecta signature. The 3.8 cm signatures disappear much more rapidly for the ejecta deposits (lifetimes 1.3 to 3.3×10^8 years, depending on crater size) than from crater floors (lifetimes $> 10^9$ years). Thompson et al. (1980b) have interpreted these ejecta signatures in terms of an initial population of surface and subsurface rocks and surface roughness associated with the formation of an impact crater ejecta blanket and the subsequent modification of the ejecta blanket by lunar surface processes.

Circular Features on Venus

Circular features on the Venus surface were first seen in the radar images produced by the Goldstone (JPL) system (Rumsey et al., 1974; Goldstein et al., 1976 and 1978). In these images the surface was observed at small incidence angles (less than 6°) and crater like forms appear as bright and dark arcuate patches produced by slope induced changes in the intensity of the backscatter signal. In the Arecibo images acquired at 12.6 cm wavelength with a much higher and broader range of incidence angles, bright annular features enclose areas of darker terrain. These features, which are of principal interest here, are derived from radar maps covering approximately 35% of the surface of Venus, and were acquired at angles of incidence which make a comparison with the lunar 70 cm and 3.8 cm data set most useful.

Thirty three of these features have now been detected (Campbell and Burns, 1980) and tentatively identified as impact craters. An impact crater by their definition is a relatively circular area of low backscatter cross section (dark) surrounded by a high contrast (bright) region of finite extent. At least four resolution cells were required for this identification and at the best resolution obtained the smallest crater detectable was approximately 20 km in diameter. Some features conforming to the above description were not included in the list of 33 "craters." Among these are features in Maxwell Montes at $66^{\circ}\text{N}, 7^{\circ}\text{E}$ and at $24^{\circ}\text{S}, 324^{\circ}\text{W}$ now designated Hathor Mons. Measurements by Pioneer-Venus radar altimeter indicated that these were probably raised volcanic features. No data have been assembled on the number of bright spots which do not have the distinctive annular form of the features characterized above; inspection of moderate quality published maps suggests that such features are present but not abundant.

What is the evidence that the bright ring features characterized by Campbell and Burns are associated with impact craters? At present the evidence is quite indirect and must depend in large part on lunar analogy. Observations of lunar craters at 3.8 cm show distinctive radar highlighting of crater rims. This kind of highlighting is not seen in the Arecibo Venus data but its absence is

not unexpected; Goldstone radar observations at very low incidence angles indicate that the rim slopes of Venus craters (8°) are much smaller than those of lunar craters ($\sim 25^{\circ}$). Unfortunately, no bright ring crater has yet been observed at low radar incidence angles, which might reveal a crater rim and show where that rim is located relative to the bright annulus.

Lacking this definitive evidence we can only proceed cautiously to compare these Venusian bright radar features with the radar signatures of lunar craters. On Venus, as on the moon, we associate the enhanced reflectivity with local excess in surface roughness or blockiness. Bright annular radar features are the exception rather than the rule on the lunar surface. They are only seen in lunar craters whose floors have been embayed with mare materials. An example is shown in Fig. 3: the lunar crater, Plato, near 10°W , 53°N . Such lunar features exhibit radar bright central features, which also appear in some of the Venus images (Fig. 3).

Accepting the lunar features as a Venusian analog would imply that almost all Venusian craters developed a fill of volcanic material soon after their formation. However, there are other interpretations for the dark interiors of the Venusian features. The distinctive form and evolution of most lunar crater signatures: initially bright in floor

and ejecta zone; shrinking comparatively rapidly to the crater rim; and gradually fading with further exposure is a consequence of the greater lifetime of the ejecta floor signature in comparison with the signature of the ejecta zone. If the floor materials either formed as a rock-free smooth deposit or if they evolved to this state more rapidly than the ejecta deposit then the radar signature would either initially be a bright annulus or would evolve rapidly to a bright annulus. So different are the conditions of crater formation and degradation in the thick atmosphere of Venus that neither possibility can be excluded.

On the assumption that the bright ring features are associated with ejecta deposits we have performed comparisons with the signatures of lunar ejecta deposits. Whereas Campbell and Burns (1980) compared the Venus radar halo with the photogeological measure of ejecta deposit size we have used the 3.8 cm and 70 cm radar measurements of lunar craters. Our lunar measurements are referenced to the crater rim diameter as measured most accurately from photographs. For the Venus data we have followed Campbell and Phillips in assuming that the inner margin of the bright halo can be associated with the margin of the crater floor (not the rim) and we have determined a revised crater diameter assuming rim widths typical of large lunar craters. Plotted in Fig. 4 are the

diameters of the bright radar signatures of lunar and Venusian craters.

The Venus halo diameter (D_{Vh}) can be expressed in terms of the diameter of the dark crater interior (D_{Vi}) and bright halo width (W_{Vh}) measured by Campbell and Burns (1980)

$$D_{Vh} = D_{Vi} + 2 W_{Vh} \quad (1)$$

In Fig. 4(c) it is D_{Vi} that is plotted against the halo diameter D_{Vh} . Since D_{Vi} may represent only the width of the crater floor and not the rim-to-rim crater diameter, we have estimated the Venus rim-to-rim crater diameters (D_{Vrr}) using relationships developed by Pike (1977) for lunar craters

$$D_{Li} = 0.187 D_{Lrr}^{1.249} \quad (2)$$

Using an analogous relationship for Venus and ignoring the scaling differences which are complex and difficult to assess, we find approximately that

$$D_{Vrr} = (5.37 D_{Vi})^{0.80} \quad (3)$$

In Fig. 4(a) Venus halo diameter D_{Vh} is plotted against D_{Vrr} calculated from equation (3).

Resolution limits the Venus data to craters of large diameter (>20 km). Because the lifetime of the 3.8 cm radar signatures of lunar crater ejecta deposits is short on the moon, few examples of large lunar craters with bright ejecta deposits appear in Fig. 4. Thus, only a few craters occur in the size range for which we have data on both bodies.

Because of the substantial differences between 3.8 cm and 70 cm halo diameters and the uncertainty in the location of the crater rim in the 12.6 cm Venus images, no significant differences can be discerned between the characteristics of the the two populations. However, no very broad deposits are seen such as those occurring around some of the smaller lunar craters.

Given the much greater gravity on Venus and more importantly the influence of a thick atmosphere, the dynamics of crater ejecta emplacement will be very different on Venus than on the Moon. Comparisons have been made of the effects of atmospheric drag on the range of ejecta particles in the context of interpretations of ejecta deposits (Schultz and Gault, 1979; Settle, 1980; Campbell and Burns, 1980). Except for ejecta particles which are implausibly large and could represent only a fraction of the ejecta deposit these results predict ejecta ranges much shorter than the observed width of Venus ejecta deposits (Fig. 4). It seems most plausible that the Venusian ejecta were deposited as flows perhaps in an analogous fashion to the ejecta deposits of many martian craters (Carr et al., 1977). Without better resolution and a more comprehensive data set it is difficult to draw further conclusions from this data set about ejecta emplacement on Venus. We now proceed to examine the populations of craters with radar bright ejecta deposits on the Venusian surface.

POPULATIONS OF CRATERS WITH RADAR BRIGHT EJECTA

In investigations of the populations of craters with radar bright crater floors and ejecta deposits Thompson et al. (1980a, b) used data on photogeological crater abundances to establish lifetimes for floor and ejecta signatures. For Venus craters, only the populations of craters with radar bright ejecta have been measured (Campbell and Burns, 1980). Here we compare the lunar and Venusian crater populations and attempt to define what type of crater population is being measured in the Arecibo radar images.

Crater populations on planetary surfaces lie somewhere between two extremes: production populations in which the number of craters continue to increase with time and is the total number formed since the surface was created; and steady state populations in which a uniform erosional or depositional process or mutual obliteration destroys old craters as rapidly as new ones are formed. When different criteria are used for crater identification, the same surface may appear to have a production population using one method of crater identification and a steady state population according to another. There is nothing contradictory in this result, of course, and the resulting populations contain complementary information about different processes acting on planetary surfaces.

Lunar Crater Populations

Investigation of the surface of the lunar maria using image data suitable for revealing the topographic character of lunar craters -- circular depressions with raised rims -- indicates that the population of craters of diameter 1 km and larger occupies a small fraction of the surface. Craters of this size and larger are regarded as belonging to a production population; at 100 m and below, craters are more densely packed and mutual obliteration may have set up an equilibrium or steady state situation. On the lunar uplands, photogeological measurements reveal much denser populations at all sizes; whether these are nearer to steady state or production populations is still a subject of controversy (Woronow, 1978).

The 3.8 cm and 70 cm radar (and infrared signatures) of crater floors and ejecta deposits have finite lifetimes to exposure on the surface of the moon. When the age of the surface exceeds that lifetime, so do many of the craters on it and the population of craters with radar bright characteristics assumes the steady state form. The steady state population of craters with radar bright ejecta is compared with the crater population on Oceanus Procellarum in Fig. 5.

Degradation by impacts of meteoritic particles which abrade and fracture rocks exposed at the surface, excavate

other rocks from depth, and coat the regolith with mantles of fine ejecta appears to be a logical explanation for the aging of infrared and radar crater signatures. Precisely why crater floor deposits survive longer than ejecta deposits is unknown but a number of possible explanations have been advanced (Thompson et al., 1980a).

Venus Crater Populations

In Fig. 6, the crater populations on Venus generated from a tabulation published by Campbell and Burns (1980) are compared with the number of craters predicted for 3.2 billion years exposure on the lunar surface using data generated during the Basaltic Volcanism Study Project (1980). The Venus crater population is deficient in small craters, compared to the production population. Atmospheric effects are not believed to be an important influence on crater formation above diameters of 10 km (Tauber and Kirk, 1976). Campbell and Burns (1980) suggest that either Venus has a very young surface or that craters are simply not resolved in the radar data. Neither explanation is very satisfying. The young surface explanation requires either widespread internal activity continuing for 7/8 of the planet's history, then terminating suddenly, or active surface erosional processes which also ended abruptly. Both ideas are ad hoc. The resolution effect explanation also has weaknesses: it does not explain why some craters are clearly recognized and others are not.

A preferred explanation in our view is that the Venus radar crater population seen in the Arecibo images is a steady state population established by competing processes of crater formation and the obliteration of the radar crater signatures. The limited data on topographically expressed craters from the Goldstone images (Saunders and Malin, 1976) which indicate a population comparable to the most heavily cratered parts of the Moon and Mars, suggest that the bright ejecta craters in the Arecibo images are a very small subset of all craters on Venus. Populations of craters with IR, 3.8 cm or 70 cm radar bright interiors on the lunar terra discussed earlier are steady state populations in which the process obliterating the remote sensing signatures is comparatively slow. The populations of craters with IR and radar bright ejecta are steady state on both lunar mare and terra; here the obliteration process is comparatively rapid (Fig. 5). In slope, the Arecibo Venus radar crater population (Fig. 6) resembles the lunar steady state populations (Fig. 5) consistent with the proposition that large craters survive longer than small ones. In magnitude it appears to be somewhat smaller than the lunar steady state populations of craters with bright ejecta deposits suggesting a process operating at a somewhat faster rate.

What process could be responsible for the steady obliteration of radar crater signatures on Venus? Whereas meteoritic gardening is probably the major factor in degrading these signatures on the moon, it is clearly ineffective on Venus where the thick atmosphere shields the surface from meteoritic bombardment. A continuing series of volcanic events or eolian processes cannot be ruled out. Although such continuing processes seem more plausible than an abrupt termination of activity 600 million years ago, an explanation requiring only impact processes would be attractive. Conventional saturation of cratering is obviously out of the question because these populations (Fig. 6) are sparse. An interesting possibility is that suspended particles injected into the atmosphere by large cratering events precipitate from atmospheric suspension and progressively mask the blocky ejecta deposits that render Venus craters visible in the Arecibo radar image (Fig. 7).

We have modelled the effects of this process on the Venus radar crater populations. The volume of material excavated in a cratering event (V_{ej}) can be approximated as:

$$V_{ej} = \pi k' D^3 (1 - f_d) / 8 \quad (4)$$

where k' is the depth-diameter ratio referred to the original surface, D is the crater diameter and f_d is the fractional volume of the crater that is produced by target displacement.

Settle (1979) points out that much of the ejected material in a Venus cratering event will fall back into the transient cavity. Nevertheless, some fraction (f_s) will escape both fallback into the cavity and deposition in the ejecta blanket. Let us assume that the resulting volume of material (V_s) is uniformly precipitated over the surface of Venus.

$$V_s = f_s \cdot V_{ej} \quad (5)$$

$$V_s = \{\pi k' (1-f_d) f_s\} D^3 / 8 \quad (5a)$$

The diameter of the initial crater cavity used here will be larger than the rim -to-rim diameter D_{Vrr} discussed earlier. However, because applications of equation (5a) only involve crude scaling arguments, the difference is not of consequence.

Let us now calculate the steady-state radar crater population on the assumption that crater ejecta deposits disappear from Venus images when the deposit on them exceeds a thickness T . We allow T to be a constant or a function of crater diameter D .

Cratering events in the size range above 10 km were generated with a Monte Carlo simulation, modeling cratering as a Poisson process, with crater diameters determined by the cumulative distribution (Hartmann, 1977),

$$\text{Probability (Diameter} \geq D) = (D_{\min}/D)^2 \quad (6)$$

where D_{\min} was taken to be 10 km. The material deposited planetwide by each event was calculated and the crater diameter, time of formation of the crater and the thickness of deposition stored. After

each cratering event, the thickness of the deposit on each crater already in the file was updated. The population of craters at the end of the experiment that was visible to radar was estimated using a variety of assumptions about the thickness of deposit needed to obscure a crater of a given diameter.

In Fig. 8 we illustrate the amount of deposition as a function of time for three Monte Carlo model runs. For each run the deposition history was calculated for two functional dependences between V_g and crater diameter: D-squared scaling and a D-cubed scaling.

The quantity in parentheses in Equation 5a would depend on D^{-1} in the first case and be constant in the second case for these overall relationships to hold. In neither case is the deposition rate uniform but, for the D-cubed law, the deviation is much more conspicuous because a few large events dominate the depositional history.

In Fig. 9 we contrast the observed population of radar craters on Venus with the total number of craters produced in each run ignoring any crater erasure process. The slope of the observed populations is quite different and $\log R$ is lower than the Monte Carlo model population for $D < 512$ km.

Crater erasure by the mantling process has the effect of reducing the crater population in the model population. However, the slope is not significantly changed. The results

shown in Fig. 10 include examples for both the D-squared and D-cubed deposition laws and for a low and high deposition threshold. With the low threshold a comparatively small deposit thickness is needed to eliminate the crater (Fig. 11). Some of the resulting populations are not bad fits to the Venus data provided one excludes craters below about 64 km (e.g., Fig. 10a, Venus 5; Fig. 10c, Venus 5); however, if the crater densities below 64 km are considered valid, there are substantial deviations. It is evident that models in which crater obliteration threshold is independent of crater diameter will not match the observed data from say 32 km all the way up to the maximum size crater observed.

We have developed a model to provide a better fit to the crater population over this larger range. First, a power law was least squares fit to the crater densities estimated from the Arecibo data. The fitting program fits a curve of the form

$$R = M(D/\bar{D})^B \quad (7)$$

to the input data. Here M and B are parameters determined by the program (with uncertainty estimates) and \bar{D} is the mean diameter of the input data. Note that this is equivalent to

$$\log R = \log M + B(\log D - \log \bar{D}) \quad (8)$$

In Case 1 the population was fit to all craters above 16 km; in Case 2 only craters larger than 32 km were considered; and in Case 3 only craters larger than 45 km were included.

Using the best fit power function for Case 2, which includes only those craters which are at least twice the size of the best resolution Venus data, we have calculated a deposition threshold relationship:

$$T_D/T = (D/400)^{1.67} \quad (9)$$

where T_D = thickness of deposit to remove a crater diameter D , and

T = total deposit thickness from all cratering events.

For a crater production function conforming to the inverse diameter squared law and any crater sedimentation law, the steady state population computed with this threshold law is identical to the best fit curve of Case 2 (Table 1). The derivation of Equation (3) is described in the Appendix. The relationship is compared with the fixed threshold (high and low) independent of diameter in Fig. 11.

Using the Monte Carlo crater population of Fig. 9 we have generated simulated steady state crater populations using the deposition threshold relationship of Equation 3. As expected, the general shape of the simulated populations (Fig. 13) is similar to the observed data from which it was essentially derived in a roundabout statistical way. However, there are considerable differences between two Monte Carlo runs conducted with the same statistical parameters. Deviations from the linear relationship on the log-log

plot far exceed the estimated errors in the individual observations. This is simply a consequence of the large deviations between the actual rate of deposition of crater ejecta material (Fig. 8) and the uniform rate which is assumed in the analytical solution given in the Appendix. These deviations are reflected in attempts to fit the curves in Fig. 13 to a single power function. Variation in the slope and intercept is found in these plots which far exceeds the estimated errors. Only one of the plots gives a result within the range of the analytical model (see Appendix).

The analytical model generates a threshold function for crater obliteration as a function of diameter which can be compared with radiophysical expectations. The 12.6 cm radar signal from bright ejecta haloes originates from surface roughness elements and rocks in the size range of 1 to 10 wavelengths (Thompson et al., 1980b). The size distribution of the rock population and the slope length frequency spectrum of rocks will vary with crater size and the smaller rocks and shorter slopes will be obliterated first by sedimentation. However, it seems unlikely to us that the differences in the ejecta characteristics of small and large craters are sufficient to explain the difference in the deposit thickness needed to obliterate those craters. For example, from Equation 11 it appears that 50 times

more deposition is needed to obliterate the signature for a 500 km diameter crater than for a 50 km diameter crater.

Without a more detailed assessment of all the uncertainties in the estimate of the threshold function (Fig. 11), we cannot say definitely whether a global deposition model is consistent with the observational data. There are several reasons why the slope of this relationship may have been overestimated. The deposition relationships of equation (5a) maybe simplistic and uniform deposition over the planet's surface is unlikely. The $1/D^2$ distribution for crater production may be inappropriate at large diameters and statistical effects can yield significant deviations from the simple analytical model as seen in Fig. 13. Finally, our estimate of the population of craters with radar bright ejecta deposits will be low at the smaller diameters because of resolution loss.

DISCUSSION

A basic question in these calculations is whether a cratering event can inject enough material into suspension to obliterate craters. Alvarez et al. (1980) have discussed the possibility that a 10 km diameter asteroidal body impacted the earth 65 million years ago forming a 100 km diameter crater and laid a 1 cm thick layer of dust across the entire earth causing the Cretaceous-Tertiary extinction. If a 100 km diameter crater could produce a layer this thick on the earth, then it seems quite possible that some of the larger events considered in our model (up to 300 km crater diameter) would have produced layers with thicknesses up to a meter on Venus.

Scattering of 3.8 cm radiation in lunar ejecta deposits appears to be dominated by centimeter-sized blocks; analogously, scattering of 12.6 cm radiation from Venus is likely to be dominated by blocks of at most a few tens of centimeters in size. Scattering from such a block population would be substantially reduced by a layer a few tens of centimeters thick. However, it is not obvious why the deposition threshold for removal of the scattering signature would have the strong diameter dependence inferred from the steep slope of the crater densities. One possibility is that smaller craters (below $D = 64$ km) do not produce strong signatures and are not

resolved in the radar images as discussed above. Another possibility is that more of the larger features are volcanic in origin and bias the shape of the crater curve. Many of the observed Venus ring structures are not randomly distributed and occur in clusters. Consequently, we should also entertain modifications to the mechanism illustrated in Fig. 7.

Conceivably, atmospheric turbulence induced by cratering events disturb surface material over areas much greater than the size of the crater or the depositional ejecta deposit immediately around it. The energy introduced into the lower atmosphere by impact events would produce much greater wind intensities than the weak solar and rotational effects that act on the Venusian lower atmosphere. Although not global in extent such processes could erase craters on areas of regional scale and the net result would be similar to that depicted by our model of global obliteration by suspended material (Fig. 7).

Radar data on the average properties of the Venusian surface tend to support sedimentation mantling of large areas of the Venusian surface. The average small scale roughness on Venus is only a third of what it is on the Moon (Jurgens, 1970); this suggested to Jurgens and Dyce (1970) that the surface was neither blocky nor contained high slopes. The reflectivity and, hence the density, of the surface materials appears to be rather high compared with lunar surface materials (Rogers and Ingalls, 1970). It seems unlikely that a sediment deposited from suspension would be densely packed; however, reworking by surface currents

could have caused densification as happens in terrestrial eolian dunes and stream beds.

In terms of the model presented here, radar bright upland features on Venus would be interpreted as recent geological features or areas on which sediment was not retained. The insitu visual observations of the Venusian surface that were acquired by Venera 9 and 10 were acquired on the eastern margins of the radar bright Rheu Mons and Thea Mons in the Beta region (Pettengill et al., 1980). They established the existence of a blocky surface consistent with the radar signatures. Conceivably, as still better images of Venus are acquired, we will begin to discern in detail the effects of fluid transport processes on the Venus surface.

CONCLUDING REMARKS

The surface of Venus as seen in Arecibo radar images has a small population of bright ring features. We have compared the properties of radar bright ring features on Venus with the radar bright haloes around young lunar craters. We have concluded that the bright ring-shaped features on Venus are crater ejecta deposits which are rapidly destroyed in the Venus surface environment just as they rapidly disappear on the surface of the moon. However, the mechanisms of removal must be radically different on the two bodies. We have evaluated a process for removing Venusian radar crater signatures in which material injected by large cratering events into atmospheric suspension mantles the rocky radar bright ejecta deposits of earlier formed craters. Such a process does not readily explain the pronounced excess of large craters in the Venus population. Conceivably, small craters are underrepresented in the observed Venus population for observation reasons or because of a difference in the type of ejecta deposit developed at small crater sizes. Alternatively intense regional winds set in motion by large cratering events could have reworked surface materials on areas of regional extent and selectively removed the signatures of small craters. Whatever mechanism is valid, the effects of large cratering events on deposition and erosion need to be taken into account in interpreting radar images acquired with large radar incidence angles such as those obtained at Arecibo and those that will be acquired from the projected VOIR spacecraft.

APPENDIX -- DERIVATION OF THRESHOLD DEPOSITION THICKNESS RELATION

Suppose N_0 craters to have formed in an area A according to a $1/D^2$ cumulative distribution relationship:

$$\text{Pr \{diameter} \geq D\} = (D_{\min}/D)^2 (D \geq D_{\min}) \quad A(1)$$

If all these craters are visible and are grouped into diameter bins whose boundaries are successive powers of some number ρ , e.g., 2, then the expected number ($N(D)$) of craters in a bin of mean diameter D can be expressed as:

$$N(D) = N_0 \left[(\rho^{1/2} D_{\min}/D)^2 - (\rho^{-1/2} D_{\min}/D)^2 \right] \quad A(2)$$

which simplifies to:

$$N(D) = N_0 ((\rho^2 - 1)/\rho) (D_{\min}/D)^2 \quad A(3)$$

The expected value of the Relative Crater Density (R) can be expressed in terms of the observed density in the bin as

$$R = (\rho^{1/2} N(D) D^2) / ((\rho - 1)A) \quad A(4)$$

and substituting for $N(D)$ from Equation 3 the value of R for the cumulative crater density relationship of Equation (1) is

$$R_0 = N_0 = (\rho + 1) \rho^{-1/2} D_{\min}^2 / A \quad A(5)$$

where A is the area of the terrain surface.

We wish to find a function $t(D)$, where $t(D)$ is the minimum thickness of material which must be deposited to obscure a crater of diameter D , such that the observed relationship between R and D is

$$\log R = \alpha \log D + \beta \quad A(6)$$

α and β are defined by a least squares fit to the observed crater population.

At some large diameter (D_{\max}) no craters are obliterated and $R(D_{\max})$ expressed from Equation A(6) is equal to R_0 from Equation (5). Consequently we can express R as

$$R = R_0 (D/D_{\max})^\alpha \quad (7)$$

This expression can be equated to the relationship for the relative density (Equation 4) in order to determine the number of craters ($N'(D)$) in a bin of average diameter D in the observed population.

$$R_0 (D/D_{\max})^\alpha = (\rho^{1/2} N'(D) D^2) / ((\rho - 1)A) \quad (8)$$

which yields

$$N'(D) = (\rho - 1)^{-1/2} A \cdot R_0 \cdot D^{\alpha-1} / D_{\max}^\alpha \quad (9)$$

If the rate of deposition on the surface has been uniform then

$$N'(D) = N(D) \cdot t(D) / T \quad (10)$$

where T is the total thickness of material deposited during the cratering history of the area. Combining expressions (9) and (10) we get

$$t(D) = T (D/D_{\max})^\alpha$$

ACKNOWLEDGEMENTS

We would like to thank Dr. Stan Zisk for permission to use the 3.8 cm radar data and Dr. Donald Campbell for providing original prints of some of Arecibo Venus images reproduced here. This work was supported by the National Aeronautics and Space Administration, Planetary Division under contract NASW 3383.

REFERENCES

- Alvarez, L.W., W. Alvarez, F. Asaro, and H.V. Michel (1980). Extraterrestrial cause for the Cretaceous-Tertiary extinction. Science 208, 1095-1108.
- Campbell, D.B., R.B. Dyce and G.H. Pettengill (1976). New radar image of Venus. Science 193, 1123-1124.
- Campbell, D.B., B.A. Burns, and V. Buriakoff (1979). Further evidence of impact cratering and tectonic activity from radar observations. Science 204, 1425-1427.
- Campbell, D.B., and B.A. Burns (1980). Earth-based radar Imagery of Venus. J. Geophys. Res. (in press).
- Carr, M.H., L.S. Crumpler, J.A. Cutts, R. Greeley, J.E. Guest, and H. Masursky (1977). Martian impact craters and emplacement of ejecta by surface flow. J. Geophys. Res. 82, 4055-4066.
- Goldstein, R.M., R.R. Green, and H.C. Rumsey (1976). Venus radar images. J. Geophys. Res. 81, 4807-4817.
- Goldstein, R.M., R.R. Green, and H.C. Rumsey (1978). Venus radar brightness and altitude images. Icarus 36, 334-352.
- Hartmann, W.K. (1977). Relative crater production rates in planets. Icarus 31, 260-276
- Jurgens, R.F., and R.B. Dyce (1970). Radar backscattering properties of Venus at 70 cm wavelength. Astron. J. 75, 297-314
- Jurgens, R.F. (1970). Some preliminary results of the 70 cm radar studies of Venus. Radio Science 5, 435-442.

- Malin, M.C., and R.S. Saunders (1977). Surface of Venus: Evidence of diverse landforms from radar observations. Science 196, 987-990.
- Pettengill, G.H. (1978). Physical properties of the planets and satellites from radar observations. Ann. Rev. Astron. Astrophys. 16, 265-292.
- Pettengill, G.H., D.B. Campbell, and H. Masursky (1980). The surface of Venus. Scientific American 243, 54-65.
- Pettengill, G.H., P.G. Ford, W.E. Brown, C.H. Keller, H. Masursky, and G.E. McGill (1979). Pioneer Venus radar mapper experiment. Science 203, 806-808.
- Pike, R.J. (1977). Size-dependence in the shape of fresh impact craters on the Moon. In Impact and Explosion Cratering (D.J. Roddy, R.O. Pepin, and R.B. Merrill, Eds.) pp. 489-509. Pergamon Press, New York.
- Rogers, A.E.F. and R.P. Ingalls. (1970) Radar mapping of Venus with interferometric resolution of the range-Doppler ambiguity. Radio Science 5, 425-433.
- Rumsey, H.C., G.A. Morris, R.B. Green and R.M. Goldstein (1974) A radar brightness and altitude profile of a portion of Venus. Icarus 23, 1-7.
- Saunders, R.S. and M.C. Malin (1976) Venus Geological Analysis of radar images. Geol. Romana 15, 507-515.
- Schaber, G.G. and J.M. Boyce (1977) Probable distribution of large impact basins on Venus: Comparison with Mercury and the Moon. Impact and Explosion Cratering, Pergamon Press (New York), 603-612

Schultz, P.H., and D.E. Gault (1979). Atmospheric effects on martian ejecta emplacement. J. Geophys. Res. 84, 7669-7687.

Settle, M. (1980). The role of fallback ejecta in the modification of impact craters. Icarus 42, 1-19.

Tauber, M.E., and D.B. Kirk (1976). Impact craters on Venus. Icarus 28, 351-357.

Tauber, M.E., D.B. Kirk, and D.E. Gault (1978). An analytical study of impact ejecta trajectories in the atmospheres of Venus, Mars and Earth. Icarus 33, 529-536.

Thompson, T.W., J.A. Cutts, R.W. Shorthill, and S.H. Zisk (1980a). Infrared and radar signatures of lunar craters: implications about crater evolution. Proc. Conf. Lunar Highlands Crust, 483-499.

Thompson, T.W., S.H. Zisk, R.W. Shorthill, P.H. Schultz, and J.A. Cutts (1980b). Lunar craters with radar bright ejecta. Submitted to Icarus.

Woronow, A. (1978). A general cratering-history model and its implications for the lunar highlands. Icarus 34, 76-88.

LIST OF TABLES

- Table 1: Analysis of measured Venus radar crater populations from Pettengil et al. (1980), and Campbell and Burns (1980).
- Table 2: Results of Monte Carlo simulations.

CASE	DATA SELECTED	SLOPE	LOG R AT 64 KM	χ^2	DEGREES OF FREEDOM
A	CRATERS ABOVE 16 KM DIAMETER (5 DATA POINTS)	-3.3 ± .20	-3.66	4.83	3
B	CRATERS ABOVE 32 KM DIAMETER (4 DATA POINTS)	-.73 ± .29	-3.52	2.45	2
C	CRATERS ABOVE 48 KM DIAMETER (3 DATA POINTS)	-2 (FIXED)	-3.47	6.54	2

TABLE 1: ANALYSIS OF MEASURED VENUS RADAR CRATER POPULATIONS FROM
PETTENGILL ET AL. 1980 AND CAMPBELL AND BURNS (1980).

MODEL I: DEPOSITION \propto DIAMETER CUBED

SIMULATION	SLOPE	$\frac{\log R}{64 \text{ KM}}$	χ^2	DEGREES OF FREEDOM
1 (5)	$1.37 \pm .07$	-3.67	50.70	7
2 (6)	$1.21 \pm .04$	-3.28	135.63	9
3 (7)	$1.17 \pm .04$	-3.29	139.89	8

MODEL II: DEPOSITION \propto DIAMETER SQUARED

1	$1.83 \pm .10$	-4.09	15.12	5
2	$1.39 \pm .07$	-3.67	45.88	9
3	$1.33 \pm .08$	-3.67	11.03	8

TABLE 2: RESULTS OF MONTE CARLO SIMULATIONS

FIGURE CAPTIONS

- Figure 1 (a) Lunar craters with 3.8 cm radar bright ejecta deposits: Mare Serenitatis, Mare Tranquillitatis, and adjoining terra.
(b) Low sun photograph of the same area. Craters with large radar bright halos are identified with circles with the diameter of the halo.
- Figure 2 (a) 70 cm depolarized radar map of lunar crater Plato (100.0 km diam.) and its environs. Plato's floor has been flooded by mare.
(b) Arecibo 12.5 cm radar image of three circular Venusian features located near longitude 340° and latitude -27° . The largest and smallest circular features are about 100 km and 60 km in diameter respectively.
- Figure 3 (a) Distribution of craters with 3.8 cm radar bright ejecta on the moon.
(b) Distribution of features with radar bright annular features and dark circular features on Venus.
- Figure 4 Scatter diagrams of radar halo diameters versus crater diameters for Lunar and Venusian craters. Lunar craters (a and b) were observed at 3.8 cm and 70 cm wavelengths. Only craters with 3.8 cm haloes plotting near or above the solid line (diameter greater than 20 km or twice crater diameter) were included in the compilation for reasons discussed by Thompson et al., 1980a. This emphasized young craters with diameters

(Figure 4 - cont'd.)

between one and ten kilometers, where 70 cm haloes are smaller than the 3.8 cm haloes (see Thompson et al., 1980b. Venus craters (c and d) were taken from Campbell and Burns (1980). Venus crater diameters in (d) are published values, while (c) shows modified crater diameters assuming the dark central areas in the Venus radar images corresponds to a floor width similar to those observed in lunar craters. (Pike, 1977).

- Figure 5 Least square fit to crater distributions for Oceanus Procellarum (67 craters, $1.4 \times 10^6 \text{ km}^2$) and 3.8 cm radar bright halo craters with diameters greater than 4.0 kilometers (59 craters, $12.0 \times 10^6 \text{ km}^2$). Results of least squares fit given in Table 1.
- Figure 6 Actual population of bright annular features on Venus compared with the predicted crater density for a 3.2 billion year old surface.
- Figure 7 Model of radar crater obliteration on Venus.
- Figure 8 Deposition on Venus for the D^2 and D^3 deposition laws.
- Figure 9 Comparison of measured venus radar crater population with Monte Carlo simulations.

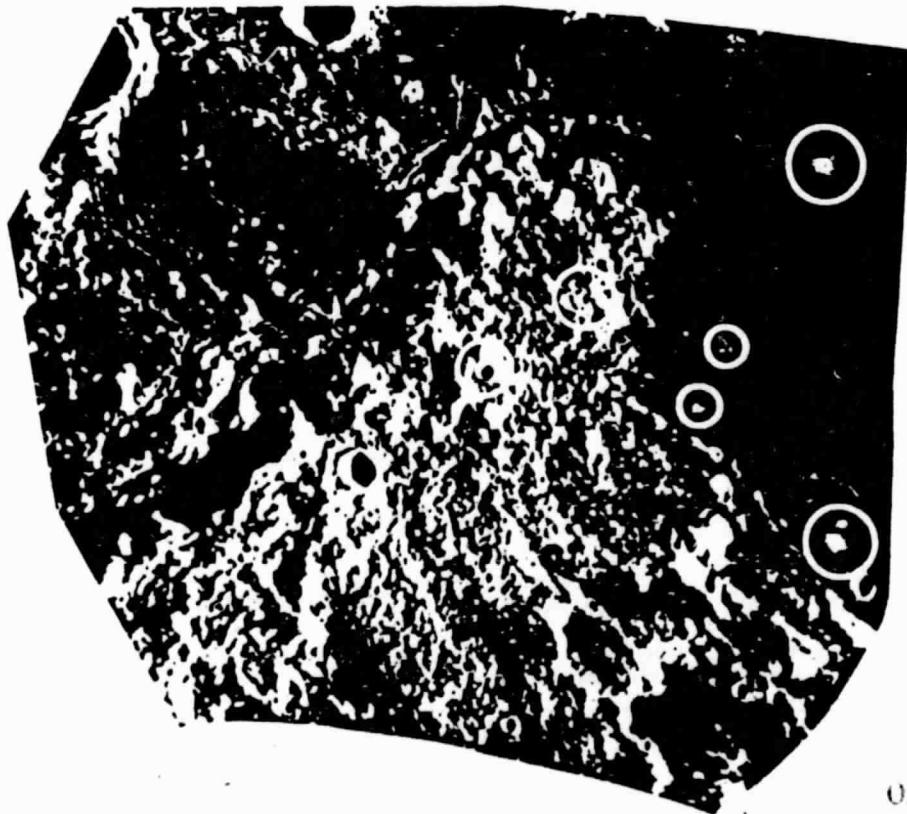
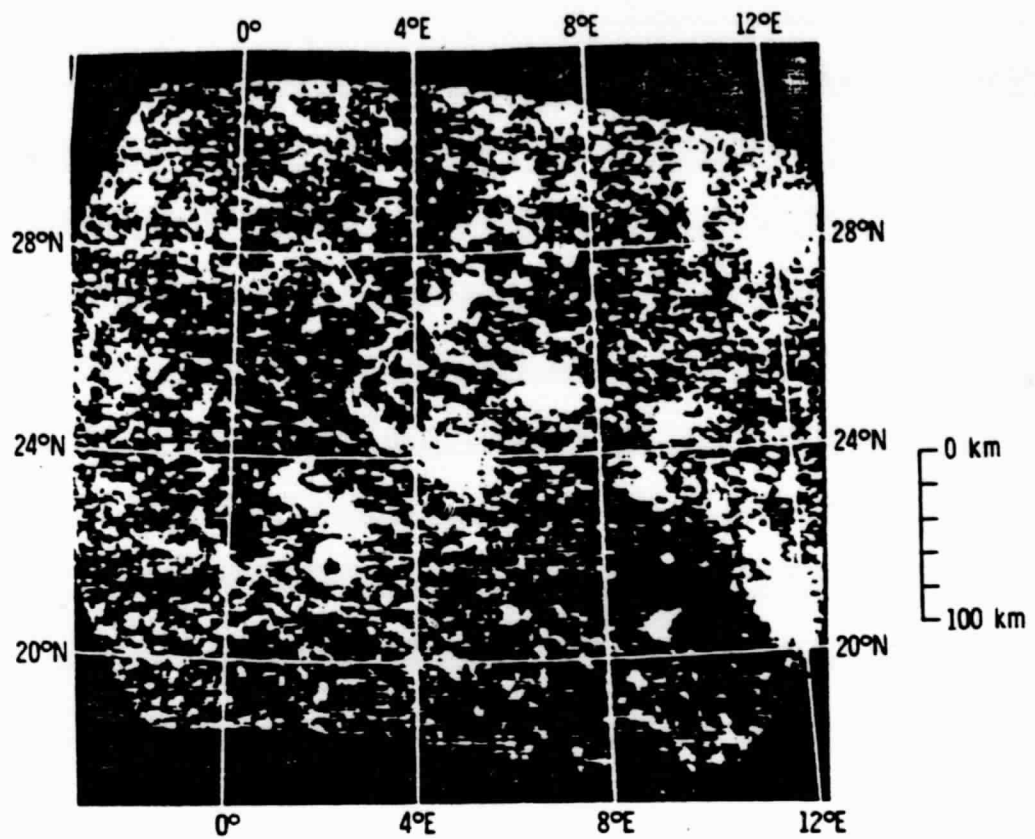
Figure 10 (a) Comparison of measured Venus radar crater population with Monte Carlo simulations.
 (b) Comparison of measured Venus radar crater population with Monte Carlo simulations.
 (c) Comparison of measured Venus radar crater population with Monte Carlo simulations.

Figure 10 (d) Comparison of measured Venus radar crater population with Monte Carlo simulations.

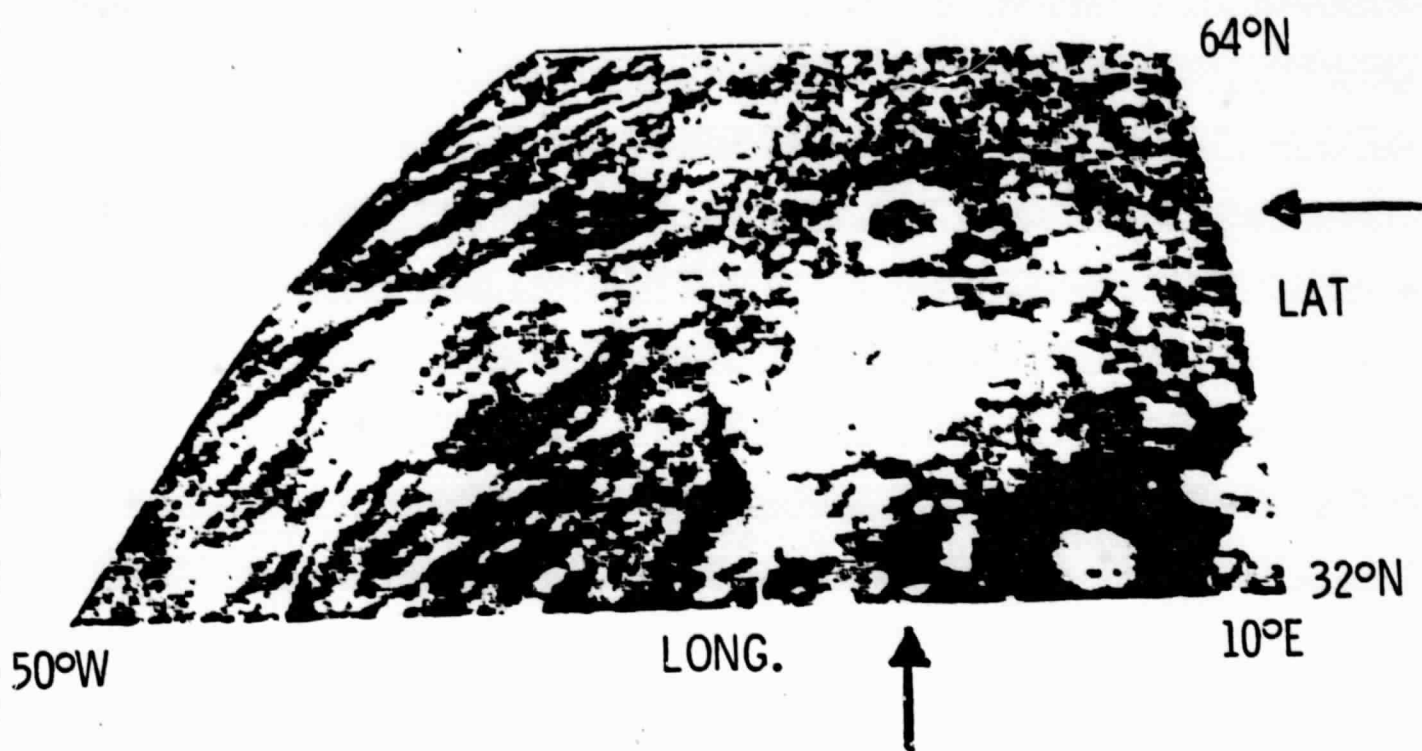
Figure 11 The threshold thickness for crater radar signal obliteration as a function of crater diameter.

Figure 12 (a) Case A: Least squares fit: five data points.
 (b) Case B: Least squares fit: four data points;

Figure 13 Comparison of measured Venus radar crater population with Monte Carlo simulations generated with the crater obliteration threshold law of equation (9):
 (a) D^2 sedimentation law.
 (b) D^3 sedimentation law.



ORIGINAL PAGE IS
OF POOR QUALITY



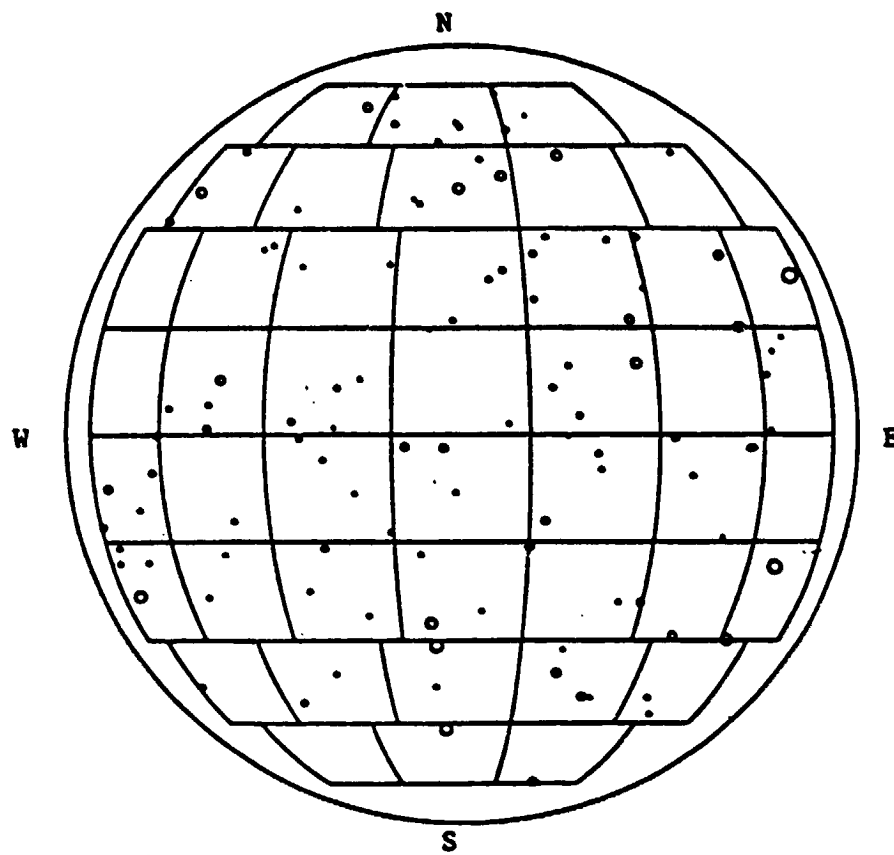


Figure 3(a)

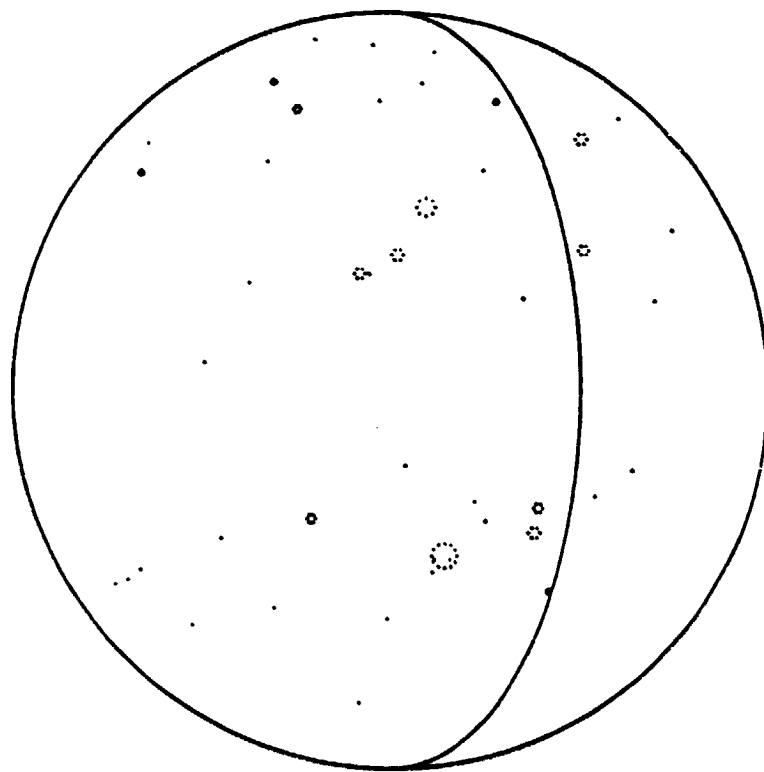


Figure 3(b)

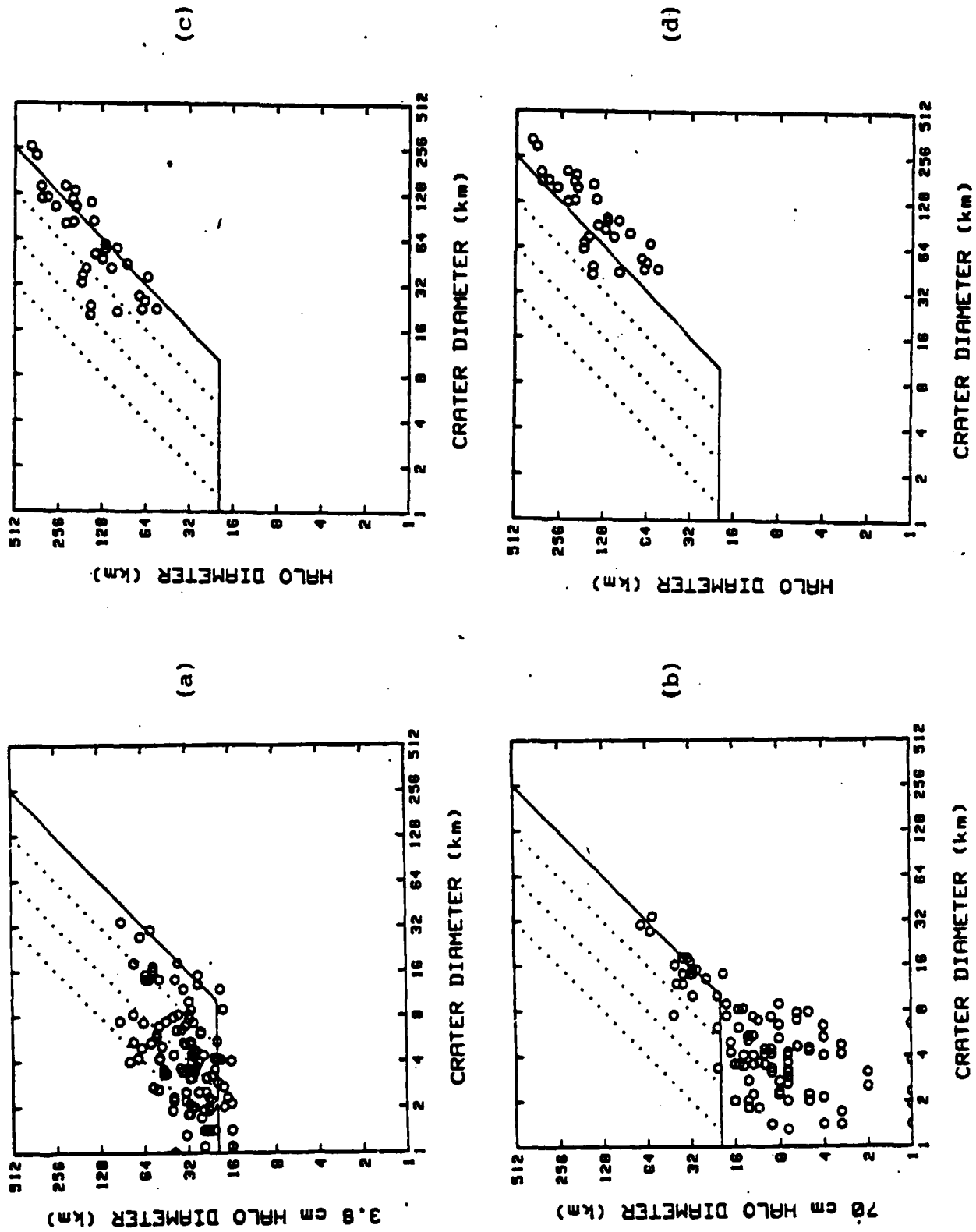


FIGURE 4:

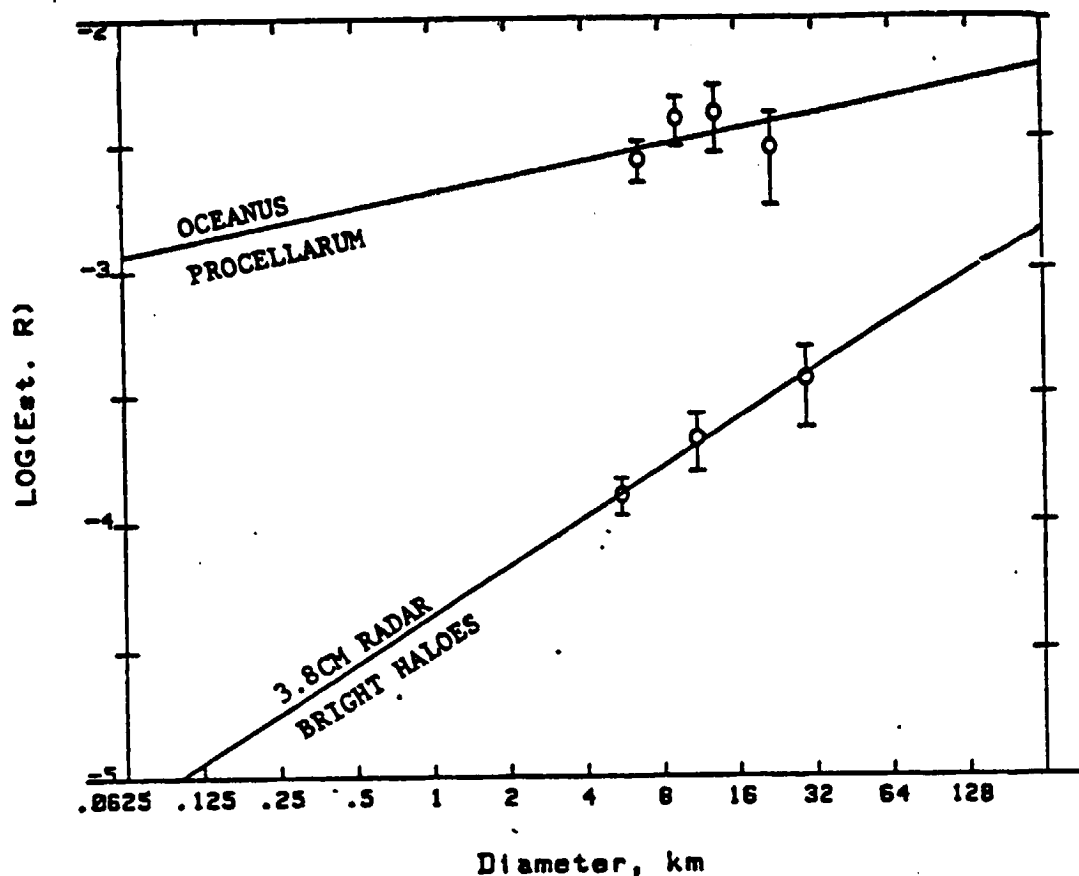


Figure 5: Least square fit to crater distributions for Oceanus Procellarum (67 craters, $1.4 \times 10^6 \text{ km}^2$) and 3.8cm radar bright halo craters with diameters greater than 4.0 kilometers (59 craters, $12.0 \times 10^6 \text{ km}^2$). Results of least squares fit given in Table 1.

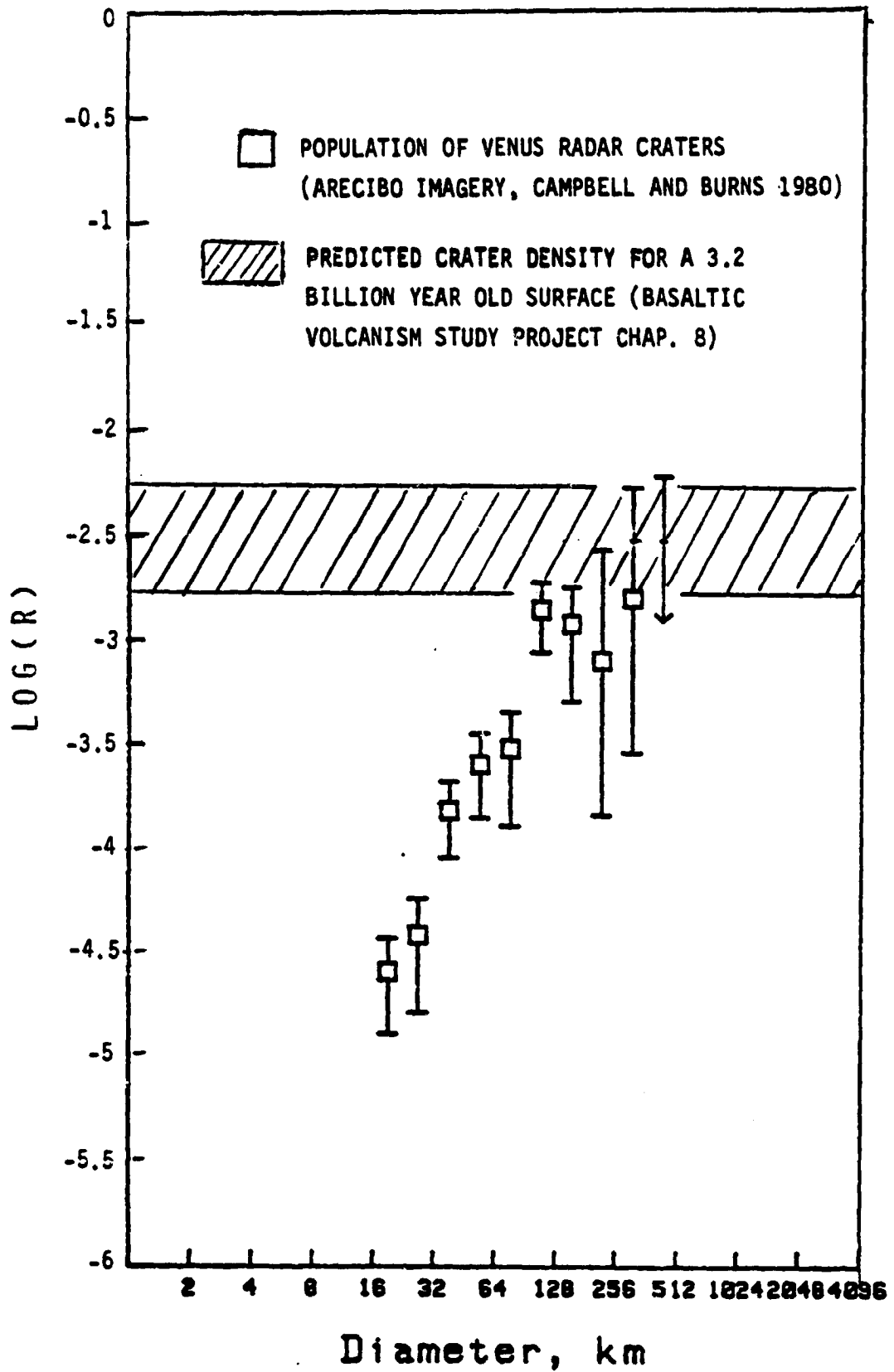
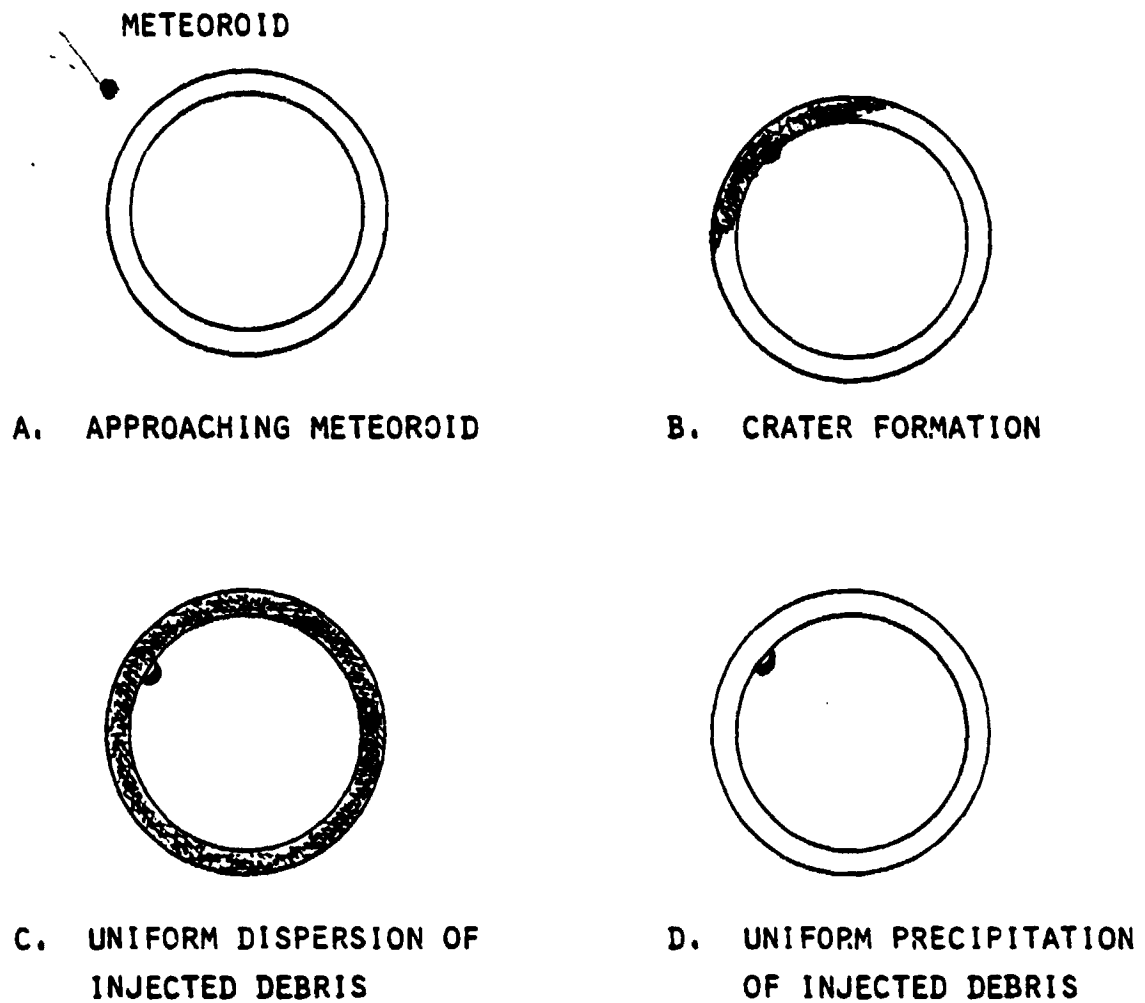
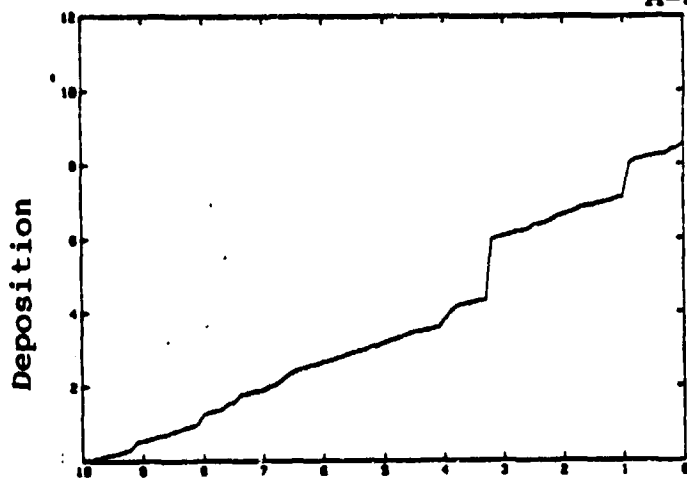


FIGURE 6:

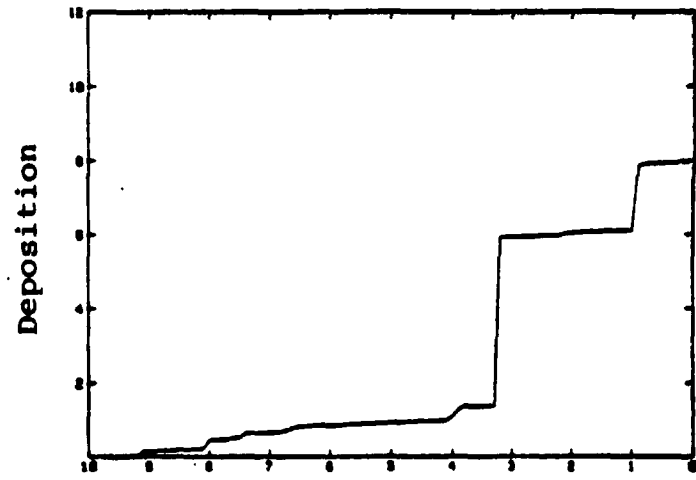


MODE OF RADAR CRATER OBLITERATION ON VENUS

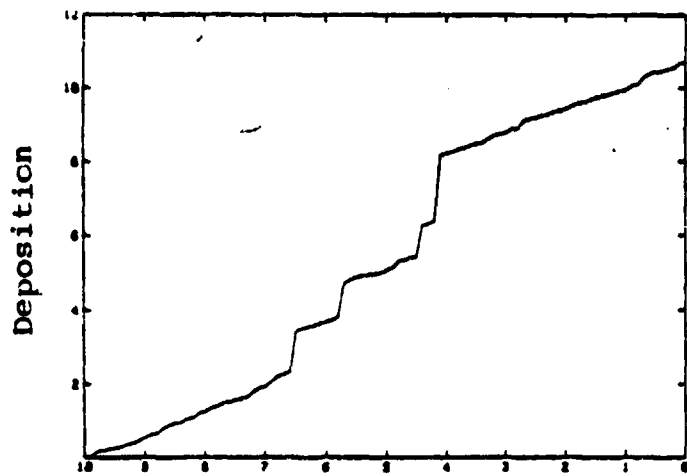
FIGURE 7:



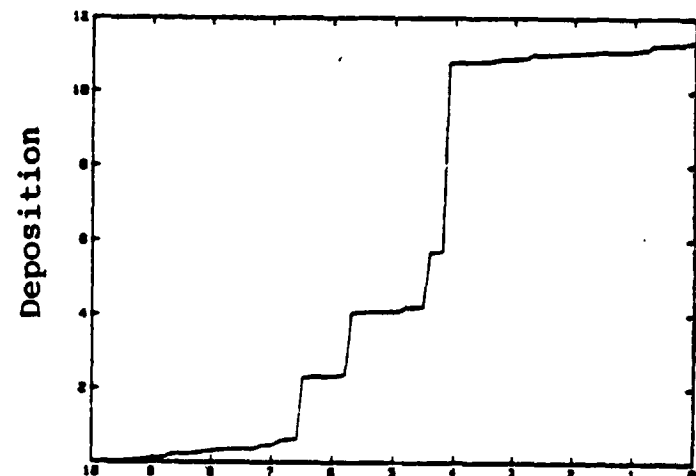
Time Versus 5



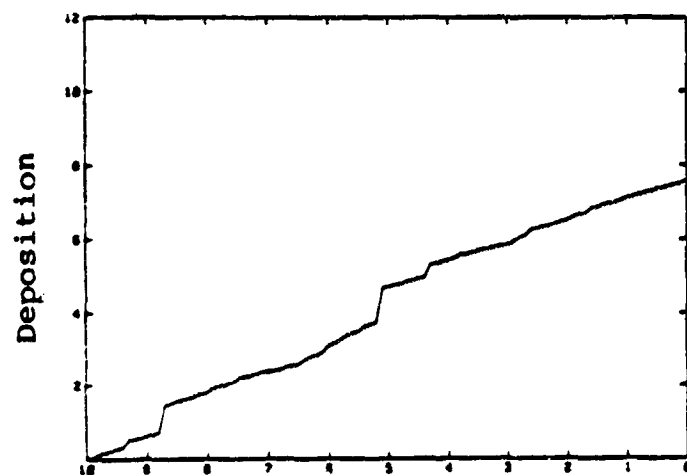
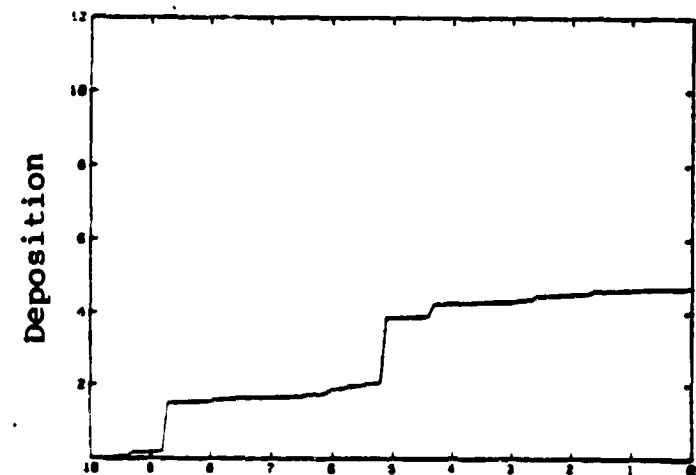
Time Versus 5



Time Versus 6



Time Versus 6

Time Versus 7
Deposition $\propto D^2$ Time Versus 7
Deposition $\propto D^3$

DEPOSITION ON VENUS FOR THE D^2 AND D^3 DEPOSITION LAWS

FIGURE 8:

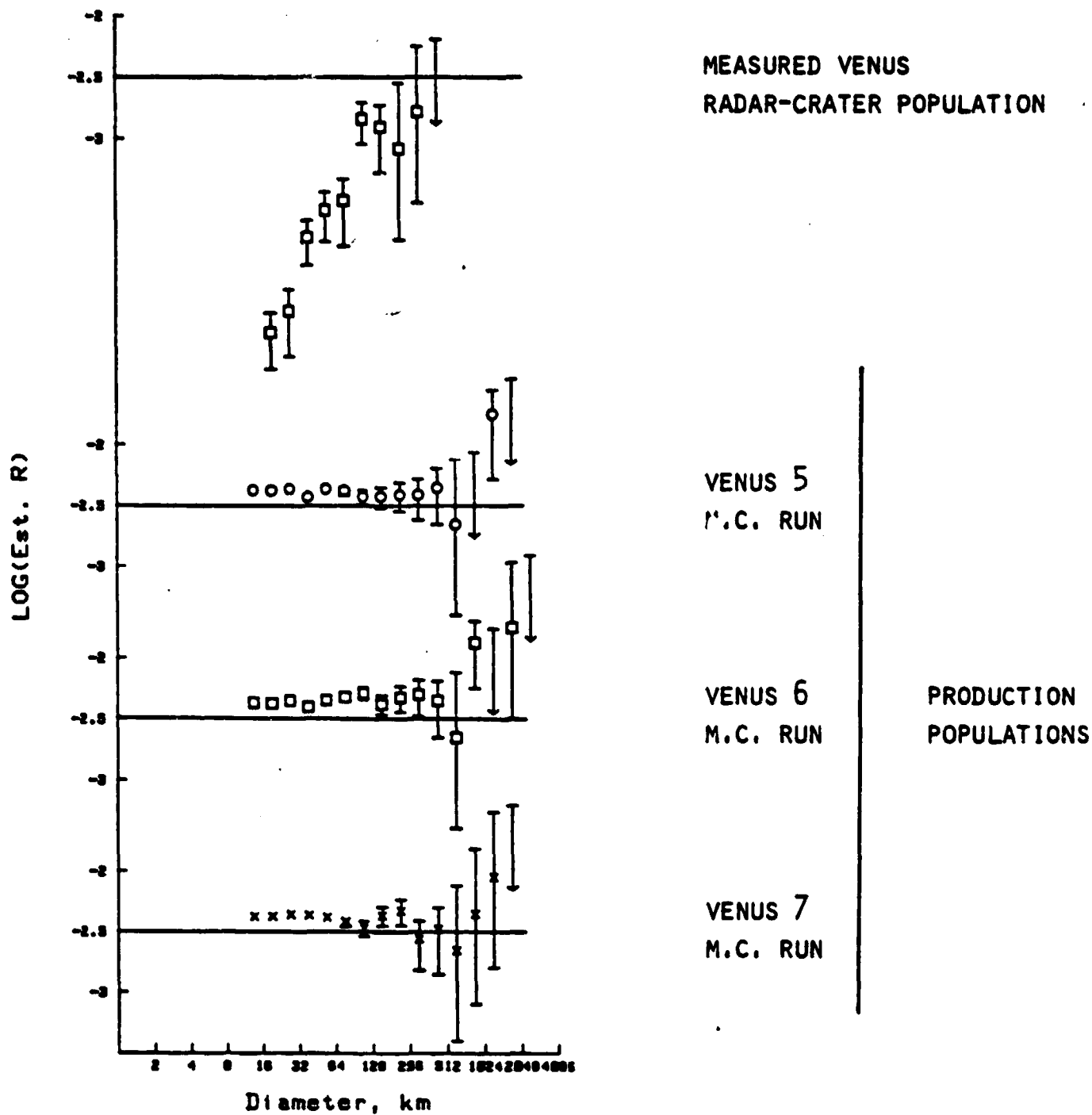


FIGURE 9:
COMPARISON OF MEASURED VENUS RADAR CRATER POPULATIONS WITH
MONTE CARLO SIMULATIONS.

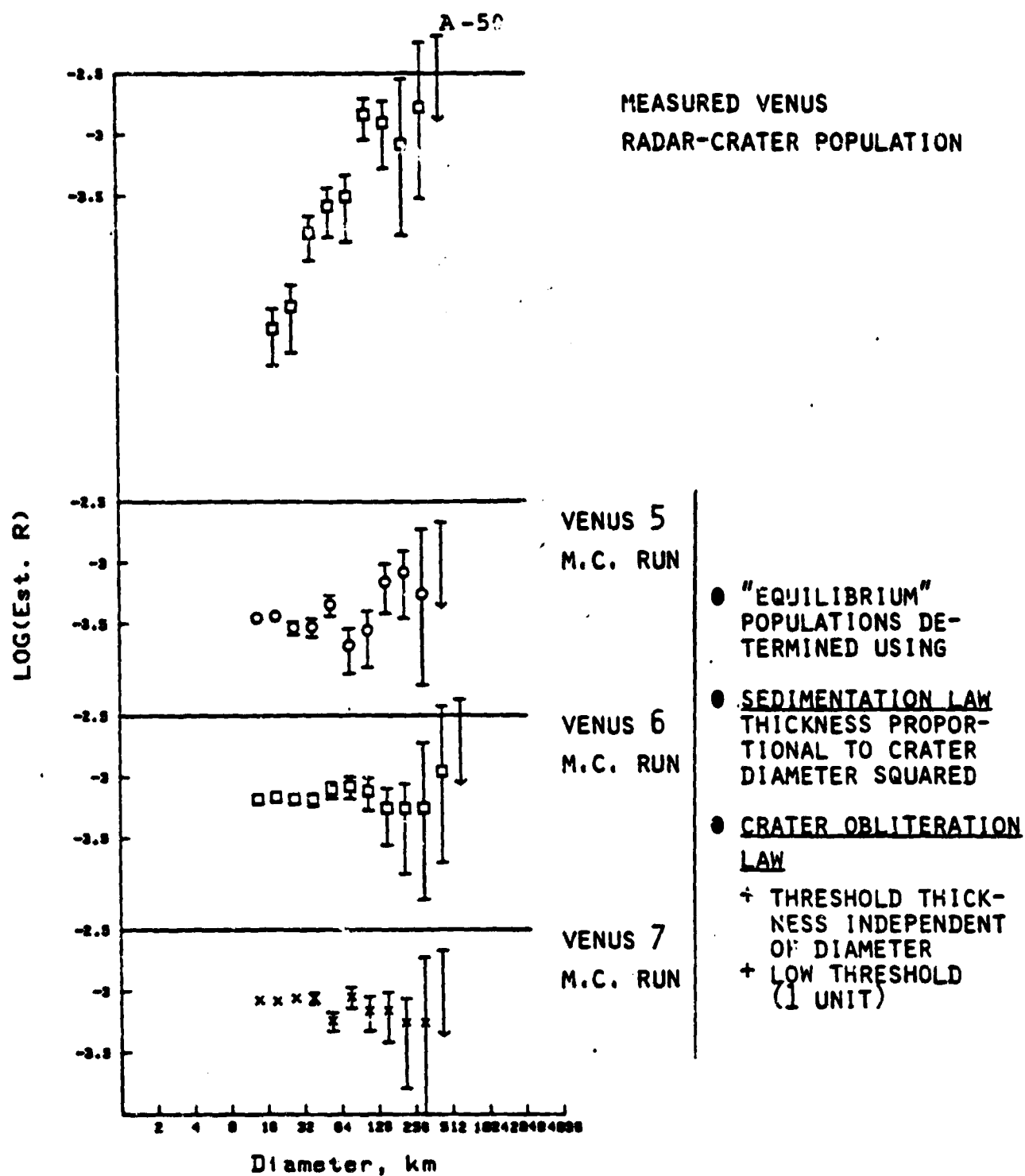


FIGURE 10(a):
COMPARISON OF MEASURED VENUS RADAR CRATER POPULATION WITH
MONTE CARLO SIMULATIONS.

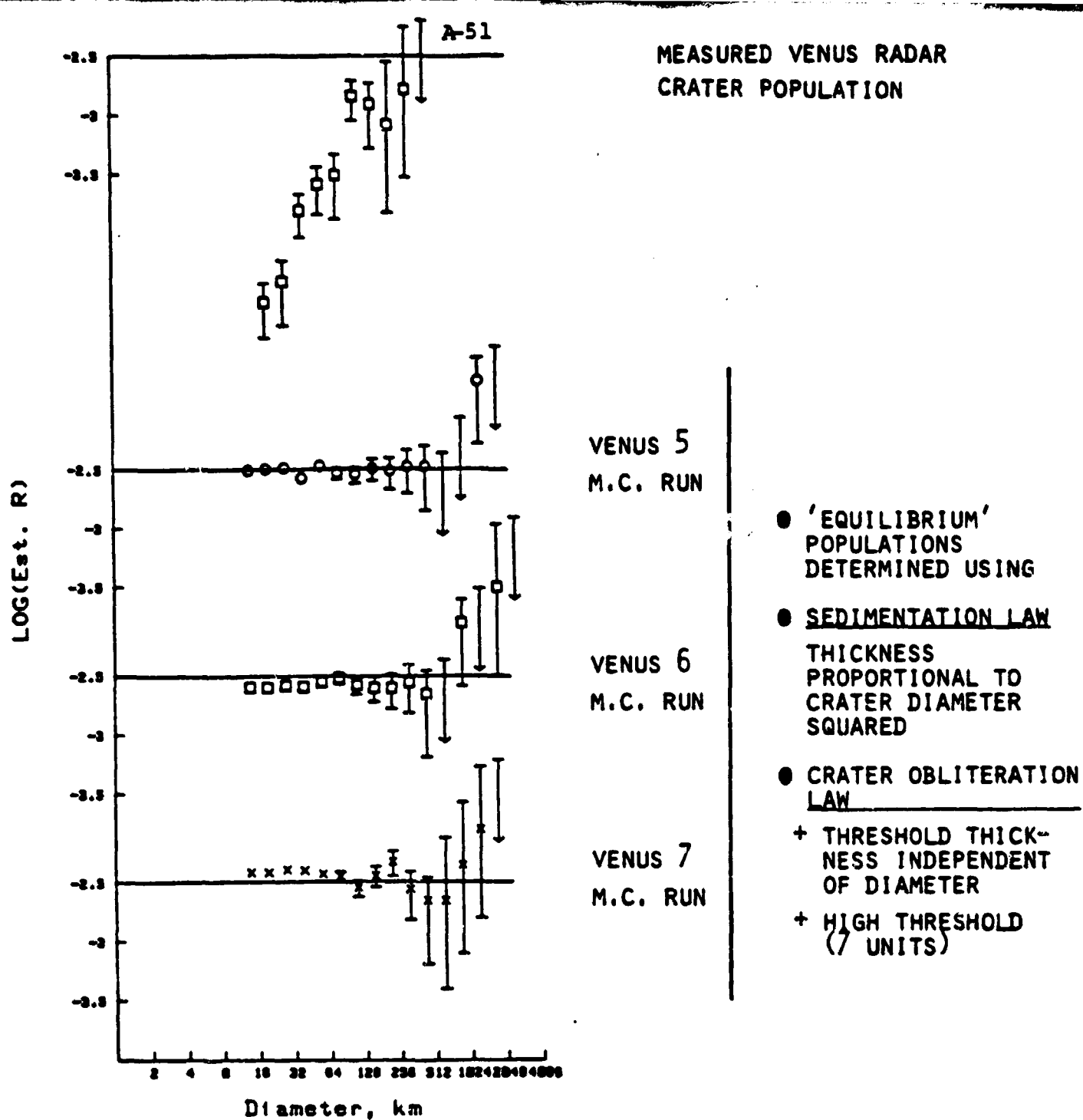


FIGURE 10(b):
COMPARISON OF MEASURED VENUS RADAR CRATER POPULATION WITH
MONTE CARLO SIMULATIONS

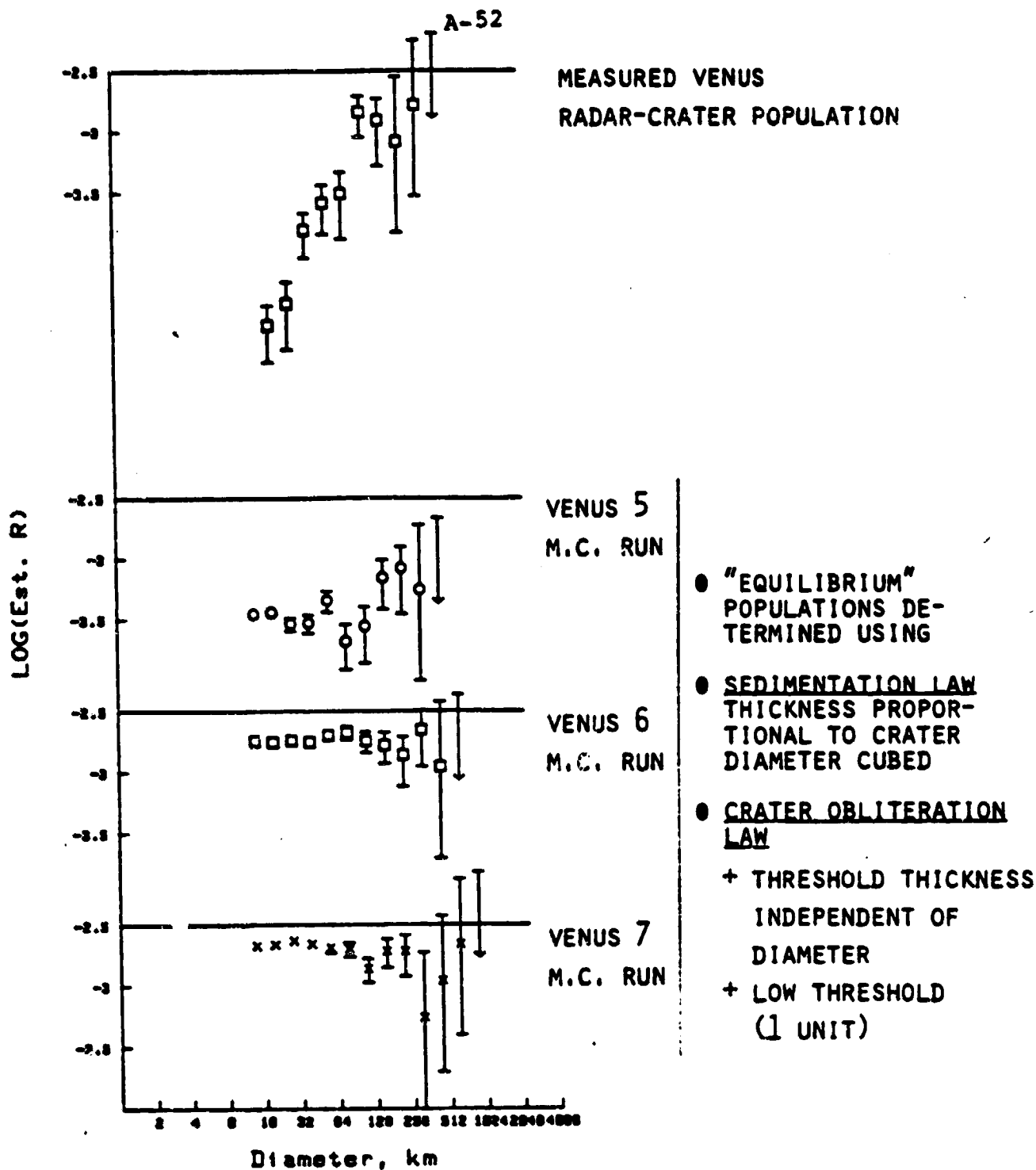


FIGURE 10(c):
COMPARISON OF MEASURED VENUS RADAR CRATER POPULATION WITH
MONTE CARLO SIMULATIONS.

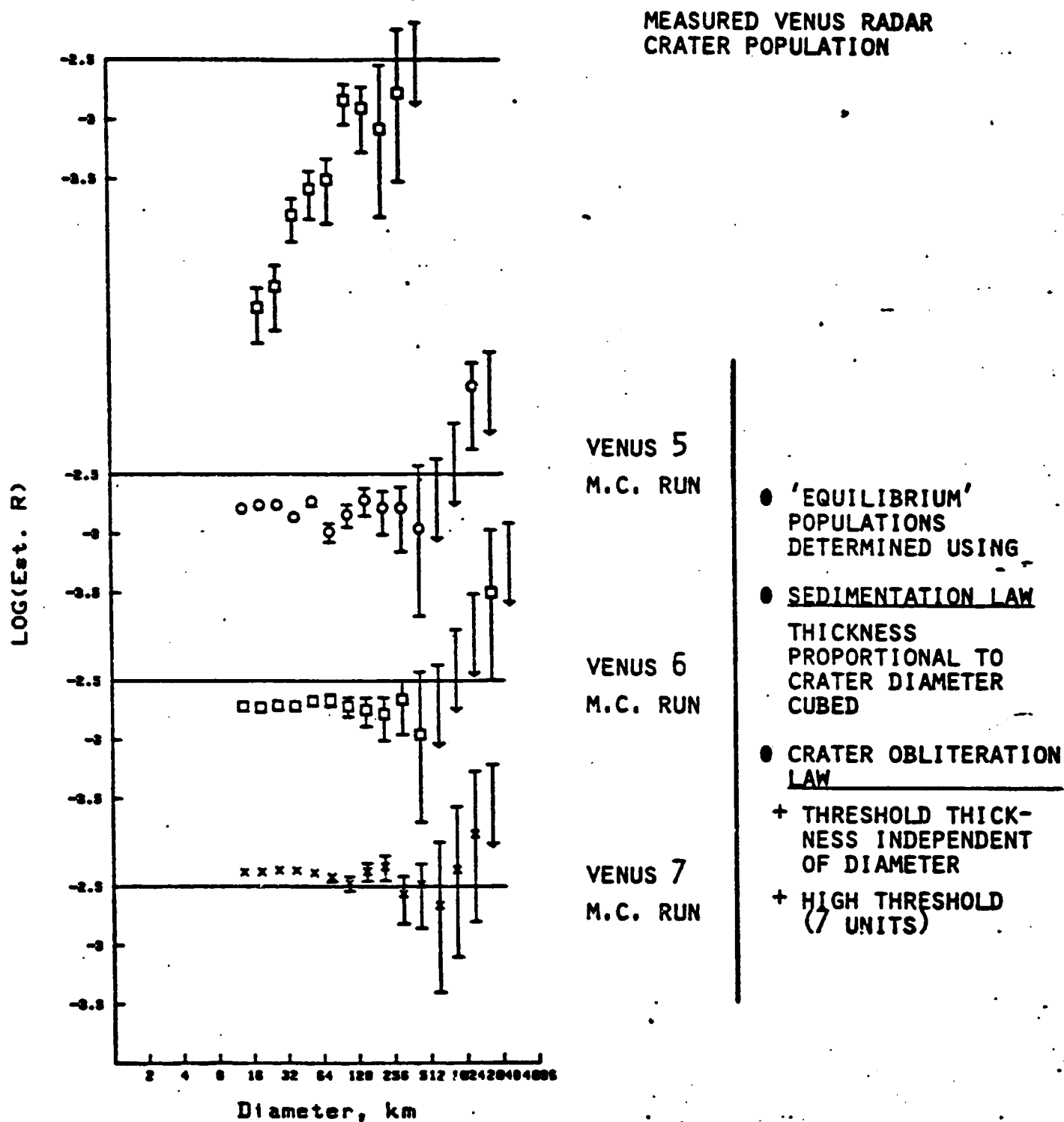


FIGURE 10(d):
COMPARISON OF MEASURED VENUS RADAR CRATER POPULATION WITH
MONTE CARLO SIMULATIONS

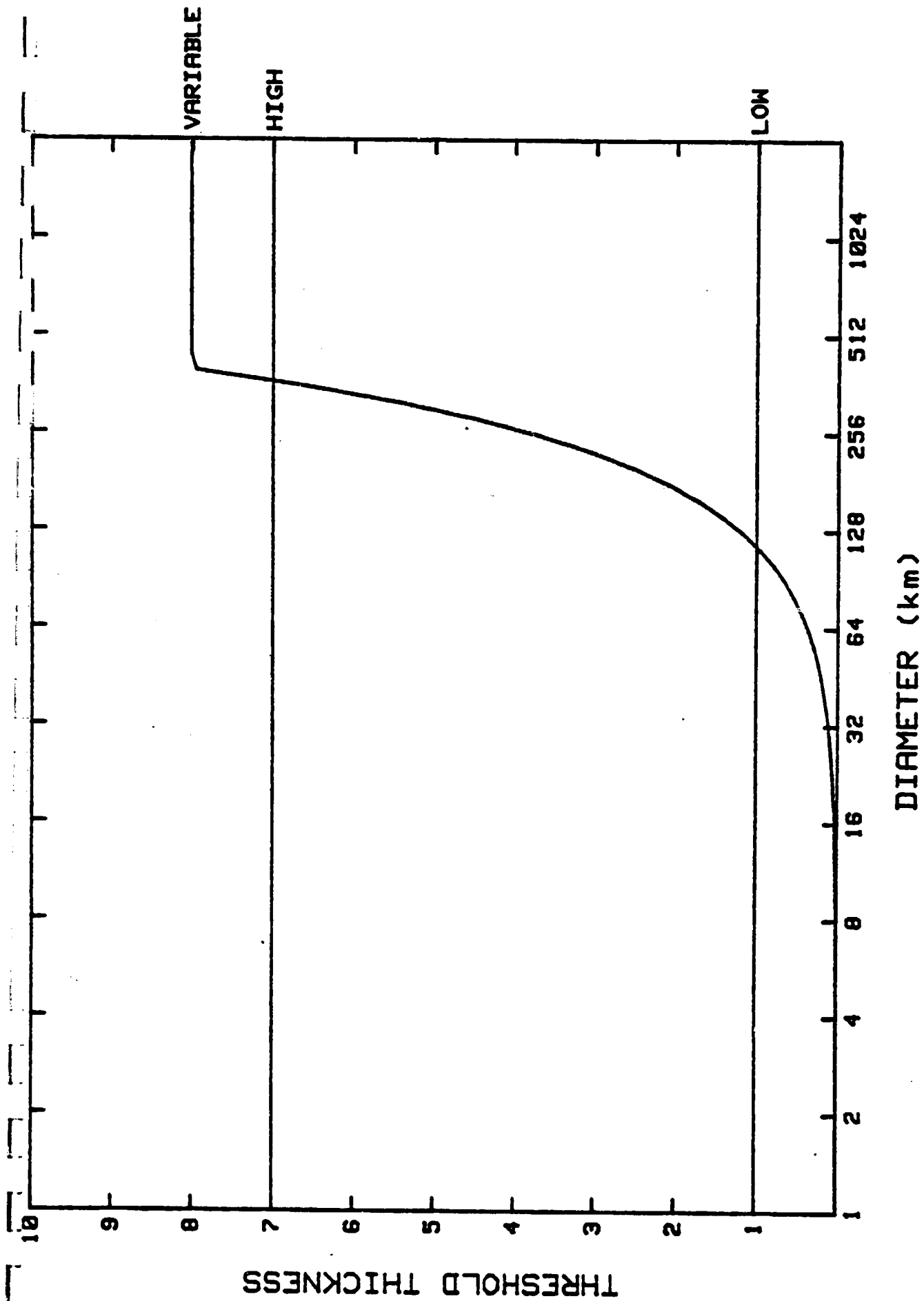


FIGURE 11: THE THRESHOLD THICKNESS FOR CRATER RADAR SIGNAL OBLITERATION AS A FUNCTION OF CRATER DIAMETER

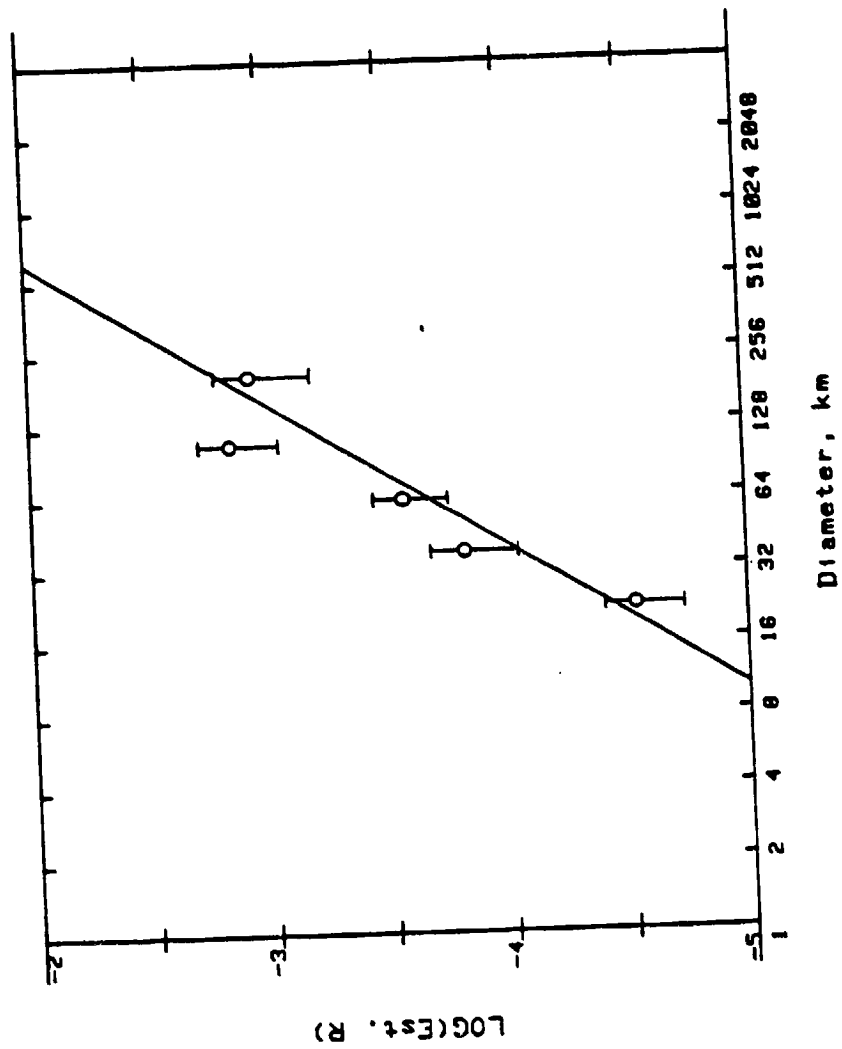


Figure 12(a):

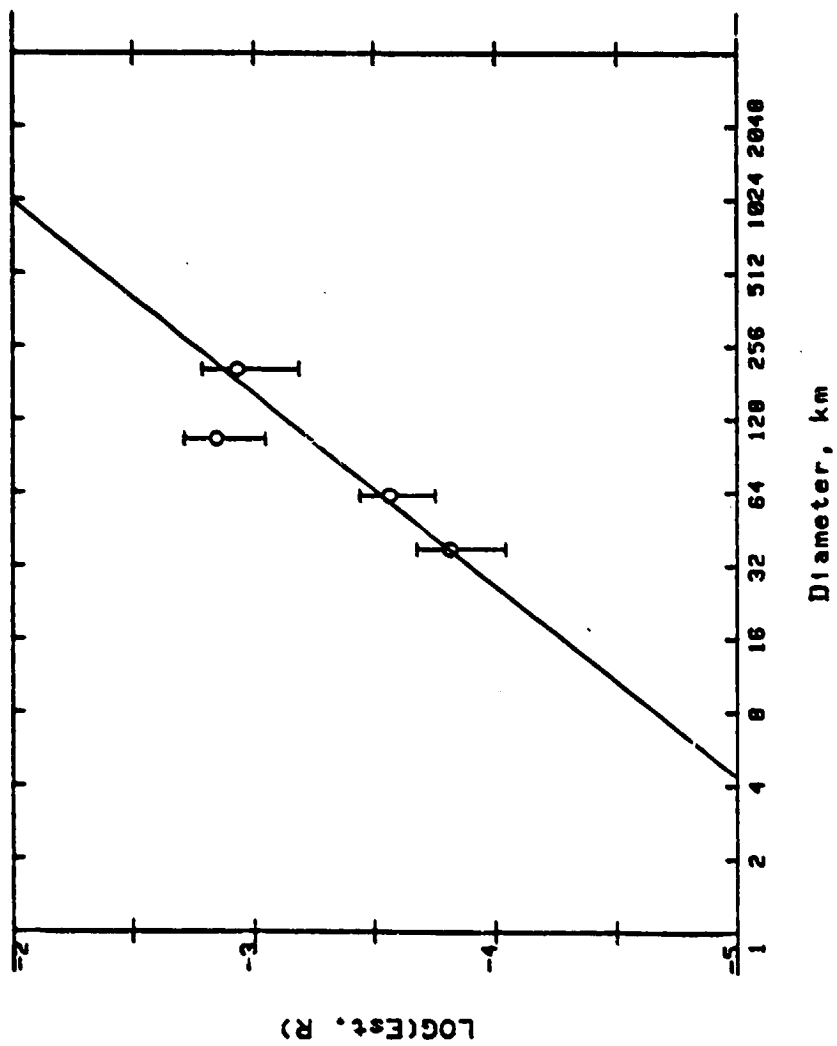


FIGURE 12(b):

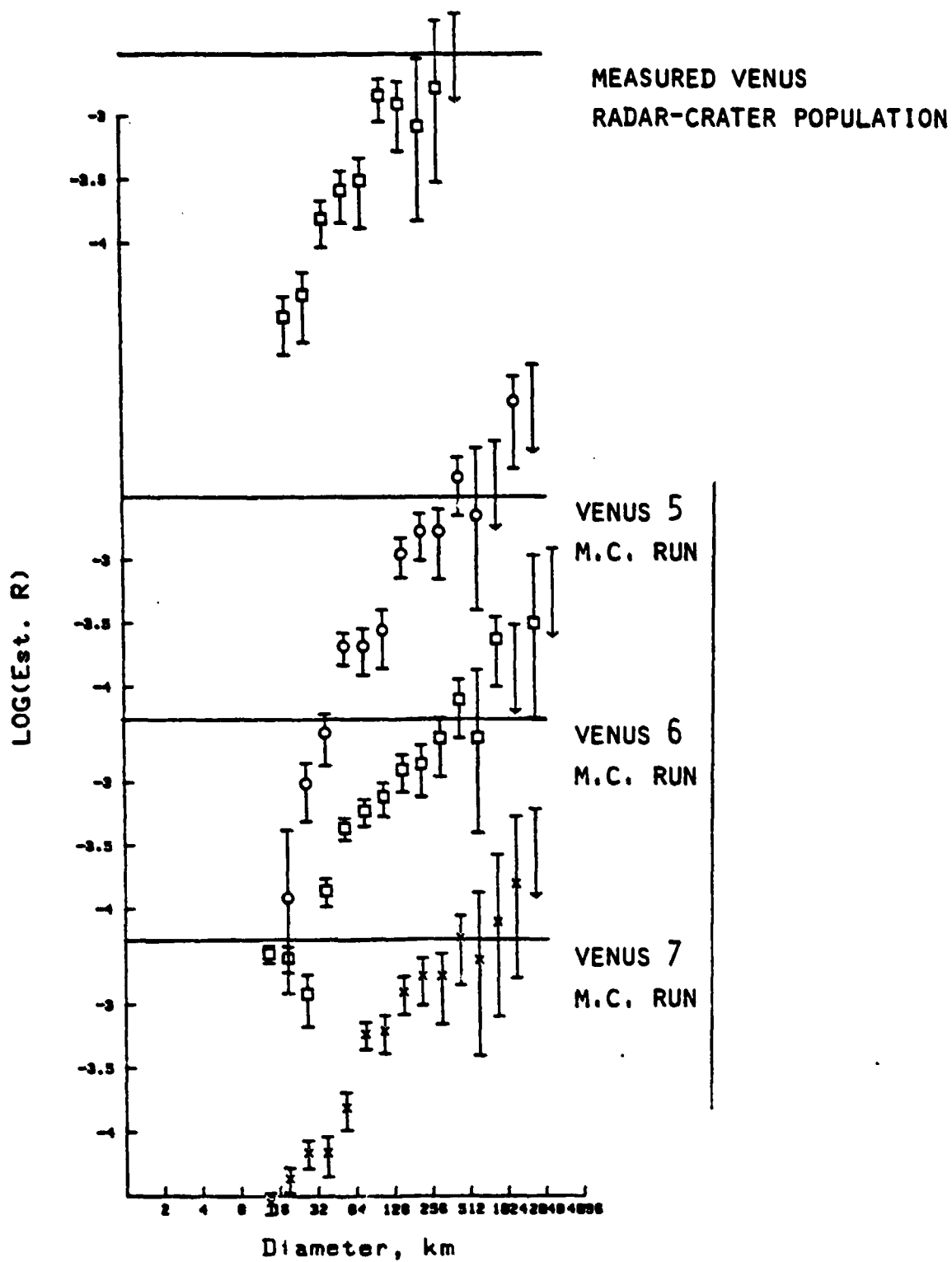


FIGURE 13(a):
COMPARISON OF MEASURED VENUS RADAR CRATER POPULATION WITH
MONTE CARLO SIMULATIONS.

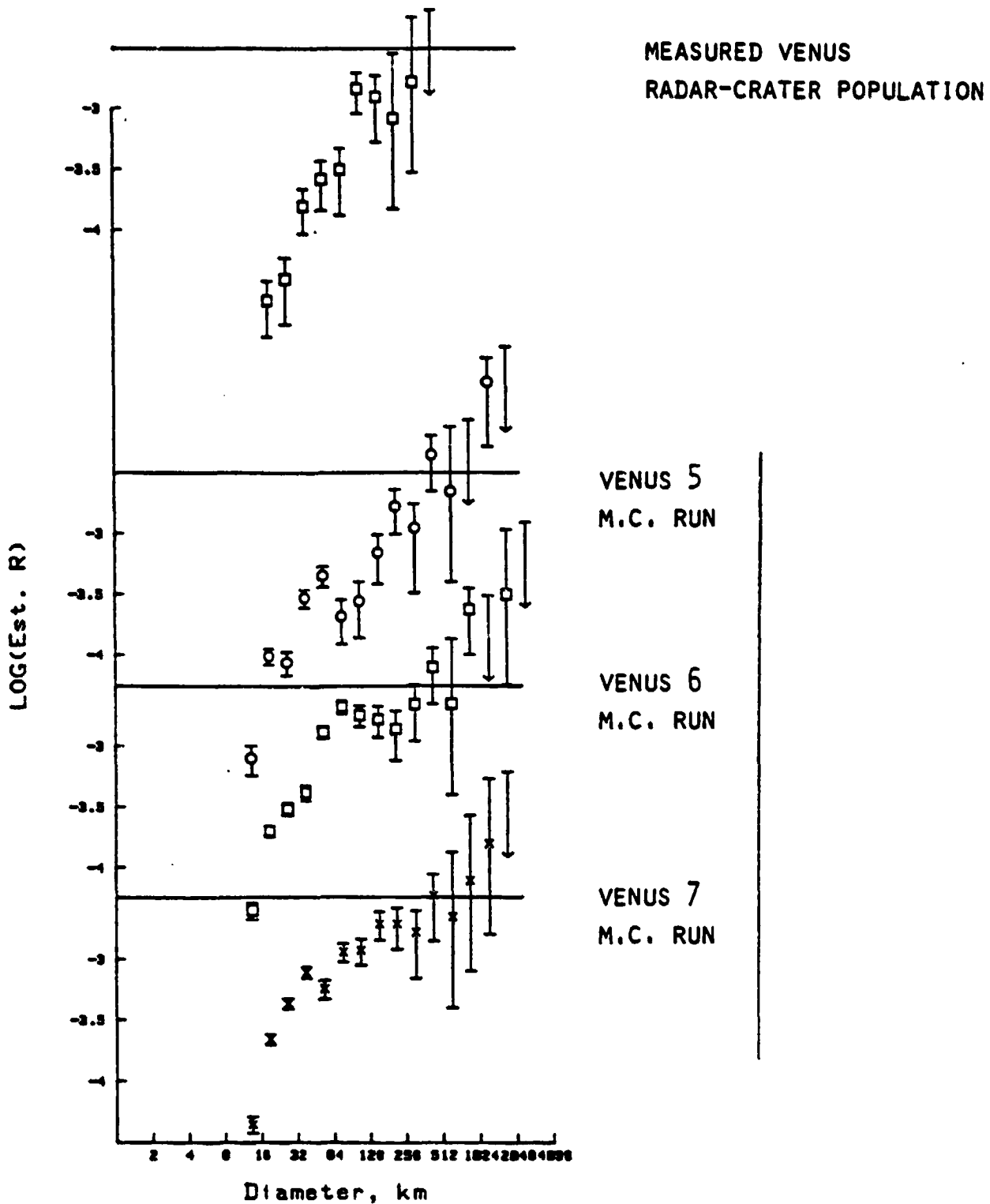


FIGURE 13(b):
COMPARISON OF MEASURED VENUS RADAR CRATER POPULATION WITH
MONTE CARLO SIMULATIONS.

APPENDIX B

LUNAR CRATERS WITH RADAR BRIGHT EJECTA*

T.W. Thompson (1,2)
S.H. Zisk (3)
R.W. Shorthill (1,4)
P.H. Schultz (5)
J.A. Cutts (2)

- (1) Visiting Scientist, Lunar and Planetary Institute, Houston, TX 77058
- (2) Planetary Science Institute, Science Applications Inc., Pasadena, CA 91101
- (3) NEROC Haystack Observatory, Westford, MA 01886
- (4) Univ. of Utah Research Institute, Salt Lake City, UT 84108
- (5) Lunar and Planetary Institute, Houston, TX 77058

Text: 28 pages

Figures: 13

Tables: 4

01 December 1980

Revised

01 April 1981

PSI Contribution #144

LPI Contribution #426

*Accepted for publication in ICARUS

ABSTRACT

A small fraction of the lunar impact craters with diameters of one kilometer and greater have extensive enhanced 3.8cm radar echoes associated with their ejecta deposits. The physical properties of these ejecta deposits and the ages of the central craters have been characterized via various infrared, radar and optical signatures. Most of these ejecta deposits are radar bright at the 3.8cm wavelength but are not radar bright at 70cm wavelength. Some ejecta have large infrared signatures, others do not. Although most of these ejecta have bright albedos in full-moon photographs, a significant fraction of the bright albedo markings do not extend beyond the crater.

This mix of remote sensing signatures indicates that craters with 3.8cm radar bright haloes are young and have ejecta deposits containing an excess of surface or near surface rocks relative to the surrounding terrain. Abundant centimeter-sized rocks are inferred from the high 3.8cm radar and infrared signatures. The low 70cm radar signatures indicate that larger blocks are much less numerous.

The population of craters with 3.8cm radar bright craters on the moon is much smaller than the population of craters in a similar size range on a young mare (Oceanus Procellarum) and has a different slope. We interpret this population as a steady-state population reflecting a balance between the production of fresh craters and the destruction of the high infrared and radar signatures by small-scale cratering. We attribute the slope of difference between visual and radar craters to more rapid destruction of the radar signatures in smaller craters.

Relative densities of 3.8cm radar bright craters and mare craters are estimated to be $0.04^{+.016}_{-.012}$ at 4km diameter and $0.100^{+.07}_{-.04}$ at 32km diameter. Assigning ages on the basis of these relative densities raises the question of whether the 4km-32km diameter visual crater population is truly representative of a 3.3 BY age. If it is, and if crater rates between 3.3 BY and the present have been uniform, then the 3.8cm radar crater lifetimes are estimated to be $0.13^{+.05}_{-.04}$ BY and $0.03^{+.23}_{-.013}$ BY at 4km and 32km diameter respectively. Similarly, lifetimes of the infrared signatures of 4km diameter craters may be as short as 10^7 years. However, some data suggest that these estimates may be in error by a factor of five too small.

Comminution of blocky ejecta material and the smoothing of slopes by lunar surface processes could account for the elimination of radar signatures on these time scales and the development of a steady-state crater population. An alternative interpretation, which we do not favor, is that the 3.8cm radar bright crater population is formed by a subpopulation of primary bodies or by secondary cratering.

I. INTRODUCTION

A remarkable feature of the 3.8cm radar maps of the moon obtained during the late 1960's (Lincoln Laboratory, 1968) are bright halos centered on impact craters and having ten or even twenty times the diameters of the central craters. In this paper, we attempt the first systematic compilation of these features and we assemble supporting 70cm radar, thermal infrared, and photo-geologic data to assist in their interpretation. Our primary motivation for this investigation was to develop a better understanding of the physical properties of the ejecta deposits around impact craters that give rise to bright halos and to study the rate and manner in which these physical properties changed with prolonged exposure on the lunar surface. In addition we were interested in developing further constraints on the mechanism of ejecta emplacement and to search for changes in ejecta deposition due to substrate materials and geologic structure.

II. BACKGROUND

The first high-resolution radar maps of the moon were obtained in the late 1960's using the Haystack 3.8cm radar (Lincoln Laboratory, 1968). These first maps showed a number of areas that had strong echoes and were several tens of kilometers in diameter centered upon smaller (one to ten km diameter) craters. Eighteen of these features were studied in detail by Thompson, et al., (1974), who showed that they had little or no 70cm radar enhancement but in some cases had infrared enhancements in earth-based eclipse observations. Thompson et al., (1974) inferred that these bright features in the 3.8cm radar images originated from strewn fields of centimeter-sized rubble.

An outstanding example of these features is the 4.9km diameter crater Piton B, shown in Figure 1. Figure 1A shows a 3.8cm radar map (ZAC 4.11) of Piton B and its environs. Piton B has a bright halo with echoes 4 to 8 times stronger than nearby areas that extends ten crater radii from the center. A faint halo with echoes 1 to 2 times stronger than the background extends twenty crater radii from the center. We examined the 70cm and infrared eclipse temperature maps of Piton B (see Thompson, 1974 and Shorthill, 1973). The 70cm radar echo power is 4 to 8 times that of nearby areas and is localized to the crater. The infrared eclipse-temperature enhancement is 28°K and appears to extend three crater radii from the crater. Earth-based and Lunar Orbiter IV photographs of Piton B (Figures 1B and 1C) shows no unusual morphology. In the full-moon photograph, the bright spot associated with Piton B is localized to the crater itself and the bright ray pattern usually associated with pristine craters is essentially absent. A feature similar to Piton B occurs in the north rim of Cassini where a 18km diameter spot in the 3.8cm radar image is centered on a 3km crater.

Other examples of these features are shown in Figure 2, which shows six prominent 3.8cm radar bright haloes for the lunar area encompassing western Mare Serenitatis and northern Montes Appeninus. Note that the 3.8cm haloes extend beyond the craters by many crater radii; and are larger than the full-moon ray patterns in the earth-based photograph.

Fig 1

Fig 2

A goal of this study was to extend our knowledge of these craters by cataloging their occurrence and their infrared, radar and optical properties. Some 120 of these craters were cataloged for the $1.2 \times 10^7 \text{ km}^2$ of the lunar surface which is covered by the LAC maps. The infrared and radar signatures of these special lunar craters provide insights into the physical properties of fresh crater ejecta. Our use of earth-based infrared and radar signatures to estimate crater ejecta characteristics is similar to a recent study of Aristarchus and small western mare craters by Schultz and Mendell (1978). They used high resolution, Apollo 17 orbital infrared data, (Mendell and Low, 1975), which observed nighttime (pre-dawn) lunar surface temperatures which are controlled by surface rocks larger than 30cm. Here we use the earth-based infrared eclipse and short (3.8cm) and long (70cm) wavelength radar data to investigate the physical properties (surface roughness and block populations) of crater ejecta deposits.

III. CATALOG AND STATISTICS OF CRATERS WITH RADAR-ENHANCED EJECTA

As described above, previous studies of the craters with 3.8cm radar bright ejecta considered only eighteen craters. Thus, a major question is how many of these craters exist and what are their visual, infrared, and radar characteristics? To answer this question, craters from the 3.8cm radar maps were selected and their characteristics cataloged. The primary data source is the earth-based 3.8cm radar images obtained at the NEROC Haystack Observatory (Zisk, et al., 1974). The 3.8cm radar data are complemented by earth-based 70cm radar images obtained at the Arecibo Observatory (Thompson, 1974) and the earth-based infrared eclipse temperatures (Shorthill, 1973). The optical properties of these features were obtained from Lunar Orbiter IV photography (Bowker and Hughes, 1971), full moon photographs of the Consolidated Lunar Atlas (Kuiper, et al., 1976), and Apollo orbital photography where available. Also observations by the Apollo Infrared Scanner (Mandell and Low, 1975) provides information about the physical properties of the ejecta of these craters.

These data have a range of resolutions. Resolution for the optical data is about 0.05km and 0.5km for the Lunar Orbiter IV and Consolidated Lunar Atlas photographs, respectively. Resolutions for the 3.8cm and 70cm radar data are 2.0 and 7.5km, respectively. Resolution for the earth-based infrared data varies between about 15km at the disk center to about 30km toward the limb; resolution of the Apollo Infrared Scanner was 7.0 kilometers. (The infrared and radar resolutions are the projected surface size of a point target and are about one-half of a line-pair resolution.) The 70cm radar and infrared resolutions are considerably poorer than the 3.8cm radar resolution; some of the consequences of these coarser resolutions are discussed in Appendix A.

The selection of craters was based solely on 3.8cm radar image size and crater diameter. Only craters with a 3.8cm radar image size greater than 20km and more than twice the crater diameter were included. The lower limit of 20km for 3.8cm radar halo size was chosen such that the smallest halo would be covered by at least one infrared resolution element and a

few 70cm radar cells. Similarly, limiting the halo size to twice the crater diameter was used to exclude large craters with narrow radar bright haloes. This focused our attention on craters with sizes up to about ten kilometers, although a few larger craters with very broad radar bright ejecta deposits were included. The selection criterion are illustrated in Fig. 3. We cataloged some 120 craters as shown in Figure 4 for the $1.2 \times 10^7 \text{ km}^2$ of lunar surface covered by the LAC charts. Limb areas beyond the LAC chart were not cataloged because there are no 70cm radar maps of these areas. The catalog area covers some 63 percent of the earth visible himisphere.

The diameters of the radar haloes associated with these craters in the 3.8cm and 70cm images were measured from both continuous tone and incremented displays of the data similar to those shown in Figures 1 and 2. Depolarized radar data were used to reduce possible confusion between slopes and roughness (Thompson and Zisk, 1972). Infrared halo diameters were measured on a contour map which was quantized to 4°K , about twice the noise level in the original data. Measured infrared and 70cm diameters were reduced by the resolution size to account for resolution smearing effects. Sizes of the photometrically bright areas associated with these craters were taken from the full-moon plates of the Consolidated Lunar Atlas (Kuiper, et al., 1967). Sizes of optically bright haloes associated with these craters in Lunar Orbiter photographs were measured where they occurred. Crater diameters were taken from the LPL Catalog (Arthur, et al., 1963, 1964, 1965 and 1966) or from the Lunar Orbiter IV photographs (Bowker and Hughes, 1971). Crater settings were identified as either mare or terra.

The peak intensity (strength) of the radar and infrared signal from the halo was also measured from the data described above. Where the halo was resolved by several resolution elements (most 3.8cm measurements) this strength measurement is dominated by the signal returned from the crater floor and rim. Where the halo was not resolved, the floor, wall, rim zone and ejecta of the crater all contribute to the measured value. In these cases the strength measurements provides a constraint on halo sizes as described in Appendix A. Radar strengths are in terms of enhancements relative to a background while infrared strengths are in terms of temperatures (in $^\circ\text{K}$) relative to terra areas at the same angle of incidence.

IV. 3.8cm RADAR BRIGHT EJECTA CRATER CHARACTERISTICS

The infrared, radar, and visual signatures of these craters can be interpreted in terms of surface characteristics. However, these interpretations may not be unique. The coarse resolution of some data means that the detailed size, shape and intensity of the corresponding signature is not well defined for smaller craters. Even where size, shape and intensity can be exactly specified, the implications for surface properties can be ambiguous. These limitations are not fatal, and in practice, the combination of several signatures provides a clearer picture of surface conditions than just one signature by itself.

The cataloging effort mentioned above provides a large data base for describing the surface properties of fresh crater ejecta. Whereas, Thompson et al. (1974) studied only eighteen craters, this report is based upon 120 craters. To show the signatures of these 120 craters in a meaningful way, the data are plotted as scatter diagrams of the strengths and halo sizes versus crater diameter in Figures 5, 6 and 7, and as crater size-frequency distributions using the Relative Size-Frequency Distribution Plots proposed by the Crater Analysis Techniques Working Group (1979) as shown in Figures 8 and 9.

Radar and Infrared Halo Diameters

The size of the measured 3.8cm ejecta haloes ranged from 2 to 35 times the diameter of the central crater (Fig. 5a). The lower limit in the scatter plot was set by the criteria used to select the crater data set (Fig. 3). Radar bright haloes at 70cm wavelength are much less extensive than the 3.8cm radar bright haloes except for craters larger than 30km where the 70cm and 3.8cm haloes are approximately equal. The infrared images show a spectrum of behavior. Some craters have large infrared haloes with sizes up to twenty crater diameters while other craters have no infrared haloes at all.

There are two kinds of problems with the diameter measurements presented in Figure 5a which are imposed by the intensity and spatial resolution of the data. The limited intensity resolution of all data sets restricted our ability to determine exactly the diameter of the crater haloes. The enhanced signature does not cut off abruptly at some distance from the

crater; it fades away gradually. Clearly, the point at which the signature drops below the threshold of recognizability depends on the signal-to-noise of the observation. The spatial resolution limitations of the IR and 70cm data compounds this problem for all but the very largest craters. These limitations must be understood before attempting to interpret the data presented in Figure 5. In particular, there are large uncertainties in all IR halo diameters below 40km and in 70cm radar diameters below 20km. However, strength measurements help constrain the size of small crater haloes which appear as only an unresolved bright spot in the IR and 70cm maps (see Appendix A).

Radar and Infrared Crater Strengths

The strength as used here is the peak signal from the crater feature relative to background. The strengths for the 3.8cm radar return (Fig. 6a) varies between 4 and 8. For most of the data points this value refers to the center of a resolved halo and is dominated by signal returned from the crater floor, wall and near rim regions. There appears to be no systematic dependence of this strength index on crater diameter.

In contrast with this behavior, the IR strength signatures (Fig. 6b) have a large scatter, which arises from a number of sources. In the largest craters which are resolved by the IR data, (say larger than 16km), the variation of 30°K to 45°K in the strength index may indicate real variability in the properties of crater floor and rim materials. In contrast, the radar enhancements of these larger craters varies little. For smaller craters, the resolution loss contributes to variation in the strength index, and observed temperature difference range from 5°K to 55°K . The theoretical curves in the IR strength index plot indicate the strength indices that would be observed from a crater of given diameter if the enhancement of 20°K , 40°K , or 60°K were confined to the crater interior. As noted, large crater interiors are not enhanced by more than about 45°K relative to their surrounds and it is difficult to conceive of physical properties of floor material which would give an enhancement of the crater interior exceeding 60°K . Evidently, most of these craters must have infrared enhancements extending well outside the crater and a number of them must have enhancements extending to a few tens of kilometers (see Appendix A). Unfortunately, we cannot uniquely

determine the IR halo diameters from strength measurements for the craters smaller than sixteen kilometers. There are indications from the measurements on larger craters that there are variabilities in the properties of floor and ejecta materials and this probably occurs with the smaller craters as well.

A different pattern of variation of the strength index with diameter appears in the 70cm radar data (Fig. 6c). In the larger craters which are resolved by the 70cm data ($D > 8\text{km}$) there is a fairly narrow variation in strength from 8 to 16 times background. For these resolved craters, the strength index refers to the properties of rim and floor materials; the small variability in these properties at 70cm resembles behavior at 3.8cm and contrasts with higher variability in the earth-based infrared data. For smaller craters, resolution affects the observed strength. To facilitate the interpretation of the resolution affected strength value, we have plotted predicted degraded strengths for craters with enhancements confined to the crater interior of 4 and 16 times the background. Most smaller ($D < 8\text{km}$) craters have enhancements less than that predicted, suggesting that these craters have little, if any, halo. However, a few of these smaller craters have enhancement larger than that predicted by our model, suggesting that these craters have 70cm radar haloes. Most of these enhancements are 2 or 4, which would be expected for haloes which extend beyond the central crater by only a few kilometers. Thus, the 70cm haloes appear to be much smaller than the 3.8cm haloes for these smaller craters. Again, ambiguities in the interpretation preclude a unique determination of the 70cm halo diameter from the 70cm signal strength.

Properties of Specific Craters

An appreciation of the effect of resolution on the signatures can be sharpened by a discussion of the properties of two craters.

The smallest crater in the present catalog ($\sim 0.7\text{km}$ diameter) is located at -50.4° , 0.2° and known informally as "Tiny Tim". The halo diameter of 40km at 3.8cm is well resolved by the radar data. The 3.8cm strength index is

4 times the background. The infrared halo is just resolved despite the small size of the central crater but the estimated diameter of 22km has a large uncertainty. The strength is at the low side of resolved craters although there are very few with which to compare in this size range. The crater is not spatially resolved in the 70cm data, but a 2 times signature is identified with the crater. Comparison with the theoretical curves indicates that at 70cm the halo radius is probably a few crater diameters in size (see Appendix A).

Linne', the crater pictured in Figure 2, is a 2.1km diameter crater located in Mare Serenitatis. The halo diameter of 40km at 3.8cm is well resolved. The 3.8cm strength index is four times the background. Thus, Linne' appears similar to Tiny Tim in the 3.8cm maps. Linne' is only marginally resolved in the IR data; however, the strength indices indicate an IR signature extending several crater diameters beyond the rim. Linne' is not spatially resolved at 70cm but the high strength index suggests a 70cm halo of a few crater diameters.

Summary

Our data on infrared, 3.8cm and 70cm radar lunar crater haloes provide some important constraints on the properties of these features despite degradation by resolution and selection effects. The 3.8cm haloes range up to thirty times the size of the craters itself. Although the strength of the 3.8cm signal returned from the crater and rim lies in a narrow range. For this population of craters, the infrared data indicates that the strength of the IR signature for the crater and rim area in large craters is much more variable than the comparable 3.8cm signatures. In larger craters, the IR bright halo extends to between 2 and 4 times the crater diameter. However, for some smaller craters, analysis of the strength data indicates that the IR haloes are generally smaller than the 3.8cm haloes. In general, the larger IR haloes are about one half as large as the 3.8cm haloes. The 70cm radar haloes are quite narrow and confined to no more than a few times the crater diameter.

Optical, Photogeologic and Population Characteristics

In addition to the infrared and radar signatures, other crater characteristics such as optical appearance, photogeologic interpretations, and crater populations are helpful in understanding the surface properties associated with craters with 3.8cm radar bright haloes.

Optical properties of 3.8cm radar bright ejecta craters were characterized by the size of the photometrically bright spots associated with these craters in the Lunar Orbiter IV photographs (Bowker and Hughes, 1971) and in the full-moon plates of the Consolidated Lunar Atlas (Kuiper, et al., 1967). These data are shown in Figure 7. Comparing these data with the 3.8cm radar halo sizes in Fig. 5a (the 3.8cm selection limits are shown in Fig. 7 to facilitate this), it is evident that a substantial number of craters with large 3.8cm radar bright haloes have very much smaller visible bright albedo features. Furthermore, there are a few craters with radar bright ejecta for which the full-moon albedo does not extend beyond the crater (like Piton B shown in Figure 1). On the other hand, many of these features have photometrically-bright ejecta in the low-sun Lunar Orbiter photographs; an expected signature for pristine lunar craters. Also a few of the craters, like M ltke, Copernicus H and Dionysius, have 3.8cm radar bright haloes and optically-dark ejecta in full-moon photographs. In view of the results of Fig. 5 and 7, it appears that a 3.8cm radar bright halo is a more reliable criterion for identifying fresh craters than is enhanced visual albedo.

Apollo Panoramic photography was used to test the correlation between 3.8cm haloes and fresh impact craters. A survey of Apollo 15, 16 and 17 photography identified pristine impact craters down to one-half kilometer in size. Without exception, impact craters with well-preserved ejecta facies (hummocky continuous deposits, ray streaks and ray patches) could be associated with a broad 3.8cm enhancement. Most of the bright-rayed craters smaller than 1km in diameter with 3.8cm enhancements were not included in the general survey since their 3.8cm halo sizes were smaller than 20 kilometers.

Both Apollo and Lunar Orbiter IV photography suggests that the 3.8cm radar bright halo craters are primary impacts. They have deep and symmetrical shapes while secondary craters tend to be shallow and assymeterical. Size considerations also suggests that the radar bright halo craters are primary since Secondary craters with diameters greater than one kilometer require primary craters with diameters of 50km or greater. Also, orbital infrared observations suggest that secondary craters are not blocky (Schultz and Mendell, 1978).

The general population properties of the 3.8cm bright craters have been examined using Relative Size-Frequency Distribution Plots proposed by the Crater Analysis Technique Working Group (1979). We plot $R = (\bar{D})^3 N / A (D_{\max} - D_{\min})$, where \bar{D} is the geometric mean of crater diameters, N is the number of craters, A is the area, and D_{\max} and D_{\min} are the maximum and minimum crater diameters in a size bin. A crater population which has a cumulative distribution proportional to (crater diameter)⁻² and a differential distribution proportional to (crater diameter)⁻³ plots as a horizontal line in a log (R) versus log (D) plot. Similarly, a crater population which has a cumulative distribution proportional to (crater diameter)⁻³ and a differential population proportional to (crater diameter)⁻⁴ has a slope of (-1) in a log (R) versus log (D) plot.

Figure 8 shows the Relative Crater Frequencies for the radar bright halo craters. Craters with infrared bright ejecta deposits form a subset of craters with 3.8cm radar bright ejecta deposits and consequently their relative crater density is smaller (Fig. 8a). Densities of mare craters with 3.8cm bright ejecta are indistinguishable from those on the terra (Fig. 8b). This is consistent with the notion that these craters have formed all over the moon at the same rate and that their occurrence is not strongly affected by peculiarities in the local geologic materials. Finally, the population density of 3.8cm radar bright craters (Fig. 9) is compared with the total population of photogeologically observed craters on one of the youngest lunar surfaces. It is seen to be substantially smaller (see also the plot in Fig. 4) and has a different slope; implications of this are explored in a later section.

V. ORIGIN OF ENHANCED SIGNATURES AND POSSIBLE IMPLICATIONS OF CRATER EJECTA EMPLACEMENT

The various crater halo signatures have implications for the physical nature and emplacement dynamics of crater ejecta materials. Our analysis of the Apollo photography indicated that all craters in our catalog with 3.8cm ejecta enhancements for which good imaging data exists are also photogeologically fresh. Consequently, we can draw on previous studies of young craters to assist us with our interpretations.

One of the key issues in the interpretation is relating 3.8cm radar brightness to surface conditions. Thompson, et al., (1974) suggested that excess surface and subsurface rocks with sizes of one to forty centimeters is the prime cause for enhanced 3.8cm radar echoes. However, Moore and Zisk (1973) showed that 3.8cm radar brightness did not correlate well with surface rock distributions in the vicinity of the Apollo 17 landing site at Taurus Littrow. Zisk, et al., (1977) suggested changes in surface chemistry as a cause for radar echo modulation, but that appears unlikely here. However, surface roughness at the space-regolith interface with scales of one to forty centimeters could cause the observed brightness in the 3.8cm radar images. A mound or cavity at the space-regolith interface is about as effective as a rock with the same size and shape in generating radar backscatter. Thus, the extremely broad 3.8cm haloes associated with crater ejecta may reflect a combination of both surface roughness and excess ejecta fragments with sizes of one to forty centimeters.

Studies of the High Resolution Apollo Orbital Data

Apollo photography and data from the Infrared Scanning Radiometer (ISR) on Apollo 17 are pertinent to consideration of these alternative models. Orbital photography suggests a transition in fresh crater morphology at about one or two kilometers in diameter (see Schultz, 1976). Small craters with diameters less than one kilometer exhibit broad, block-strewn ejecta fields where ejecta deposits have coarse, meter-sized fragments up to several crater radii from the rim. Craters larger than 2 kilometers exhibit a different morphology where meter-sized ejecta blocks are restricted to within a crater radius of the rim and a hummocky dune field of finer scale ejecta deposits extends to 2 to 3 crater radii beyond the rim (Table I).

Table I

Orbital Photography is complemented by the Infrared Scanning Radiometer data on Apollo 17 which observed predawn, nighttime temperatures which in turn are controlled by surface rocks larger than about 30cm in size. Studies of these data (Table I) indicate that the bright-rayed impact craters larger than about one kilometer display a blocky crater interior and near rim (within 0.3R of the rim) environment, but a relatively non-blocky ejecta facies beyond 0.5R of the rim (Schultz and Mendell, 1978). Thus, for craters larger than 1 to 2 kilometers, submeter to meter sized blocks are confined to within a crater radius and possible half a crater radius of the rim and an ejecta blanket of unknown physical properties extends several crater radii beyond the rim.

The 70cm data are consistent with the orbital infrared and photographic data which suggest that meter-sized blocks are confined to within about a crater radius of the rim. However, the 3.8cm data indicates blockiness or roughness in the size range of a few cm and larger extending to 10 or 20 crater diameters in some cases. The IR eclipse data which is specific to surface rocks 10cm in diameter and larger indicates that, for some of the 3.8cm radar bright ejecta craters, there is a blocky deposit extending to 10 crater radii or less for most craters larger than 2km. Craters smaller than 2km appear to exhibit blockier ejecta deposits out to greater relative ranges. These IR and radar observations suggest an idealized sequence for craters larger than 2km. The near-rim (within 0.5R) ejecta are composed of cm to meter-size blocks (70cm, IR, 3.8cm signatures) surrounded by ejecta deposits dominated by 10cm (lower limit for IR and no 70cm signature) to 40cm (upper limit for 3.8cm and no 70cm signature) size material out to about 5-6 crater radii. The outermost zone out to 20 crater radii is characterized by a relatively narrow range of material or surface roughness (1cm - 40cm range for 3.8cm signature).

Our observations are consistent with the observations of Schultz and Mendell (1978) and provide further information about the scale sizes of ejecta for craters larger than 2km in diameter. The Apollo infrared data indicated little meter-size debris beyond 0.5R from the rim, but the earth-based IR and 3.8cm radar data here suggest that smaller 10cm - 40cm debris

or surface roughness occurs beyond this zone, undetectable in the response of the Apollo infrared instrument. Thus, craters smaller than 1km display a broad field of meter and sub-meter size debris in the Apollo infrared data, orbital photography and in the new results here.

The 3.8cm radar enhancements associated with crater ejecta may have contributions from three possible sources. First, it may express small size ejecta (<50cm) that survived impact into the regolith and were scattered across the surface in the upper regolith. This mode of emplacement has been reproduced in the laboratory by clustered impacts (Schultz et al., 1980). Second, the halo may reflect extensive surface scouring and secondary cratering in the regolith by small (<10cm) size ejecta. Third, it may indicate impact fragmentation of larger ejecta that are then scattered downrange from the point of impact (Schultz and Mendell, 1978). The relative contributions of these processes to the origin of the 3.8cm halo requires further study including comparisons with experimental and theoretical models of ejecta emplacement.

An interpretation of earth-based and radar signatures based upon surface and subsurface rock populations and the hypotheses originally proposed by Thompson et al. (1974 and 1980) is given in Appendix B. This suggests that the youngest craters have large infrared strengths and sizes emanating from strewn fields of surface rocks which extend beyond the craters. Older versions of these craters have infrared enhancements which are confined to the crater interior and rim areas, but still have large 3.8cm radar bright haloes which arise from excess populations of buried centimeter sized rocks in the regolith.

The analysis of the various remote sensing signatures have been synthesized into models of the distribution of blocks and surface roughness in various ejecta zones for two size ranges of fresh craters (Table I). The ejecta characteristics of craters larger than 10km are similar to those between 2 and 10km, but the number of fresh craters in this size range included in this study is quite small. The principle conclusion is that blocks and other forms of roughness are enhanced in the ejecta and that the furthest ejecta has the smallest sizes. This is expected since the ejecta at these larger ballistic ranges has experienced larger mechanical comminution and larger peak shock histories than ejecta closer to the crater (Schultz and Mendell, 1978).

VI. AGE RELATIONSHIPS AND IMPLICATIONS FOR LUNAR SURFACE PROCESSES

The data described above indicates that the craters with bright 3.8cm radar haloes are young and they occur relatively infrequently. This suggests that the 3.8cm bright haloes are rapidly degraded by lunar surface process. We now examine the age of these radar bright craters and its implications about lunar processes.

Age relationships

Figure 9 shows the population of craters with 3.8cm bright ejecta as compared with the population of all craters on Oceanus Procellarum (Planetary Basaltic Volcanism Working Group, 1980). Power curves, which plot here as straight lines, have been least squares fit to the data (Table II). For the 3.8cm data, craters smaller than 4km have been excluded for reasons of both resolution loss and the selection effects that reduce the observed population below this diameter (Fig. 5). The least squares fit showed that the radar bright haloe craters with diameters of 4 and 32 kilometers occur 0.04 and 0.10 as frequently as all craters in Oceanus Procellarum with those sizes (Table III).

Guinness and Arvidson (1977) have compared small crater densities (0.83 - 1.843/km) at the Apollo 12 site in Oceanus Procellarum (Table 2) with crater densities of two other younger sites for which plausible radiometric ages exist. They concluded that the cratering rate has been uniform between 3.3 billion years (the data of the most recent flows at the Apollo 12 site) and the present. If we adopt this result and also assume that the visual crater population between 4 and 64km in Table 2 and 3 is representative of the 3.3 billion year age we infer lifetimes for the 3.8cm radar bright ejecta signatures are $0.13^{+0.05}_{-0.04}$ BY and $0.33^{+0.23}_{-0.13}$ BY for craters of diameter 4km and 32km respectively. Errors cited are formal statistical errors for the crater counts. Applying the same methods to the population with strong infrared signatures is difficult because this population is small and the larger crater sizes are affected by resolution loss at smaller crater sizes. However, assuming that the population at 4km is fairly complete (Fig. 8a), we infer that the lifetime of these 4km IR bright haloes of 3×10^7 years.

One problem with this analysis is that the reference population of 4km-32km diameter craters in Oceanus Procellarum probably includes a number of older craters that were only modified and not obliterated by the 3.3 BY flows. The fractional representation of older craters can be large because they

Table II

could include craters formed in a period before 3.3 BY when impacting rates were very much higher. Reinforcement for this view is provided by a comparison (Table II) of the Guinness and Arvidson estimates of crater density at 1km (we have converted our log R to their log A values) with extrapolations of the 4km to 32km crater counts of the Planetary Basaltic Working Group (1980). Assignment of reliable ages to these radar bright craters will require further improvements in our understanding of rates of production of 4km-32km diameter craters between 3.3 BY and the present. The Guinness and Arvidson values are a factor of five lower.

Shoemaker (1977) gives an estimate of the impact rate of Apollo-Amor objects in recent lunar history. His impact rate for our study area and ages of 3×10^7 years to 3×10^8 years gives estimated total numbers of craters which agree with the numbers of radar bright halo craters. We should point out that Apollo-Amor objects are only a subpopulation of all objects that impact the moon and the relative proportions of these to cometary objects is very uncertain (Wetherill, 1979, a and b).

Implications for Lunar Surface Processes

Let us consider whether the observed occurrence and lifetimes of 3.8cm bright radar craters are consistent with what we know about crater formation and lunar surface processes. The signature from 3.8cm bright halo craters is influenced by two major factors: the state of ejecta when it is originally emplaced and its subsequent gardening by meteoroidic bombardment.

From analysis of the IR and radar signature of crater haloes we conclude that the process of ejecta deposition results in some combination of excess blockiness and roughness compared to the mature regolith adjoining the ejecta blanket. One can plausibly argue that with exposure to meteoroidal bombardment at the lunar surface, rough ejecta surfaces are leveled by the rain spattering effect (Soderblom, 1970) and excess populations of surface and subsurface rocks disappear by impact fragmentation (Hörz et al., 1975; Gault et al., 1974). A reasonable scenario attributes the enhanced IR and radar signatures to rocks, that the IR signature disappears first as surface rocks are broken down and the 3.8cm signature disappears later as the buried rocks are exhumed and ruptured. This would explain why the IR bright ejecta deposits are only a subset of the craters with 3.8cm bright ejecta. Buried centimeter-sized rubble is the most probable source of the haloes with 3.8cm radar enhancements and no infrared enhancement.

If this scenario is correct, then rock comminution rates provide another method of estimating the lifetimes of the 3.8cm radar and IR signatures of ejecta deposits. In particular, the lifetimes of the infrared and radar signatures of these features depend upon the rate at which surface rocks are catastrophically ruptured, as well as the rate at which the lunar regolith is turned over. The former has been modelled by Hörz et al. (1975), who showed that a centimeter-sized rock will survive 10^8 years. This model suggests that the radar bright halo craters with large IR signals and size have ages of $10^7 - 10^8$ years. After $10^7 - 10^8$ years, the radar enhancements associated with the ejecta will be controlled by gardening of the regolith. The models of Gault et al. (1974) provide an estimate for the lifetimes of these older (but still radar enhanced) ejecta, since they show that the first meter of the lunar surface is turned over once every 10^9 years. This model suggests that the older radar bright ejecta will have ages less than 10^9 years. Thus, these model data are consistent with the inferred lifetime of $\sim 10^7$ years for the infrared halo which is associated with surface rocks and with the inferred lifetime of 1.3 to 3.3×10^8 years for the 3.8cm halo which can be associated with both surface rocks and subsurface rocks. However, detailed modelling of the evolution of an ejecta layer under meteoroidal processes and rigorous computations of the signatures from a terrain with a population of surface and buried rocks is needed to demonstrate quantitative agreement. Also, differences in the lifetimes of enhancements around large and small craters may arise from differences in thickness and initial size distributions of ejecta.

Another important point is that the evolution of the infrared and radar signatures for the haloes is possibly size dependent. Smaller craters will probably lose their radar and infrared bright haloes faster than larger craters. Although the size-frequency distributions of these craters with bright haloes will depart from the classical photogeological "production" and "steady-state" distribution, they may still represent a steady-state population. This occurs for the infrared and radar signatures of crater interiors (Thompson et al., 1980) and appears to occur for crater ejecta also (Fig. 9). However, the sampling criterion for radar craters changes at 10km in the existing data set and a more careful analysis of this on the population slope should be performed.

In summary, various arguments suggest that infrared and radar bright ejecta have lifetimes which depend upon crater size. Larger craters have longer lifetimes than smaller craters. A least squares fit of the crater size-frequency data suggests lifetimes of 1.3 to 3.3×10^8 years, which is consistent with Apollo-Amor impact predictions of Shoemaker (1977) as well as a rock comminution processes models of Hörz et al. (1975) and the regolith gardening models of Gault et al. (1974).

VII. CONCLUDING REMARKS

The data and analyses presented above suggest that lunar craters with large, bright radar and infrared haloes are the younger features on the moon and probably no older than 10^7 to 10^9 years (depending upon both size and their infrared and radar signatures). The enhanced radar and infrared signatures from the ejecta deposits of fresh craters are produced by various combinations of enhanced blockiness and roughness. With exposure to lunar surface processes, roughness and blockiness is restored to the value typical of the surrounds and the remote sensing enhancement disappear.

There are a number of future studies which would shed even more light on these features. (1) Our small size limit of 20kms should be decreased to about 10kms and our large size limit of (2 x crater diameter) should be eliminated entirely. (2) New 70cm radar and infrared images with resolutions on the order of 3km would yield better estimates of halo size and strengths. (3) Models for crater ejecta emplacement need to be improved to understand how much ejecta is emplaced and also to understand what ejecta rock-size distributions are. (4) Models for regolith generation need to be improved to understand how rock populations in crater ejecta blankets evolve with time. And, (5) electromagnetic scattering theory needs to be improved to better understand how radar enhancements relate to surface and subsurface rock populations. (Items 2, 4, and 5 are also needed to further our knowledge about the evolution of the radar signatures of crater interiors described by Thompson et al., 1980).

APPENDIX A

RESOLUTION EFFECTS AND INTERPRETATION OF INFRARED AND RADAR
SIZES AND STRENGTHS

The crater halo features discussed in this paper range in size from features thirty times the spatial resolution of the data to features with sizes that are believed to be some fraction of the resolution of the data. Resources did not permit a sophisticated image restoration for features near the resolution limit. Instead, we used some first-order estimation methods to correct for the effects of resolution and to test hypotheses about the sources of signals.

A basic resolution correction applied to all the data and reflected in the halo diameter plots of Fig. 5 was to subtract the nominal resolution of the instrument from the apparent size of the crater halo. This unsophisticated correction allows us to demarcate those features which are essentially unresolved by the instrument and those which are resolved. Obviously, the "corrected" diameters of features originally near the resolution limit are still highly uncertain and the apparent sizes may depend on the areal intensity of the signal.

For the IR and 70cm radar signatures the resolution is only adequate to clearly define the diameters of haloes of a few tens of kilometers (Fig. 5). However, information on the strength (intensity) of an unresolved halo can be used to place constraints on the size of that halo using plausible assumptions about the distribution of the signature enhancement in the crater and crater surroundings.

The method of using signal strengths to define halo size can be illustrated with the earth-based infrared data. Assume that a small crater has a enhanced IR response which is significantly smaller than the instrument resolution. A simple model for the observed strength assumes that the infrared signal arises from a circular area of uniform temperature imbedded in a circular resolution element. Then

$$(T_b + \Delta T_o)^4 = T_b^4 [1 - (D^2/R^2)] + (T_b + \Delta T_c)^4 (D^2/R^2) \quad (A.1)$$

Where T_b = Temperature of the background = 250°K

ΔT_o = Observed temperature difference

ΔT_c = True temperature difference of the central area

D = Central area diameter, and

R = Resolution = 22.5 km

Equation A.1 was used to compute the diminution of IR strength with crater size shown as the solid lines in Fig. 6b.

The term D in equation A.1 is the central area diameter and does not have to equal the crater diameter. Instead, it may include a substantial part of a broader ejecta deposit. Thus, the problem here is now to constrain this diameter D based upon observed temperature differences. Solution of equation A.1 for the true temperature difference of the central area (ΔT_c) yields:

$$(T_b + \Delta T_c)^4 = T_b^4 - (R^2/D^2) [(T_b + \Delta T_o)^4 - T_b^4] \quad (\text{A.2})$$

The infrared data shown in Figure 6b indicate that ΔT_o , the observed temperature differences for many craters range from 10°K to 50°K . In Fig. A.1, central area temperatures are shown as a function of observed temperatures and central area size. Note that these predicted central area temperatures increase sharply for the smaller central area sizes.

Observations of large craters where the central area is resolved show no temperature differences larger than 55°K . These larger craters are older and the infrared enhancement may have weakened from our original, higher value. Here, we will arbitrarily assume that the central areas cannot have temperatures greater than 350°K (only 50° colder than the pre-eclipse background). The data shown in Fig. A.1 indicates that the central infrared bright areas must be 5km in diameter or larger if the observed temperature differences is greater than 10°K and if the central temperature differences do not exceed 100°K . If the observed temperature differences are near 50°K , then the central area must be sixteen kilometers or greater.

Fig A.1

This assumed a simple case where the infrared bright area is confined to a central areas. It is more likely that the bright areas gradually fade out for ejecta areas further from the crater. However, the simple model does illustrate that it is likely that the craters with observed temperatures of 10°K or more greater than their environs have central enhanced areas with sizes determined from the contour plots of the infrared data (Fig. 5b).

These arguments which were just applied to the earth-based infrared data can be applied to the 70cm radar data as well. For the 70cm data there are few craters with enhancements greater than that predicted assuming that enhanced region is confined to the crater itself. However, there are enough exceptions to this that the minimum sizes should be computed for this wavelength also.

For the 70cm radar case we assume that the radar enhancement arises from a central circular area imbedded in a square resolution element. Here:

$$\beta_{\text{obs}} = 1 + [(\alpha_c - 1)(\pi/4)(D^2/R^2)] \quad (\text{A.3})$$

where β_{obs} = observed enhancement

α_c = the enhancement of the central area

D = central area diameter

R = resolution = 7.5km

Equation A.3 was used to compute the diminution of radar intensities for resolution effects shown as the solid lines in Figures 6a and 6c.

Once again, the diameter D is for the radar bright area which may be larger than the crater. The enhancement for the central area, α_c , is given by:

$$\alpha_c = 1 + [(\beta_{\text{obs}} - 1)(4/\pi)(R^2/D^2)] \quad (\text{A.4})$$

The observed 70cm radar enhancements vary between 2 and 8 times yielding the predicted enhancements shown in Figure A.2. Once again the predicted enhancements have a strong dependence upon central area diameter.

Fig A.2

C-2

The curves plotted in Figure A.2 in turn yield estimates of central area sizes. Here we assume that central area enhancements cannot exceed 32, a reasonable value based on observations of larger, resolved craters. Note that Figure 6c shows six craters with diameters between 0.7 and 2.0 kilometers which have observed enhancements of 2.0 times the background. The 70cm radar bright areas associated with these craters must come from areas at least 1.5 kilometers in diameter based upon the curves in Figure A.2 associated with the observed enhancement of two. Similarly, Figure 6c shows about ten craters with diameters between two and four kilometers and observed enhancements between four and eight times the background. The 70cm radar bright areas associated with these ten craters must be 3.0 kilometers and greater based upon the curves for the observed enhancements of 4 to 8 in Figure A.2.

Thus, the 70cm strength values are consistent with a simple, first-order model where the high reflectivity areas are confined to the crater interior and its near-rim region. This is, of course, one extreme in a spectrum of models. At the other extreme, one permits high reflecting areas to be as large as those plotted in Figure 5c, where, about ten craters with diameters between two and four kilometers have measured 70cm haloes on the order of fifteen kilometers. These are somewhat larger than that observed with Apollo Infrared Scanner.

In summary, it appears that the peak signal strength coupled with a simple first-order model yield consistent results between observed peak signal strengths and halo diameters. The smaller craters which are ten to fifty degrees warmer than environs have infrared haloes which are a few tens of kilometers in size. On the other hand, the smaller craters probably have 70cm radar enhancements which are confined to the crater interior and nearby areas.

APPENDIX B

INTERPRETATION OF THE INFRARED AND RADAR SIGNATURES OF CRATER
EJECTA IN TERMS OF SURFACE ROCKS

In Section IV of this report, the possible identification of surface conditions associated with the 3.8cm radar bright haloes are presented. In this Appendix one of these possible identifications is examined in detail. This is based primarily upon the hypothesis developed by Thompson, et al. (1974 and 1980). Thompson, et al. (1980) discussed how the infrared and radar signatures of lunar craters evolve with time in response to lunar surface processes such as meteoroidic bombardment. In addition, Thompson, et al. (1974) described how the infrared and radar signatures can be related to surface and subsurface rock distributions. A question here is whether the infrared and radar signatures of radar bright ejecta have an analogous evolution.

A background for this discussion is provided by the relations of the infrared and radar signatures to subsurface and surface rock distributions originally proposed by Thompson, et al. (1974). Briefly, infrared and radar signatures are characterized as either bright (stronger than nearby areas) or faint (equal to nearby areas). Bright radar signatures implies enhanced populations of surface and/or subsurface rocks with sizes between one-quarter and ten radar wavelengths, buried no deeper than fifty radar wavelengths. Similarly, bright infrared signatures implies enhanced populations of surface rocks greater than 10cm in size. This, for the most part, ignores 3.8cm radar brightness roughness at the space-regolith interface.

Various combinations of these infrared and radar signatures in turn imply various types of surface and subsurface rock populations in the ejecta. The ejecta are 3.8cm radar bright by definition. However, the data in Figure 5 suggest that the ejecta have little or no 70cm radar enhancements. This implies that centimeter-sized rocks occur more frequently in and on the ejecta, while meter-sized rock populations are not enhanced relative to nearby areas. Infrared signatures permit one to assign the excess centimeter-sized rocks to the surface or subsurface. A bright infrared signal from the ejecta implies excess surface rocks while a faint infrared signature with a bright 3.8cm radar signature implies excess centimeter-sized rocks within

the first two meters of the subsurface. In contrast, the strength data in Figure 6 are consistent with a model where the crater interior and outer wall are bright at all three wavelengths implying that these areas have excess surface rocks of centimeter and meter sizes.

The infrared and radar signatures of crater interiors evolve with time such that the younger craters have both infrared and radar enhancements while older craters are only radar bright (Thompson, et al., 1980). Perhaps crater ejecta evolves in a similar manner. A model of crater evolution based on these considerations is shown in Figure B-1. The youngest features would have a large infrared and 3.8cm radar haloes emanating from large ejecta fields of surface centimeter-sized rubble. A feature with an intermediate age would retain a large 3.8cm radar halo emanating from buried centimeter-sized rubble accompanied by a small infrared halo confined to crater interior. The evolution from the youngest to the intermediate age assumes that surface centimeter-sized rubble will be catastrophically ruptured by meteoroidic bombardment while buried centimeter-sized rubble will be protected (see Hörz et al. 1975, and Thompson et al., 1974 and 1980). The evolution from intermediate age to the oldest of these features is characterized by a loss of the 3.8cm radar halo. The craters of our model retain an infrared and radar bright interior, whose evolution to even older forms is described by Thompson et al. (1980).

This model for the evolution of radar bright haloes is consistent with the data, particularly the range of infrared signatures. Our catalog of 120 covers only the youngest and intermediate features (the older craters with infrared and radar bright interiors and their distributions on the lunar surface are discussed by Thompson, et al., 1980). We selected some 38 candidates for the youngest features based upon their infrared halo size and infrared strength relative to other craters with the same sizes. (Craters with diameters greater than 8 km were arbitrarily dismissed since all of these larger craters had similar 3.8cm, 70cm and infrared characteristics.) These craters are given in Table B-I and their size-frequency distribution is shown in Fig. 8a.

All of our candidates for the youngest craters in this evolution model have large infrared strength and halo diameters. The infrared

Fig B.1

Table B-I

strengths are well above that expected if the infrared signal were confined to the crater interior. In general, the infrared haloes for these craters are about one-half the size of the 3.8cm halo. The furthest portions of the ejecta are only 3.8cm radar bright. In addition, some of these candidates for the youngest craters have relatively strong 70cm signals and halo sizes which would be expected for the youngest craters of any size.

The crater statistics of these candidates for the youngest lunar craters are compared with the overall statistics of craters with radar bright ejecta in Figure 7. For smaller craters with diameters between one and four kilometers only the youngest craters have 3.8cm radar haloes with diameters of twenty kilometers or more. Older craters in this size range probably have smaller 3.8cm haloes which were arbitrarily dismissed by our selection criterion. On the other hand, craters with diameters between four and eight kms show a range of behaviors between the youngest and middle-age members of the proposed evolution shown in Figure B1.

This model of crater evolution depends solely upon the association of infrared and radar signatures with surface and subsurface rocks given in Table B1. An alternate explanation for high radar echoes invokes surface roughness at the space-regolith interface. Both cavities or mounds at this interface with centimeter scale would create radar backscatter comparable to rocks with the same sizes. It is possible that some of the high radar echoes associated with the ejecta may be coming from this type of surface structures as described in Section IV of this paper.

An example of an intermediate age feature is Lichtenberg B shown in Figure B2. The 3.8cm radar halo has a diameter of 40km and extends to the furthest surface features associated with ejecta emplacement. However, the infrared and 70cm radar halo are 8km and 10km respectively and extend no further than the raised rim of the crater. If this evolution model is correct, then Lichtenberg B originally had an infrared halo which was a

few tens of kilometers in diameter and encompassed all of the surface expressions of the ejecta emplacement. This would have emanated surface rocks with centimeter sizes. These surface rocks were exposed to meteoritic bombardment and were catastrophically ruptured (Hörz et al., 1975) leaving smaller fragments which do not create enhancements during an eclipse. Today, this crater has a large 3.8cm halo presumably arising from excess centimeter-sized rocks buried in the ejecta. Also, the infrared and 70cm radar enhancements are confined to the crater and near-rim deposits indicating that these areas have excess numbers of surface meter sized blocks.

ACKNOWLEDGEMENTS

Crater population data for the lunar maria was provided to us by W.K. Hartmann who also guided us on suitable lunar crater data sets. We are also indebted to Mr. Steven Schlipf, Pasadena City College, for his careful reviews of our data, and to Mr. Blake Lewis of the Planetary Science Institute for the computer software which produced many of the figures in this report. This study made ample use of photographic displays of the infrared and radar data originally produced at IPL (Image Processing Laboratory) at the Jet Propulsion Laboratory, Pasadena, California, by Apollo Experiment S-217. This study also made use of the IR/radar crater catalog originally compiled by T.W. Thompson and W.J. Roberts of the Planetary Science Institute.

A portion of the research for this paper was done while two of us (R.W. Shorthill and T.W. Thompson) were Visiting Scientists at the Lunar and Planetary Institute, which is operated by Universities Space Research Association under Contract No. NSR-09-051-001 with the National Aeronautics and Space Administration. Two of us (T.W. Thompson and J.A. Cutts) were funded in part by NASA Grant NASW 3383.

This paper is Lunar and Planetary Institute Contribution 426 and Planetary Science Institute Contribution #144.

REFERENCES

- Arthur, D.W.G., Agnieray, A.P., Horvath, R.A., Wood, C.A., and Chapman, C.R. (1963). The system of lunar craters, quadrant I. Comm. of the Lunar and Planet. Lab., Contribution 30.
- Arthur, D.W.G., Agnieray, A.P., Horvath, R.A., Wood, C.A., and Chapman, C.R. (1964). The system of lunar craters, quadrant II. Comm. of the Lunar and Planet. Lab., Contribution 40.
- Arthur, D.W.G., Agnieray, A.P., Pellicori, R.H., Wood, C.A. and Weller, T. (1965). The system of lunar craters, quadrant III. Comm. of the Lunar and Planet. Lab., Contribution 50.
- Arthur, D.W.G., Pellicori, R.H., and Wood, C.A. (1966). The system of lunar craters, quadrant IV. Comm. of the Lunar and Planet. Lab., Contribution 70.
- Crater Analysis Techniques Working Group (1979). Standard techniques for presentation and analysis of crater size-frequency data. Icarus 37, 467-474.
- Bowker, D.E., and Hughes, J.K. (1971). Lunar Orbiter Photographic Atlas of the Moon (NASA SP-206), U.S. Gov. Printing Office, Washington, D.C.
- Gault, D.E., Hörz, F., Brownlee, D.E., and Hartung, J.B. (1974). Mixing of the lunar regolith. Proc. Lunar Sci. Conf. 5th, 2365-2385.
- Guinness, E.A., and Arvidson, R.E. (1977). On the constancy of the lunar cratering flux over the past 3.3×10^9 yrs. Proc. Lunar Sci. Conf. 8th, 2365-2385.
- Hörz, F., Schneider, E., Gault, D.E., Hartung, J.B., and Brownlee, D.E. (1975). Catastrophic rupture of lunar rocks: a Monte Carlo simulation. The Moon 13, 235-258.
- Kuiper, G.P., Whitaker, E.A., Strom, R.G., Fountain, J.W., and Larson, S.M. (1967). Consolidated Lunar Atlas. Lunar and Planetary Laboratory, Univ. of Arizona, Tucson.
- Lincoln Laboratory (1968). Radar Studies of the Moon, Final Report, vol. 2, M.I.T., Lexington, Mass.
- Mendell, W.W., and Low, F.J. (1975). Infrared orbital mapping of lunar features. Proc. Lunar Sci. Conf. 6th, 2711-2719.
- Moore, H.J., and Zisk, S.H. (1973). Calibration of radar data from Apollo 17 and other mission data. Apollo 17 Preliminary Science Report (NASA SP-330), 10-17.

- Planetary Basaltic Volcanism Working Group (1980). Chronology of planetary volcanism by comparative studies of planetary cratering. Basaltic Volcanism Study Project (draft).
- Schultz, P.H. (1976). Moon Morphology. University of Texas Press, Austin and London.
- Schultz, P.H., Gault, D.E., and Mendenhall, M. (1980). Multiple-body impacts: implications for secondary impact processes. In abstracts LPSC XI, 1006-1008.
- Schultz, P.H., and Mendell, W. (1978). Orbital infrared observations of lunar craters and possible implications for impact ejecta emplacement. Proc. Lunar Sci. Conf. 9th, 2857-2883.
- Settle, M., Cintala, M.J., and Head, J.W. (1979). Emplacement of Fahrenheit crater ejecta at the Luna-24 site. The Moon and the Planets 20, 281-300.
- Shoemaker, E.M. (1977). Astronomically observable crater-forming projectiles. In Impact and Explosion Cratering (D.J. Roddy, R.O. Pepin, and R.B. Merrill, Eds.), pp. 617-628, Pergamon Press, New York.
- Shorthill, R.W. (1973). Infrared atlas charts of the eclipsed moon. The Moon 7, 22-45.
- Soderblom, L.A. (1970). A model for small-impact erosion applied to the lunar surface. J. Geophys. Res. 75, 2655-2661.
- Thompson, T.W. (1974). Atlas of lunar radar maps at 70cm wavelength. The Moon 10, 51-85.
- Thompson, T.W., Masursky, H., Shorthill, R.W., Tyler, G.L., and Zisk, S.H. (1974). A comparison of infrared radar and geologic mapping of lunar craters. The Moon 10, 87-117.

Thompson, T.W., Cutts, J.A., Shorthill, R.W., and Zisk, S.H. (1980).

Infrared and radar signatures of lunar craters: implications about crater evolution. Proc. Lunar Highlands Crust Conf., 175-177.

Thompson, T.W., and Zisk, S.H. (1972). Radar mapping of lunar surface roughness. In Thermal Characteristics of the Moon (J.W. Lunas, Ed.), pp. 83-117. MIT Press, Cambridge and London.

Wetherill, G.W. (1979a). Steady state populations of Apollo-Amor objects. Icarus 37, 96-112.

Wetherill, G.W. (1979b). Apollo objects. Scientific American 240, 54-65.

Zisk, S.H.; Pettengill, G.H. and Catuna, G.W. (1974), High-resolution radar maps of the lunar surface at 3.8cm wavelength, The Moon, 10, 17-50.

Zisk, S.H., Hodges, C.A., Moore, H.J., Shorthill, R.W., Thompson, T.W., Whitaker, E.A., and Wilhelms, D.E. (1977). The Aristarchus-Harbinger region of the moon: surface geology and history from recent remote-sensing observation. The Moon 17, 59-99.

TABLE 1

SUMMARY OF DATA ON BLOCK POPULATIONS AND
SMALL-SCALE ROUGHNESS IN CRATER EJECTA DEPOSITS
AND SYNTHESIS

	PREVIOUS DATA	THESE DATA	SYNTHESIS
SMALL CRATERS (less than 1 to 2km)	<p><u>Apollo imagery (Schultz, 1976) indicate:</u></p> <ul style="list-style-type: none"> • broad block strewn ejecta fields containing meter-sized fragments extending several crater radii from the rim • no direct information about centimeter-sized blocks • dune field <p><u>ISR data (Schultz and Hendell, 1978) indicate:</u></p> <ul style="list-style-type: none"> • no information for craters in this size range 	<p><u>3.8cm data</u></p> <ul style="list-style-type: none"> • Enhanced halo extending up to 15 or 30 crater radii indicating: <ul style="list-style-type: none"> + enhanced centimeter-sized blocks on surface or buried + rough dune features + clods of fine ejecta <p><u>IR data</u></p> <ul style="list-style-type: none"> • Some haloes to 10 or 20 crater radii/others with smaller haloes <p><u>70cm data</u></p> <ul style="list-style-type: none"> • Must be smaller than a few radii 	<p><u>Near rim and inner zone out to 5 crater radii</u></p> <ul style="list-style-type: none"> • Blocks 30cm and larger enhanced relative to surroundings • Possibly centimeter to meter-sized roughness also enhanced <p><u>Outer zone beyond 5 crater radii</u></p> <ul style="list-style-type: none"> • 10cm to 40cm-sized roughness or • 18cm to 40cm-sized blocks • No meter-sized blocks • No meter-sized roughness
MEDIUM CRATERS (larger than 1 to 2km up to 10km)	<p><u>Apollo imagery (Schultz, 1976) indicate:</u></p> <ul style="list-style-type: none"> • meter-sized blocks restricted to within a crater radius of the rim • hummocky dune field of fine scale ejecta extending to 2 to 3 crater radii from the rim <p><u>ISR data (Schultz and Hendell, 1978) indicate:</u></p> <ul style="list-style-type: none"> • Information about blocks larger than about 30cm in size (decimeter) • crater interiors and rim areas have abundant decimeter-sized blocks • population of decimeter-sized blocks is typical of background beyond 0.5 crater radii 	<p><u>3.8cm data</u></p> <ul style="list-style-type: none"> • Enhanced halo extending up to 10 or 20 crater radii indicating: <ul style="list-style-type: none"> + enhanced centimeter-sized blocks on surface or buried + rough dune features + clods of fine ejecta <p><u>IR data</u></p> <ul style="list-style-type: none"> • Some haloes of enhanced IR emission inferred from strength data extending to at least 5 crater radii + enhanced population of rocks 10cm in size and larger <p><u>70cm data</u></p> <ul style="list-style-type: none"> • Narrow halo of enhanced 70cm emission + narrow halo of surface or buried rocks 40cm to 4m in size 	<p><u>Near rim <0.5R ejecta</u></p> <ul style="list-style-type: none"> • Centimeter to meter-sized blocks enhanced relative to surroundings • Centimeter to meter-sized roughness also enhanced <p><u>Inner zone 0.5R to 5 crater radii</u></p> <ul style="list-style-type: none"> • 10cm to 40cm-sized blocks • 18cm to 40cm-sized surface roughness • No meter-sized blocks or surface roughness <p><u>Outer zone beyond 5 crater radii</u></p> <ul style="list-style-type: none"> • 1cm to 40cm-sized roughness • 1cm to 40cm-sized buried blocks • No meter-sized blocks on

NOTES TO TABLE II:

(1) Several different schemes of expressing crater densities have been used in the literature. We have used the Relative Size-Frequency Distribution recommended by the Crater Analysis Techniques Working Group (1979) for our data. However, since we wished to compare these results with other workers we have computed equivalent incremental frequencies and cumulative numbers.

(2) The 4-6km population used here was based on published data in the Planetary Basaltic Working Group report (1980). We obtained the raw data from W.K. Hartmann. The counts were actually made by R.G. Strom and C.C. Allen.

(3) The incremental crater density estimates for 407 craters are those presented in Guinness and Arvidson's (1977) manuscript. They did not estimate either the relative or cumulative densities. It is based on data from two lunar orbiter frames: a medium resolution frame and a high resolution frame. The crater density estimates for 156 craters were made by using tables of raw data provided us by Ed Guinness and Ray Arvidson and only uses data from the medium resolution frame and therefore has a more limited diameter range. However, the estimated crater density and slope lie within the statistical error bars.

Values of estimated crater density at 1km for data set 2 are about a factor of 10 larger than the estimate based on the small crater population (data set 2). This suggests that many of the larger >1km craters in data set 2 are older than 3.3BY. A more detailed analysis of these age relationships is needed.

TABLE III. ESTIMATES OF AGE RELATIONSHIPS FROM CRATER DENSITIES

	4km diameter craters	32km diameter craters
	Relative Crater Densities log (R)	Relative Crater Densities log (R)
Radar Craters *	$-3.98 \pm .08$	$-3.40 \pm .16$
Visual Craters **	$-2.58 \pm .13$	$-2.40 \pm .17$
$\Delta \log (R)$	$1.40 \pm .15$	$1.00 \pm .23$
$\frac{R \text{ radar craters}}{R \text{ visual craters}}$	$0.040 \begin{matrix} + .016 \\ - .012 \end{matrix}$	$0.100 \begin{matrix} + .07 \\ - .04 \end{matrix}$
Age radar craters	$0.132 \begin{matrix} + .05 \\ - .04 \end{matrix} \text{ BY}$	$0.33 \begin{matrix} + .23 \\ - .13 \end{matrix} \text{ BY}$

NOTES TO TABLE III:

- (1) Data presented in this paper (see data set 1 of Table 2).
 (2) Data from the Planetary Basaltic Working Group (data set 2 of Table 2).

TABLE B-I

SMALL CRATERS WITH STRONG
INFRARED SIGNATURES

NAME	LONG.	LAT.	DIA.	RACK.	D _{3.8cm}	D _{IR}	ΔT_{obs}
"Tiny Tim"	-50.4	- 0.2	0.7	M	40	23	28
Near Suess	-47.9	3.9	0.9	M	33	16	46
Near Copernicus C	-14.8	8.2	1.1	M	24	19	21
Near Kies C	-26.0	-25.7	1.1	T	20	20	14
Near Goodacre P	17.3	-33.7	1.2	T	20	12	20
In Mare Vaporum	3.6	14.9	1.2	M	20	11	20
Between Dedale and Diophantus	-34.2	28.4	1.2	M	22	13	32
Floor of Mee	-33.6	-43.6	1.3	T	40	26	35
Near Fra Mauro B	-20.4	- 3.7	1.3	M	23	15	18
Near Wilhelm	-25.6	-42.7	1.3	T	20	16	18
Kerner D	3.2	-27.2	1.5	T	20	14	18
Lassel D	-10.5	-14.5	1.7	M	31	14	24
North of S. Gallus (2)	11.3	20.4	1.8	M	31	18	47
Near La Croix F	-60.3	-47.5	2.0	T	30	24	56
Linne (2)	11.7	27.7	2.1	M	40	13	28
Between Capella C and Capella CA	36.0	- 6.0	2.2	T	32	20	16
Near Atlas A	50.1	46.5	2.4	T	30	18	28
Near Grimaldi G	-64.6	- 8.0	2.4	T	45	30	20
Posidonius X	27.9	30.0	3.0	M	30	49	22
Near Fontenelle G	-18.6	60.4	3.0	M	31	29	36
Abulfeda O	12.3	-12.8	3.2	T	45	24	20
Herigonius K	-36.4	-12.8	3.2	M	30	17	32
Hesiodus E	-15.3	-27.8	3.3	M	29	15	24
Flamsteed HA	-52.1	- 5.6	3.4	M	36	32	33
Liebig FA	-45.0	-24.8	3.4	M	30	32	38
Encke X	-40.2	0.9	3.5	M	42	18	32
Censorinus	32.7	- 0.4	3.8	T	50	26	45
La Condamine S	-25.0	57.2	3.9	M	55	28	40
Regio Montanus CA	- 5.0	-29.1	4.4	T	80	21	46
Hell OA	- 4.4	-33.9	4.4	T	90	43	44
Piton B (1)	- 0.1	39.3	4.9	M	66	14	28
Floor of Maginus	- 3.7	49.3	5.1	T	75	25	30
Rim of Rocca A	-69.0	-13.8	6.0	T	38	39	24
Möltke	24.2	- 0.6	6.5	M	45	19	28
Rümker E	-56.9	38.5	6.7	M	64	27	32
Louville D	-51.9	46.8	6.7	M	45	23	30
Bush B	17.0	-37.9	6.8	T	52	16	45
Emmert A	65.4	24.1	7.1	T	90	37	40

(1) See Figure 1

(2) See Figure 2

FIGURE CAPTIONS

Figure 1: 3.8cm depolarized radar image, earth-based and Lunar Orbiter photographs of Piton B and its environs. Piton B (0.1°W , 39.3°N , 4.9km diam.) is denoted by the arrows. Circles in the photographs have diameters of 50km and 100km centered on Piton B. Other prominent craters are Cassini (4.5°E , 42.6°N , 56.5km diam.), Aristillus (1.2°E , 33.8°N , 55.3km diam.) and Autolycus (1.4°E , 30.6°N , 39.2km diam.). The 3.8cm radar image on the right has increments which vary as multiples of two. Thus, a single change in tone implies twice as much backscattered power.

Figure 2: 3.8cm depolarized and earth-based photographs of Montes Appeninus and Western Mare Serenitatis. Circles in the earth-based photographs denote sizes of the bright areas in the 3.8cm radar image. Craters with large 3.8cm radar haloes include Linne' (11.7°E , 27.7°N , 2.1km diam.), Hadley A (6.5°E , 25.0°N , 12.2km diam.), Aratus (4.5°E , 23.5°N , 10.6km diam.), and three unnamed craters in Western Mare Serenitatis with diameters between one and two kilometers.

Figure 3: Range of 3.8cm radar halo sizes included in the 120 crater catalog. The criterion of being greater than 20 kms for the smaller crater was selected so that 3.8cm radar bright areas were covered by at least one earth-based infrared resolution element and several 70cm radar resolution elements. The criterion that radar bright areas be twice the crater diameter for the larger craters was selected so that only a few larger craters were selected. Thus, this study emphasizes craters with diameters between one and ten kilometers.

Figure 4: Positions of the 120 craters with large 3.8cm radar haloes. Circle size corresponds to 3.8cm halo size. Background grid shows available LAC charts. No craters in the limb areas were examined.

Figure 5: Scatter diagrams of infrared and radar halo diameters versus crater diameter. Solid line indicates 3.8cm halo diameter selection criterion (see Figure 3). Dashed lines show halo diameter/crater diameter ratios of 1, 2, 4, 8 and 16, respectively. Measured infrared and 70cm halo diameters have been reduced by one resolution cell-size to account for resolution smearing (see Appendix A).

Figure 6: Scatter diagrams of infrared and radar strengths versus crater diameter. Radar strengths are ratios of peak crater signal to background and are quantized to nearest power of root 2. Infrared strengths are temperature differences in $^{\circ}\text{K}$ with respect to terra at the same angle of incidence. Solid lines show signal diminution if for signals which arise solely from the crater and are observed with resolutions of 22.0, 2.0 and 7.5km at infrared, 3.8cm and 70cm wavelengths (see Appendix A).

Figure 7: Sizes of bright albedo areas in full moon and Lunar Orbiter IV photographs plotted versus crater diameter. Plots use the same convention as the plots in Figure 5. Note that the full moon bright albedo areas for a few craters are no larger than the crater itself.

Figure 8: Diameter-frequency distributions for craters with 3.8cm radar bright haloes (ejecta deposits). The left plot compares the population of all 3.8cm bright halo craters with the subpopulation of radar bright haloes that are also IR bright. The right plot compares mare and terra populations. Plotted diameters are offset slightly to promote readability of these similar distributions.

Figure 9: Least square fit to crater distributions for Oceanus Procellarum (67 craters, $1.4 \times 10^6 \text{ km}^2$) and 3.8cm radar bright halo craters with diameters greater than 4.0 kilometers (59 craters, $12.0 \times 10^6 \text{ km}^2$). Results of least squares fit given in Tables II and III.

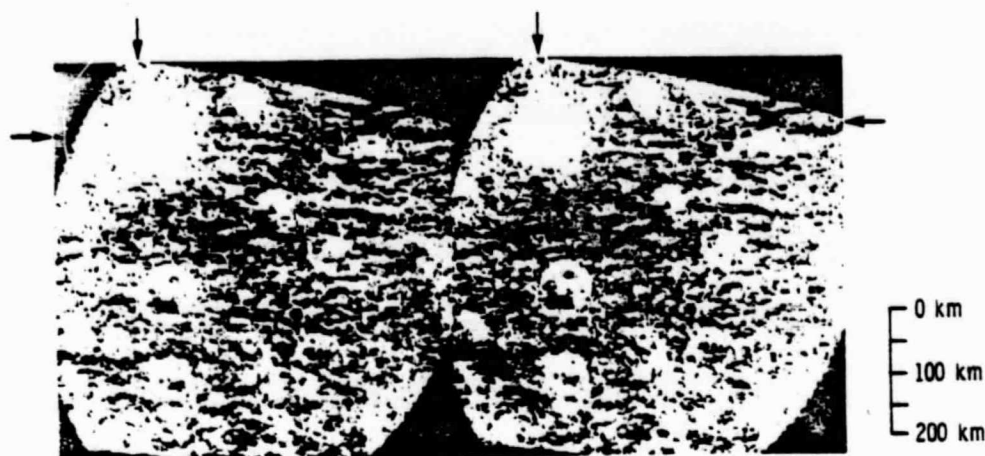
Figure A.1: Predicted temperatures for circular central areas with diameters between one and sixty-four kilometers and observed temperature enhancements of 10 to 50°K . If these central areas have maximum temperatures of 100°K , then central area sizes must be six to sixteen kilometers or greater. This indicates agreement between the infrared sizes and strengths plotted in Figures 5 and 6.

Figure A.2: Predicted 70cm enhancements for central areas between one and sixty-four kilometers, observed enhancements of 2, 4, and 8 and a resolution of 7.5 kilometers. Note that minimum central areas must be 1.7 to 4.0 kilometers or larger for an assumed maximum central area enhancement of 32. This is consistent with the 70cm radar sizes and strengths plotted in Figures 5 and 6.

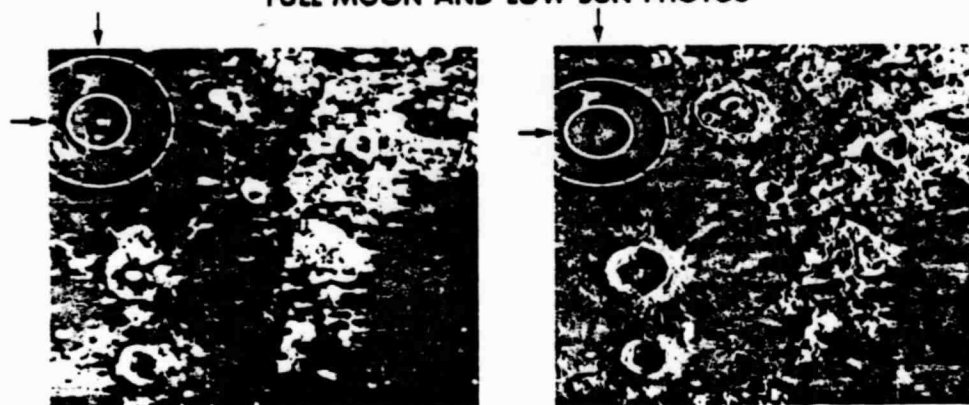
Figure B.1: A possible model of crater ejecta evolution assuming infrared and radar signals arise solely from surface and subsurface rocks. Only the youngest and intermediate age craters of this model are in the 120 crater catalog described in the main body of this paper. Evolution of the older age crater to still older forms is described by Thompson *et al.* (1980).

Figure B.2: Extent of the earth-based infrared and radar signals from Lichtenberg B, a 0.5 AE old crater described by Settle *et al.* (1979). This represents an intermediate in the evolution model shown in Figure B.1 since the 3.8cm radar echo extends well beyond the crater rim while the infrared and 70cm radar bright areas are confined to the crater interior and the close in ejecta deposits.

B-38
PITON B
3.8 cm RADAR MAP - ZAC 4.11 DEPOLARIZED



FULL MOON AND LOW SUN PHOTOS

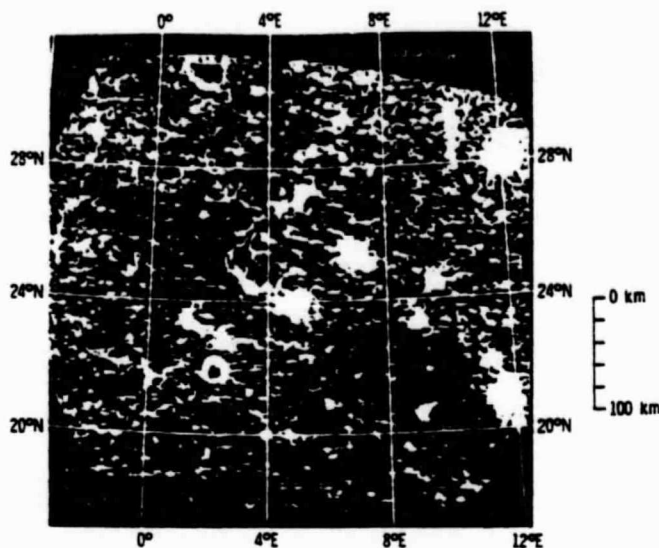


LUNAR ORBITER IV PHOTO



ORIGINAL PAGE IS
OF POOR QUALITY

Figure 1: 3.8cm depolarized radar image, earth-based and Lunar Orbiter photographs of Piton B and its environs. Piton B (0.1°W , 39.3°N , 4.9km diam.) is denoted by the arrows. Circles in the photographs have diameters of 50km and 100km centered on Piton B. Other prominent craters are Cassini (4.5°E , 42.6°N , 56.5km diam.), Aristillus (1.2°E , 33.8°N , 55.3km diam.) and Autolycus (1.4°E , 30.6°N , 39.2km diam.). The 3.8cm radar image on the right has increments which vary as multiples of two. Thus, a single change in tone implies twice as much backscattered power.



3.8 cm RADAR MAP - ZAC 3.01 DEPOLARIZED

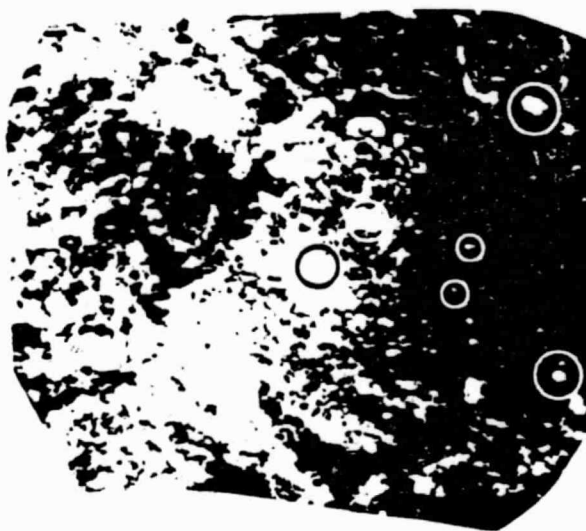
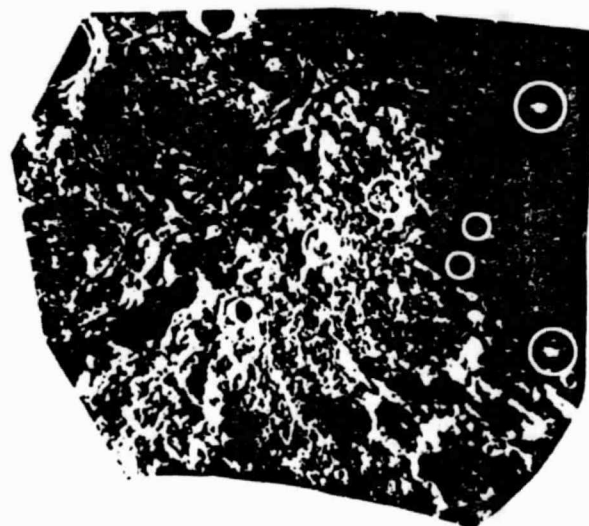
FULL MOON PHOTOGRAPH
PLATE C-III CON. LUNAR ATLASLOW SUN PHOTOGRAPH
PLATE C-9 CON. LUNAR ATLAS

Figure 2: 3.8cm depolarized and earth-based photographs of Montes Appeninus and Western Mare Serenitatis. Circles in the earth-based photographs denote sizes of the bright areas in the 3.8cm radar image. Craters with large 3.8cm radar haloes include Linne' (11.7°E, 27.7°N, 2.1km diam.), Hadley A (6.5°E, 25.0°N, 12.2km diam.), Aratus (4.5°E, 23.5°N, 10.6km diam.), and three unnamed craters in Western Mare Serenitatis with diameters between one and two kilometers.

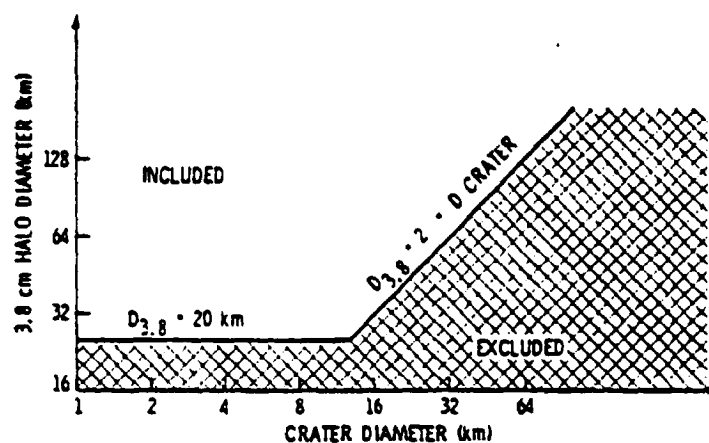


Figure 3: Range of 3.8cm radar halo sizes included in the 120 crater catalog. The criterion of being greater than 20 kms for the smaller crater was selected so that 3.8cm radar bright areas were covered by at least one earth-based infrared resolution element and several 70cm radar resolution elements. The criterion that radar bright areas be twice the crater diameter for the larger craters was selected so that only a few larger craters were selected. Thus, this study emphasizes craters with diameters between one and ten kilometers.

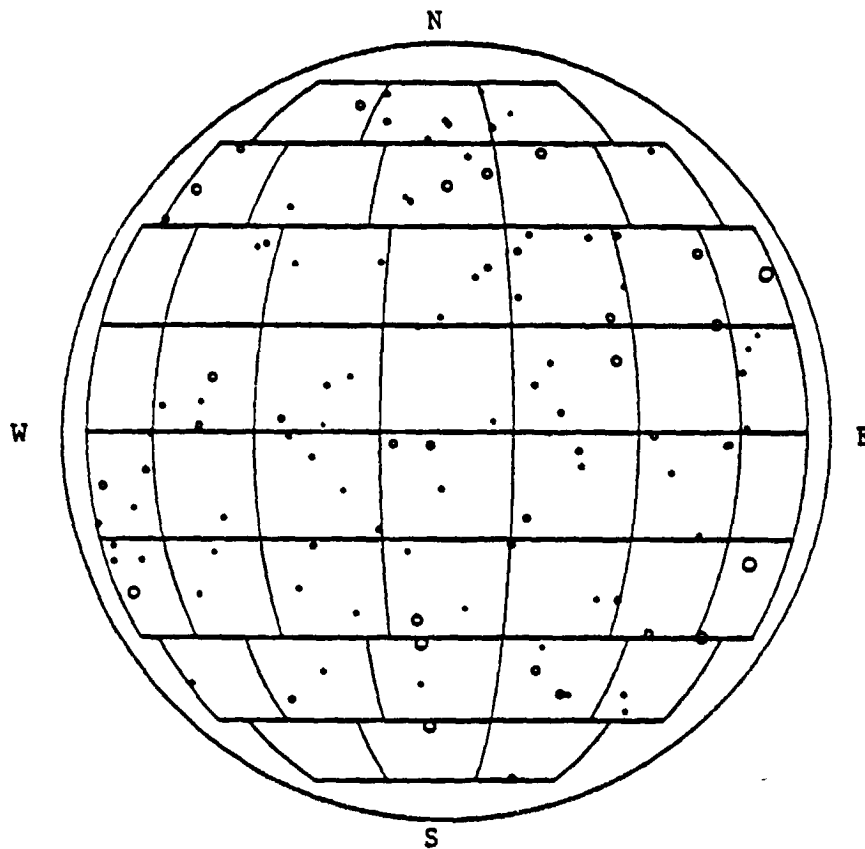


Figure 4: Positions of the 120 craters with large 3.8cm radar haloes. Circle size corresponds to 3.8cm halo size. Background grid shows available LAC charts. No craters in the limb areas were examined.

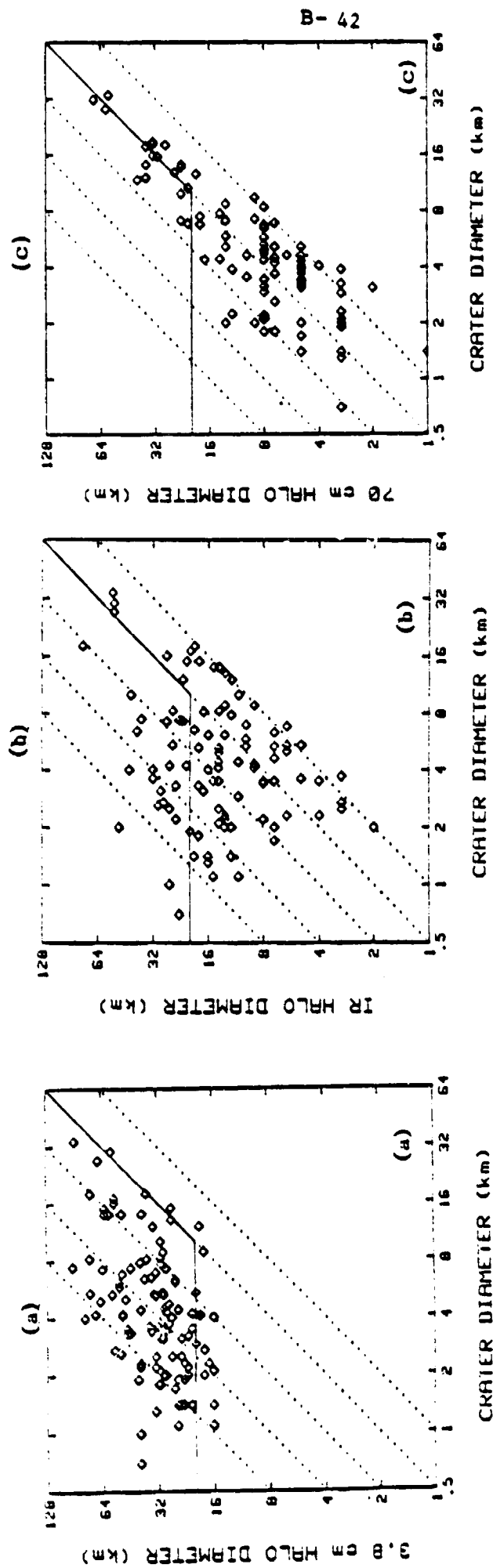


Figure 5: Scatter diagrams of infrared and radar halo diameters versus crater diameter. Solid line indicates 3.8cm halo diameter selection criterion (see Figure 3). Dashed lines show halo diameter/crater diameter ratios of 1, 2, 4, 8 and 16, respectively. Measured infrared and 70cm halo diameters have been reduced by one resolution cell-size to account for resolution smearing (see Appendix A).

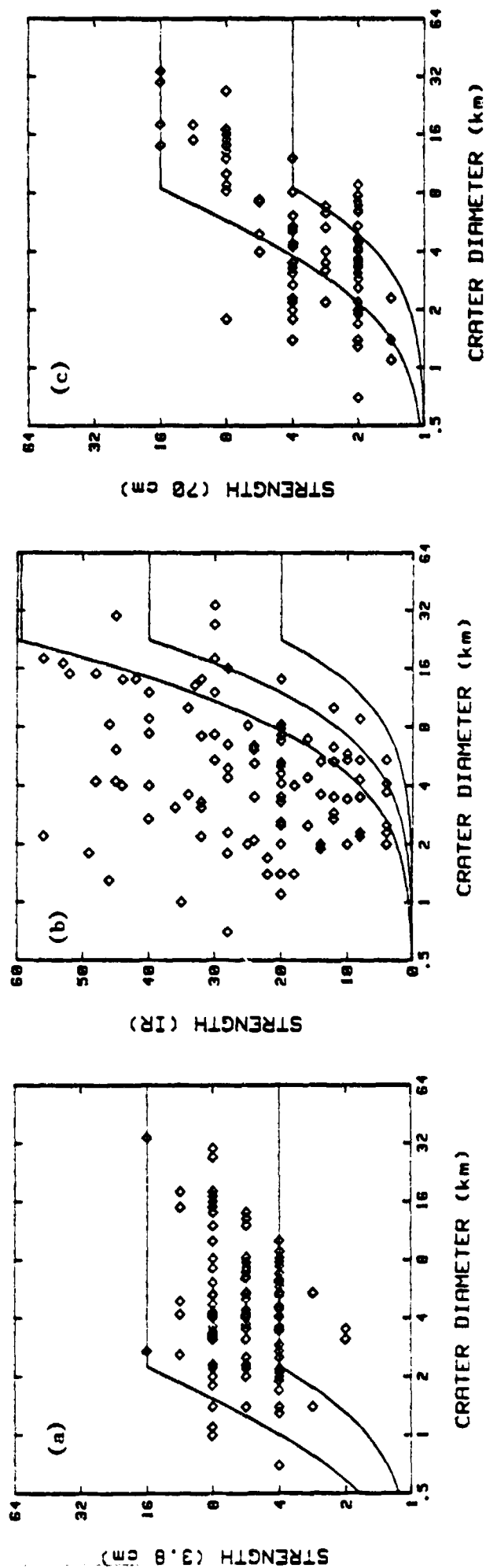


Figure 6: Scatter diagrams of infrared and radar strengths versus crater diameter. Radar strengths are ratios of peak crater signal to background and are quantized to nearest power of root 2. Infrared strengths are temperature differences in $^{\circ}\text{K}$ with respect to terra at the same angle of incidence. Solid lines show signal diminution if for signals which arise solely from the crater and are observed with resolutions of 22.0, 2.0 and 7.5 km at infrared, 3.8cm and 70cm wavelengths (see Appendix A).

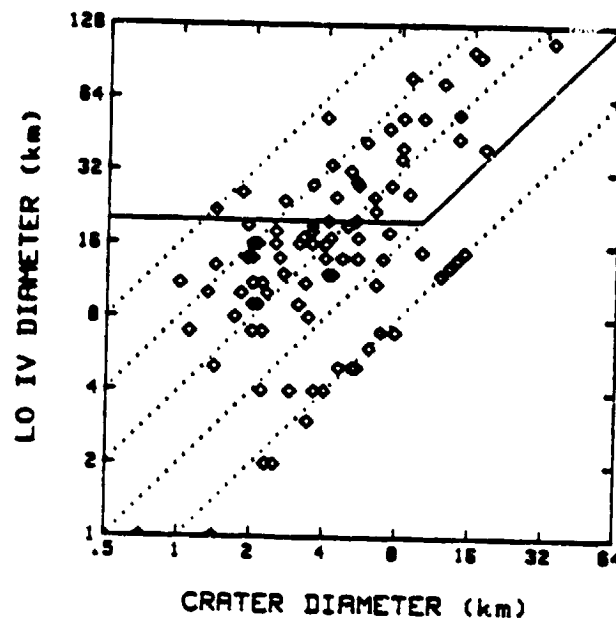
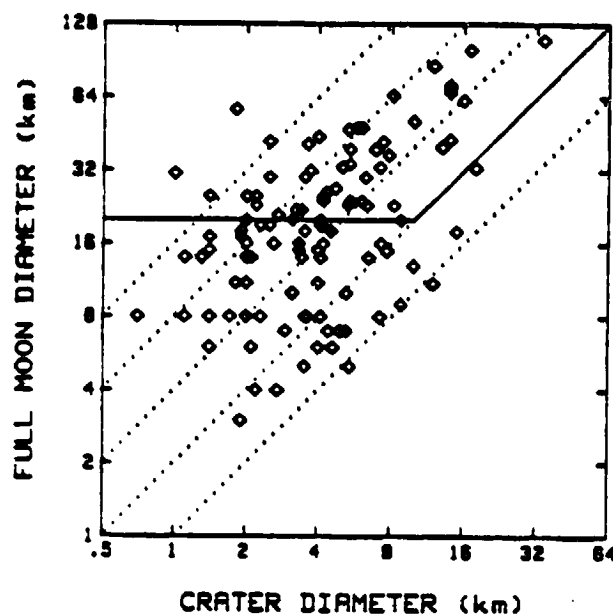
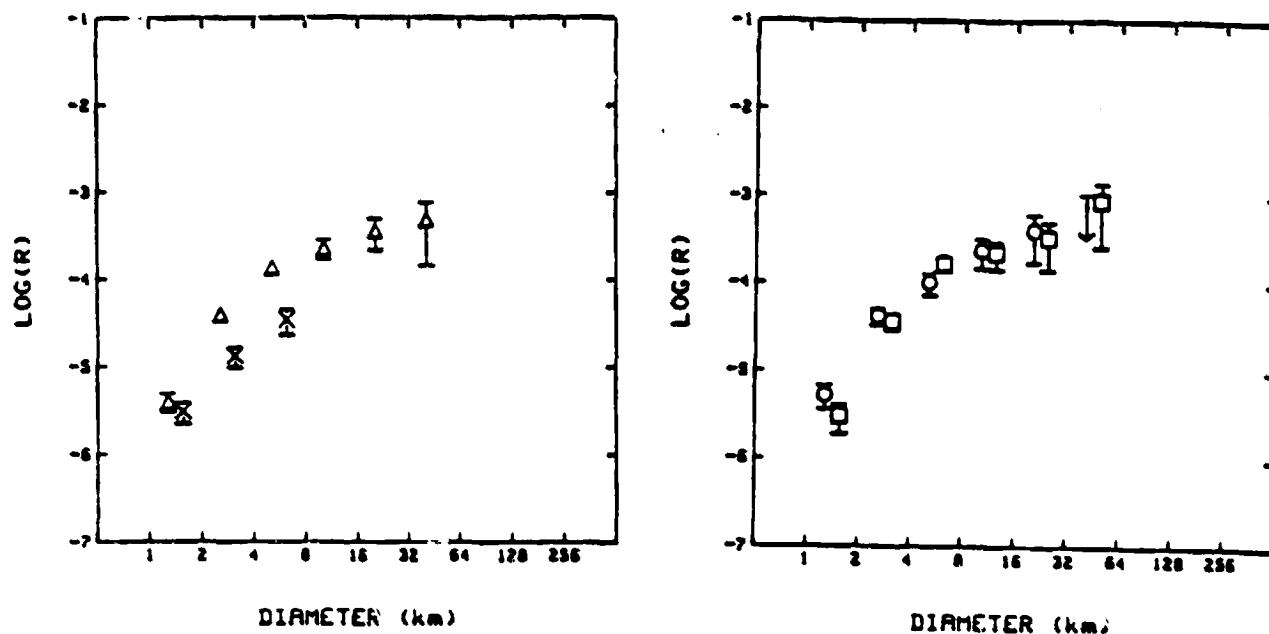


Figure 7: Sizes of bright albedo areas in full moon and Lunar Orbiter IV photographs plotted versus crater diameter. Plots use the same convention as the plots in Figure 5. Note that the full moon bright albedo areas for a few craters are no larger than the crater itself.



- \triangle All 3.8cm radar bright halo craters
- \times IR bright halo craters (from Appendix B, Table B-II)
- \circ Mare 3.8cm radar bright halo craters
- \square Terra 3.8cm radar bright halo craters

Figure 8: Diameter-frequency distributions for craters with 3.8cm radar bright haloes (ejecta deposits). The left plot compares the population of all 3.8cm bright halo craters with the subpopulation of radar bright haloes that are also IR bright. The right plot compares mare and terra populations. Plotted diameters are offset slightly to promote readability of these similar distributions.

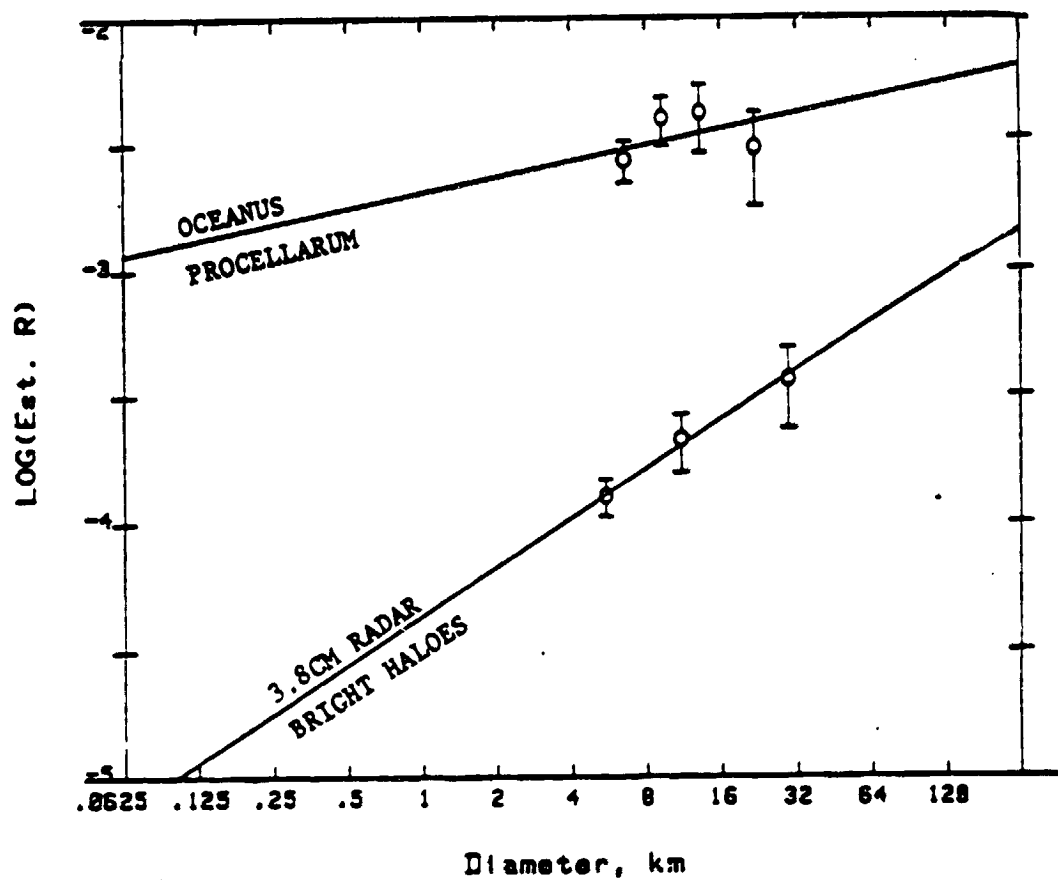


Figure 9: Least square fit to crater distributions for Oceanus Procellarum (67 craters, $1.4 \times 10^6 \text{ km}^2$) and 3.8cm radar bright halo craters with diameters greater than 4.0 kilometers (59 craters, $12.0 \times 10^6 \text{ km}^2$). Results of least squares fit given in Tables II and III.

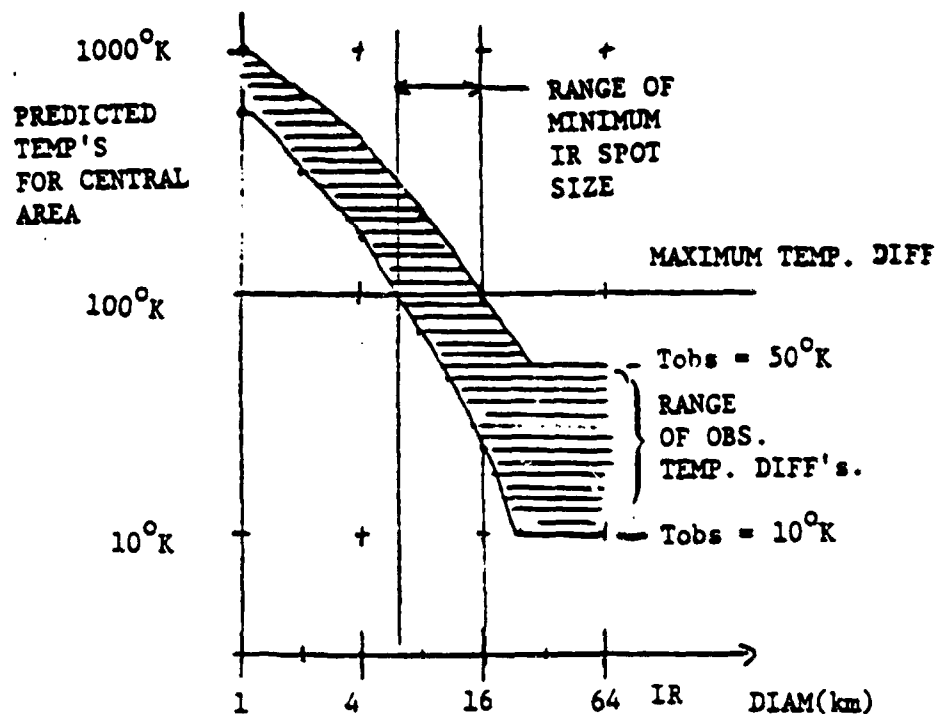


Figure A.1. Predicted temperatures for circular central areas with diameters between one and sixty-four kilometers and observed temperature enhancements of 10 to 50°K . If these central areas have maximum temperatures of 100°K , then central area sizes must be six to sixteen kilometers or greater. This indicates agreement between the infrared sizes and strengths plotted in Figures 5 and 6.

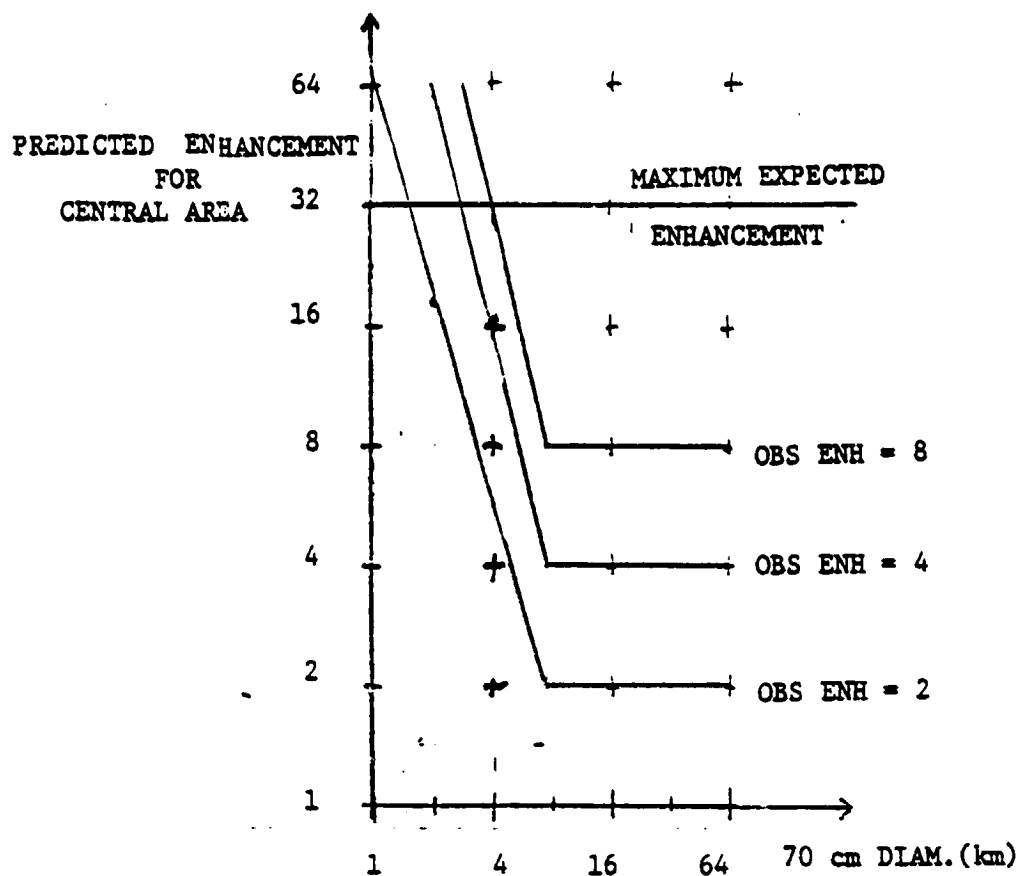


Figure A.2. Predicted 70cm enhancements for central areas between one and sixty-four kilometers, observed enhancements of 2, 4, and 8 and a resolution of 7.5 kilometers. Note that minimum central areas must be 1.7 to 4.0 kilometers or larger for an assumed maximum central area enhancement of 32. This is consistent with the 70cm radar sizes and strengths plotted in Figures 5 and 6.

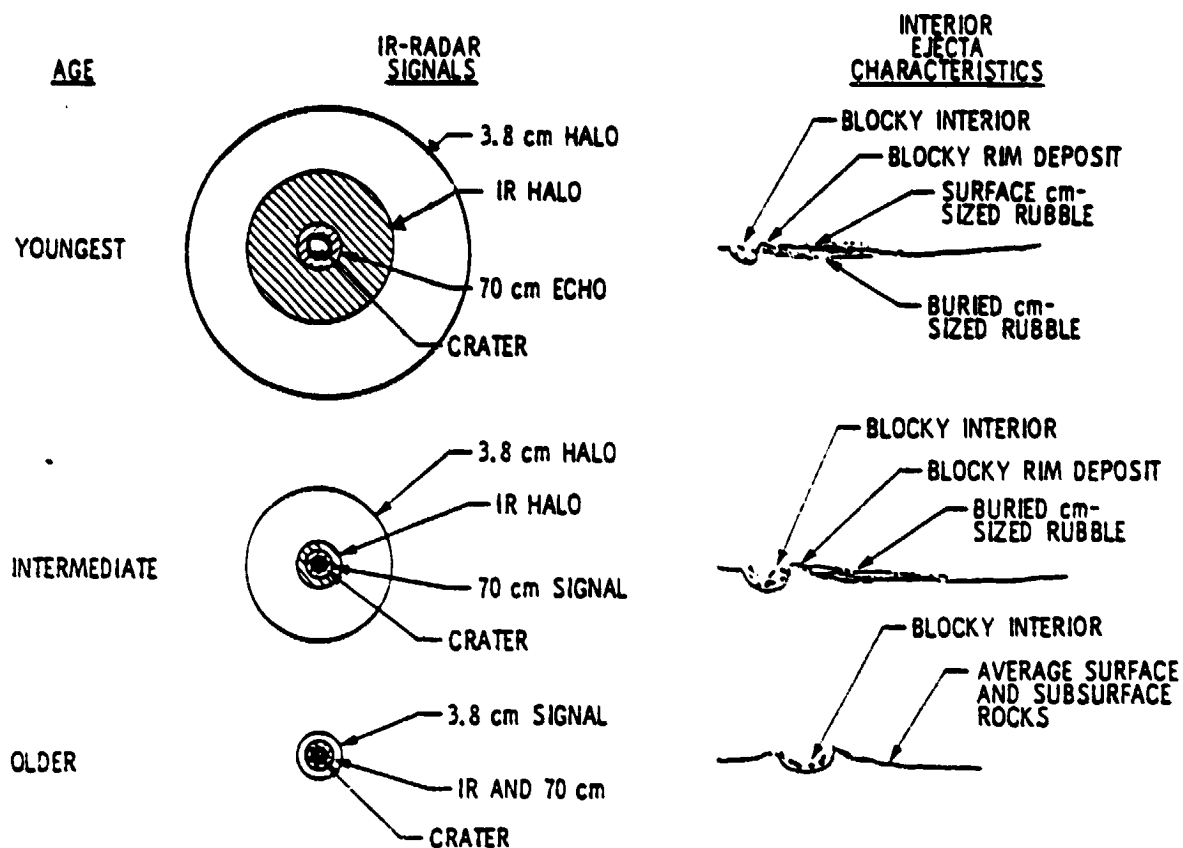


Figure B-1: A possible model of crater ejecta evolution assuming infrared and radar signals arise solely from surface and subsurface rocks. Only the youngest and intermediate age craters of this model are in the 120 crater catalog described in the main body of this paper. Evolution of the older age crater to still older forms is described by Thompson et al. (1980).

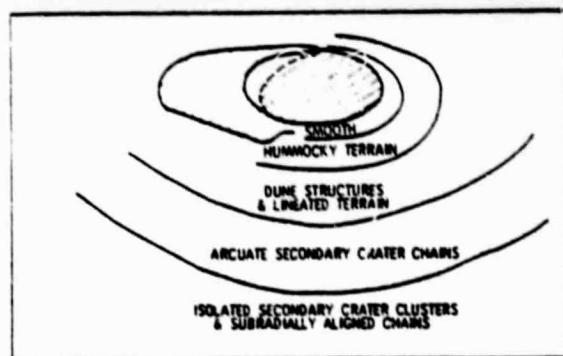
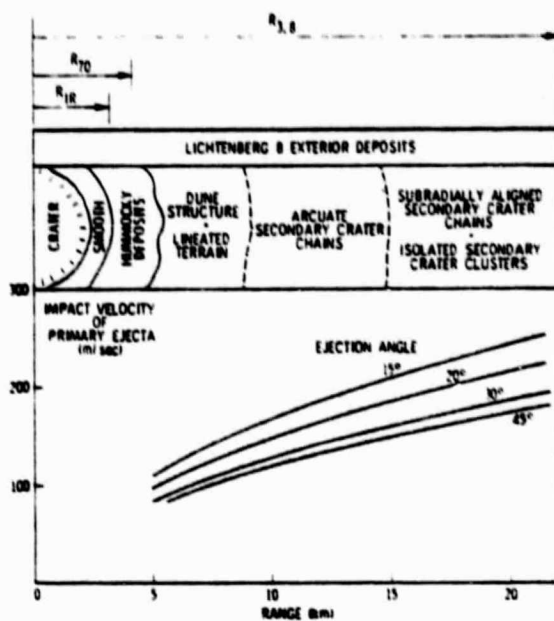


Figure B-2: Extent of the earth-based infrared and radar signals from Lichtenberg B, a 0.5 AE old crater described by Settle, *et al.* (1979). This represents an intermediate in the evolution model shown in Figure B-1 since the 3.8cm radar echo extends well beyond the crater rim while the infrared and 70cm radar bright areas are confined to the crater interior and the close in ejecta deposits.

APPENDIX C

Papike, J.J. and Merrill, R.B., eds.
Proc. Conf. Lunar Highlands Crust (1980), p. 483-499
 Printed in the United States of America

Infrared and radar signatures of lunar craters: Implications about crater evolution*

T. W. Thompson¹, J. A. Cutts¹, R. W. Shorthill², and S. H. Zisk³

¹ Planetary Science Institute, Science Applications, Incorporated, Pasadena, California 91101

² University of Utah Research Institute, Salt Lake City, Utah 84108

³ NEROC Haystack Observatory, Westford, Massachusetts 01886

Abstract—Lunar craters from different geological epochs have distinctive signatures in ground-based infrared eclipse imaging and radar imaging at 3.8 and 70 cm wavelengths. Craters have been classified as B (bright) or F (faint) depending on the contrast between the signal level from the crater floor and the average terrain background.

For large (diam. ≥ 10 km) terra craters, the IR/radar signatures are a function of crater age, supporting the hypothesis that lunar surface processes gradually reduce bright signatures to average terra background. The youngest craters have infrared temperatures and radar echo strengths which are enhanced relative to their backgrounds. In somewhat older craters, the infrared temperature enhancements have faded, but the high radar echo strengths remain. In still older craters, either the 3.8 cm enhancement or the 70 cm enhancement have disappeared. Finally, the oldest craters have no enhancements at any wavelength.

The evolution of IR/radar signatures depends upon crater size. Comparisons of size-frequency distributions of different crater types show that craters with both radar and infrared enhancements are only half as abundant as Copernican and Eratosthenian craters at 10 km diameter but are twice as abundant at 100 km diameter. Craters with any form of infrared or radar enhancement are only two thirds as abundant as Imbrian and younger craters at 10 km diameter, but are 50% more abundant at 100 km diameter. Thus, some larger radar enhanced craters are pre-Imbrian. The path of evolution is also size dependent: in larger craters (diam. ≥ 30 km) the 3.8 cm enhancement disappears first; in smaller craters, the 70 cm enhancement disappears first.

Some geological models for evolution of IR/radar signatures of crater floors have been examined. The simplest model involves the formation and subsequent gardening of an impact melt layer in the crater floor. This model accounts for the evolutionary path of larger craters (≥ 30 km) but not smaller craters. Quantitative models of the evolution of rock populations in regoliths and of the interaction of microwaves with regoliths are needed to better understand crater evolutionary processes.

I. INTRODUCTION

The infrared and radar signatures of lunar craters contain information about surface and subsurface rock populations. Infrared (10 micron) eclipse temperatures are controlled by surface rocks, whereas radar echo strengths are controlled by both surface and subsurface rocks (Thompson *et al.*, 1974). The infrared and

* PSI Contribution 124

radar signatures of craters change with time as the pristine crater is modified by surface processes. Thompson *et al.* (1974) reviewed the various combinations of infrared and radar signatures for 51 selected craters. They showed that the youngest craters have enhanced infrared and radar signatures and that enhanced radar echoes at the longest radar wavelength are the last enhanced signature to disappear. The objective of this work is to study intermediate states in the evolution of infrared and radar signatures of craters.

Whereas the earlier work of Thompson *et al.* (1974) was based upon only 51 craters, these hypotheses about lunar crater evolution can now be tested with a much larger data set of Thompson *et al.* (1979). In particular, craters with enhanced infrared and radar signatures were cataloged for the portion of the earth-side lunar hemisphere covered by the LAC (Lunar Aeronautical Chart) maps. A previous study of this data set showed mare-terra differences for smaller lunar craters (diam. < 12 km) associated with depth of the megaregolith, the debris layer overlying the lunar terrae (Thompson *et al.*, 1979). In this study, larger (diam. > 12 km) craters on the terra were compared with crater age statistics of Wilhelms *et al.* (1978) to test a hypothesis of crater evolution originally proposed by Thompson *et al.* (1974). Mare-terra differences in infrared and radar crater signatures were also investigated to corroborate the findings from the comparison of terra craters and their photogeological ages.

II. CATALOG OF RADAR AND INFRARED SIGNATURES OF LUNAR CRATERS

A catalog of infrared and radar crater signatures was assembled by Thompson *et al.* (1979) using data from several sources. The infrared data was originally obtained during the lunar eclipse of December 19, 1964, using the Kottamia 74-inch telescope of the Helwan Observatory, Egypt (Shorthill, 1973). The 3.8 cm radar data were obtained in a series of observations from 1966 to 1970 using the planetary radar at Haystack Observatory (Zisk *et al.*, 1974). The 70 cm radar data were obtained between 1966 and 1969 using the 430 MHz radar at the Arecibo Observatory, Puerto Rico (Thompson, 1974). Surface resolution for these observations was 1-3 km for the 3.8 cm radar, 5-10 km for the 70 cm radar, and 14-30 km for the infrared observations. This resolution, which is the image size of a point target, is approximately one-half of the line-pair resolution.

This catalog covers about one-half of the earth-visible surface. Craters on the limb beyond the area of the available LAC charts were ignored. There are no 70 cm radar data for these areas and the infrared resolution is reduced. Also, as described by Thompson *et al.* (1979), the original data were sorted by distance from the subearth point into the Central, Middle, and Outer Ring areas shown in Fig. 1. Only the data for the Middle and Outer Rings have been used in our investigations because of the poor radar data in the Central Area.

This catalog contains 386 craters with diameters greater than 12 km. Crater names, positions, and diameters were taken from the Lunar and Planetary Laboratory (LPL) catalogs of Arthur *et al.* (1963, 1964, 1965, and 1966). Craters were classified as mare craters or terra craters based upon their settings in the USGS Lunar Geological Maps. Craters in both the irregular and circular (basin) mare were classified as mare craters; all other craters were classified as terra craters.

Radar and infrared signatures for these craters were measured from quantized video displays of the data. For larger craters with diameters several times the resolution cell size, the infrared and radar strengths were measured from the interior of the crater. These larger craters generally display uniform responses across their interiors. The radar data show topographic effects associated with the

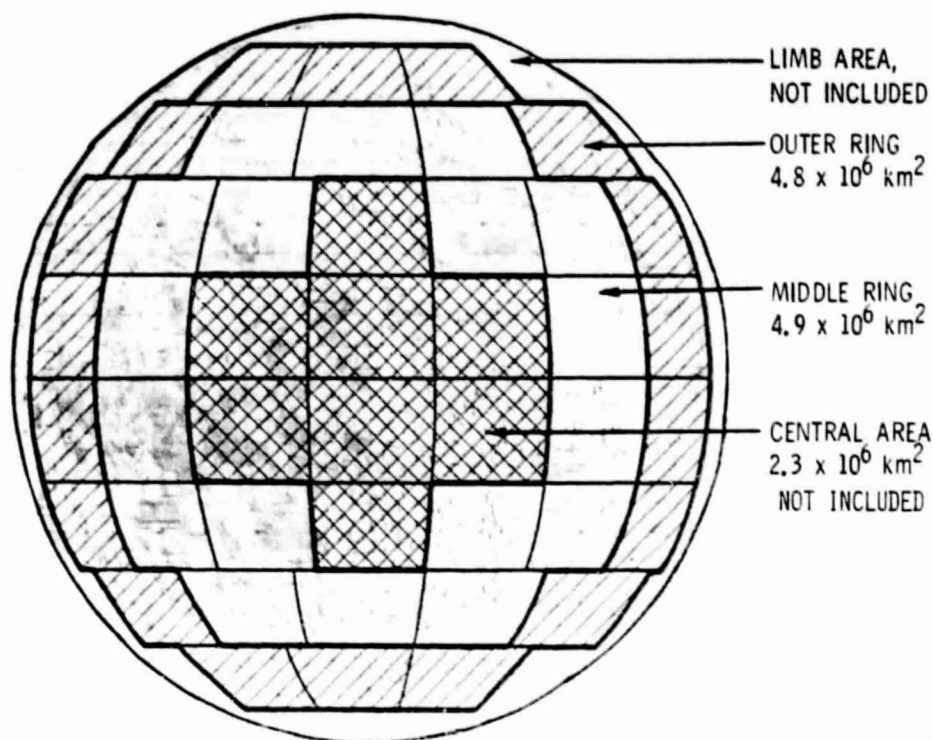


Fig. 1. Area for infrared radar statistics of this study. Middle and Outer Ring Areas were combined; Central and Limb Areas were ignored (see Thompson *et al.*, 1979).

rims since areas tilted toward the radar have stronger echoes and areas tilted away from the radar have weaker echoes. For smaller craters with diameters of a few resolution cell sizes and less, the infrared and radar strengths were measured for the center of spots which appear in the image. The infrared and radar strengths were measured relative to the brightness of the surrounding terrain.

To simplify the statistical analysis of the radar and infrared signatures, signal strengths were classified as bright or faint. Radar bright craters backscattered at least twice the power of the mean surface; infrared bright craters were warmer than the mean surface by 10°K or more. Faint craters did not meet these criteria and consequently had low contrasts relative to the adjoining terrains. A binary code, XYZ, was used to describe the infrared and radar signature of each crater in the catalog. Code X takes the value B when the crater is infrared bright and F when it is faint. Codes Y and Z were similarly assigned based on the 3.8 cm and 70 cm radar signals. (For example, a FBF crater has bright 3.8 cm radar echo with faint infrared and 70 cm radar strengths.) There are eight possible combinations. One crater type, the FFF crater, has not yet been cataloged for the terra since it was not pertinent to the earlier study (Thompson *et al.*, 1979). However, a comparison of the statistics for the infrared and radar bright craters with the data on Wilhelms *et al.* (1978) indicates that FFF craters on the terra should be ten times more abundant than all infrared and radar bright craters. Thus, about 2900 FFF craters should occur in our study area.

Histograms for the various classes of craters with enhanced infrared and radar signatures are given in Fig. 2. The surface conditions for these various combinations of infrared and radar signatures are those given in Table 1. We now consider what these crater populations imply about the origin of these craters and the evolution of craters from one class to another in response to various lunar surface properties.

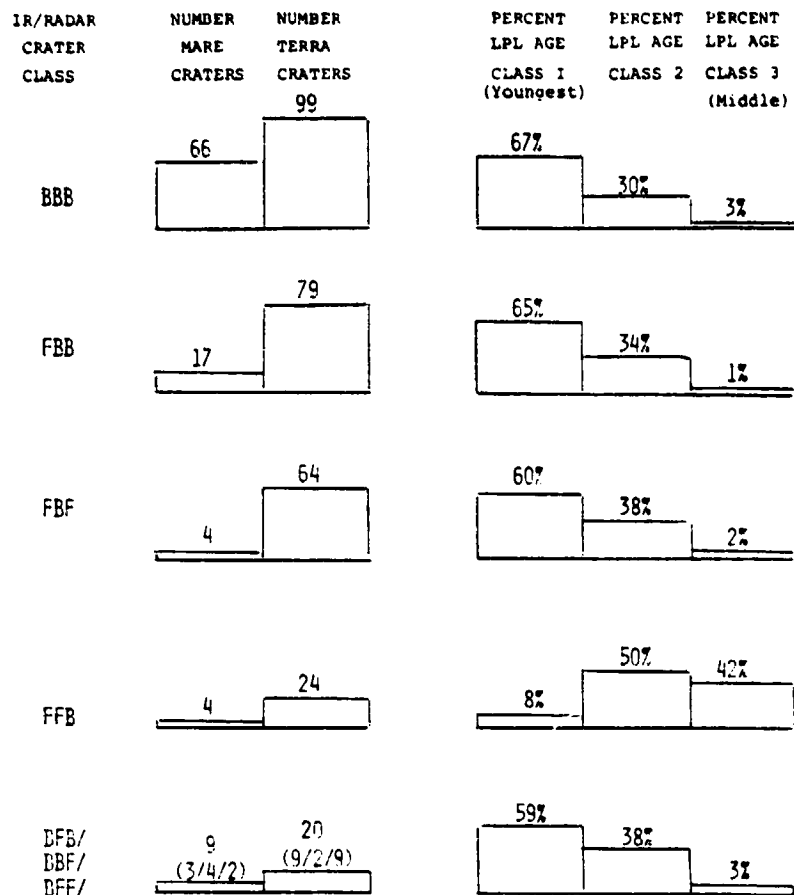


Fig. 2. Histograms for the occurrence of infrared and radar craters with diameters greater than 12 km in the Central and Outer Ring areas of Fig. 1. The FBB and FFB craters occur almost exclusively in the terra; the BFB, BBF, BFF craters occur rarely. The number of FFF craters is estimated to be 2,900 for the terra and zero for mare. Mare area was 4.4×10^6 km²; terra area was 5.4×10^6 km².

III. STATISTICS AND AGES OF RADAR-INFRARED CRATER CLASSES

The eight crater classes defined by various combinations of the infrared and radar signatures have varied populations. Most craters in the maria are either BBB or FBB craters, while in the terra the BBB, FBB, FBF, FFB, and FFF craters are abundant. To understand this, it is useful to correlate the radar infrared crater classes with age signatures based on photogeologic analysis. Figure 2 shows histograms of the occurrence of the various anomaly types as a function of a

photogeological degradation state from the LPL catalogs. These data are consistent with the hypothesis that BBB craters and FFF craters are end members of an evolutionary sequence.

Possible evolutionary paths

A framework of possible evolutionary paths for the radar-infrared crater signatures is shown in Fig. 3. This framework makes few assumptions about the mechanisms of evolution; it only requires that craters form first as BBB craters and progressively degrade to FFF craters through several possible intermediate states as the regolith at the location of the crater evolves back towards the local average for that part of the moon.

We can gain a crude idea of what evolutionary paths are most important from the frequency of occurrence of the different anomaly types on the moon (Fig. 4).

Table 1. Surface conditions implied by various combinations of infrared and radar signatures.

Anomaly index (IR-3.8 cm-70 cm)	Implied surface conditions
B—	Excess surface rocks with sizes larger than 10 cm.
-B-	Excess rocks with sizes of 1 to 40 cm on the surface or buried no deeper than 1.2 meters.
—B	Excess rocks with sizes of 20 cm to 7.0 m on the surface or buried no deeper than 20 meters.
BBB	Excess surface rocks with sizes of 1 cm and larger.
FBB	Average surface rocks Excess buried rocks with sizes of 1 to 40 centimeters within 1.1 m of surface. Excess buried rocks with sizes of 20 cm to 7.0 meters within 20 m of surface.
FBF	Average surface rocks Excess buried rocks with sizes 1 to 40 cm within 1.1 m of surface.
FFB	Average surface rocks Excess buried rocks with sizes of 20 cm to 7.0 m within 20 m of surface.
BBF	Excess surface rocks with sizes 1 cm to 20 cm. Average surface rocks with sizes 20 cm to 7.0 m.
BFB	Average surface rocks with sizes 1 cm to 40 cm. Excess surface rocks with sizes 40 cm to 7.0 m.
BFF	Average surface rocks with sizes 1 cm to 7.0 m. Excess surface rocks with sizes 7.0 m and larger.
FFF	Average surface, no excess surface and subsurface rocks.

Taken from Table 1 of Thompson, *et al.* (1979)

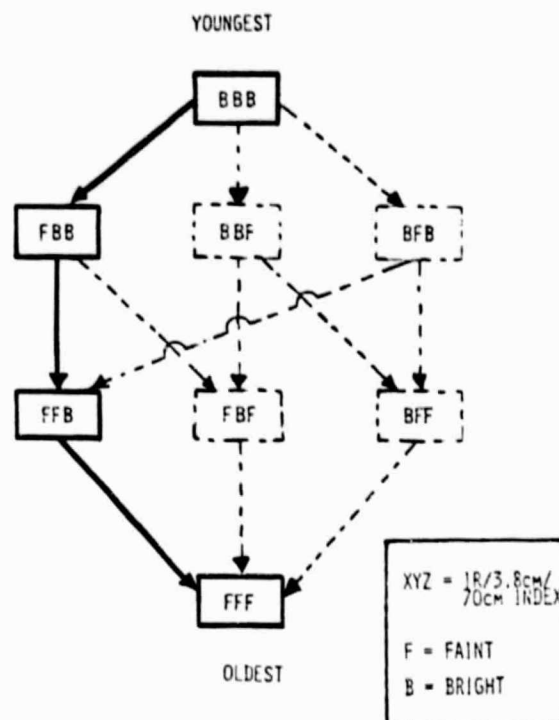


Fig. 3. Model for evolution of infrared and radar craters. This assumes that the youngest craters are BBB, the oldest are FFF and the intermediate cases lose one signature at a time. An expected evolution shown with the solid line assumes that the infrared signature disappears first, the 3.8 cm radar signature disappears second, and 70 cm radar signature disappears last.

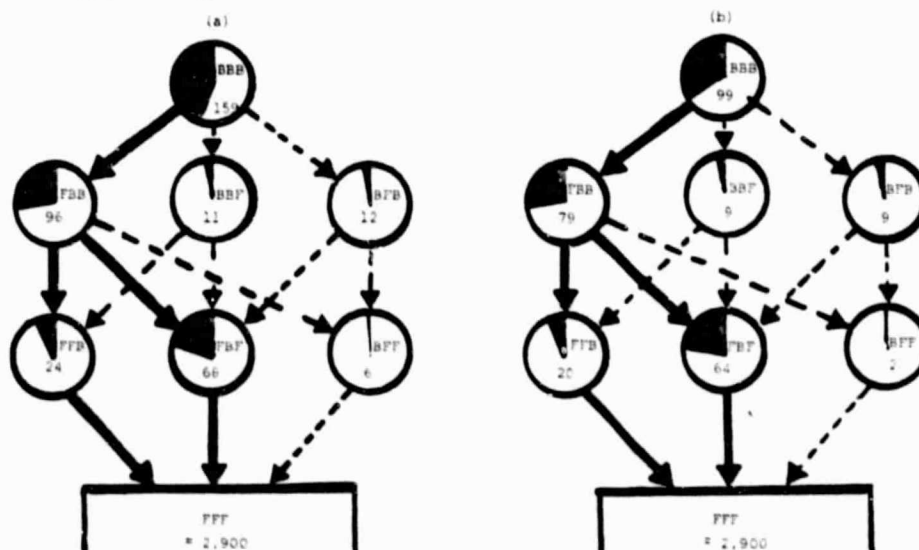


Fig. 4. Observed infrared radar crater populations plotted on evolution model paths shown in Fig. 3. (a) All mare and terra craters; (b) Terra craters only. Note that the FBB Craters evolve to both FBF and FFB craters.

There are 99 BBB, 79 FBB, 64 FBF, 30 FFB, 9 BFB, 9 BFF, and 2 BBF craters in the 5.4×10^6 km² of terra in the Central and Outer Ring areas of Fig. 1. Figures 2 and 4 show that the BBB, FBB, FBF and FFB craters occur frequently while the BBF, BFB, and BFF occur infrequently. These crater abundances suggest that BBB craters initially evolve into FBB craters; these FBB craters further evolve by two distinct paths to FBF or FFB craters; these FBF and FFB craters in turn finally evolve to FFF craters.

Time scale

In order to establish a time scale for the evolutionary paths illustrated in Figs. 3 and 4, and to estimate how long a crater remains in a particular class, we need to relate the populations of radar-infrared classes to a geologic time scale. Wilhelms *et al.* (1978) have recently classified large lunar craters by geologic age and constructed size-frequency distributions for craters produced in four time intervals: Copernican plus Erathosthenian, Imbrian, Nectarian and pre-Nectarian. By comparing these size-frequency distributions with those for radar-infrared bright crater classes we can search for a correspondence between crater class and age. Here we emphasize the craters on the terra since the radar-infrared populations indicate that craters from all stages in the evolution from BBB to FFF are preserved there (Fig. 4). Also, the terra background signal level in the radar and infrared has little variation across the moon and this simplifies the interpretation of the radar-infrared crater evolution.

In order to compare different crater populations we use relative size-frequency plots (Crater Analysis Group, 1979), where a function R is plotted versus crater diameter. The quantity R is $(\bar{D})^2 N / A (D_{\max} - D_{\min})$, where \bar{D} is the geometric mean of crater diameters, N is the number of craters, A is the area, and D_{\max} , D_{\min} are the maximum and minimum crater diameters in a size bin. A crater population which has a cumulative distribution proportional to (crater diameter)⁻² and a differential distribution proportional to (crater diameter)⁻³ plots as a horizontal line in a log (R) versus log (D) plot. Similarly, a crater population which has a cumulative distribution proportional to (crater diameter)⁻³ and a differential population proportional to (crater diameter)⁻⁴ has a slope of -1 in a log (R) versus log (D) plot.

In Fig. 5(a) we compare the diameter-frequency distribution of BBB craters on the terra with the Copernican and Eratosthenian craters. The two populations are generally similar at smaller diameters, suggesting that most small BBB craters are Copernican and Eratosthenian in age. However, BBB craters at larger diameter are more abundant than Copernican and Eratosthenian craters, implying that some of these larger BBB craters on the terra are Imbrian in age. In Fig. 5(b) we compare the size-frequency distributions of all infrared and radar bright craters on the terra with Imbrian and younger craters. The two populations have different slopes, indicating that the radar-infrared bright craters are again more numerous at larger sizes. Thus, some of the larger radar bright craters are pre-Imbrian.

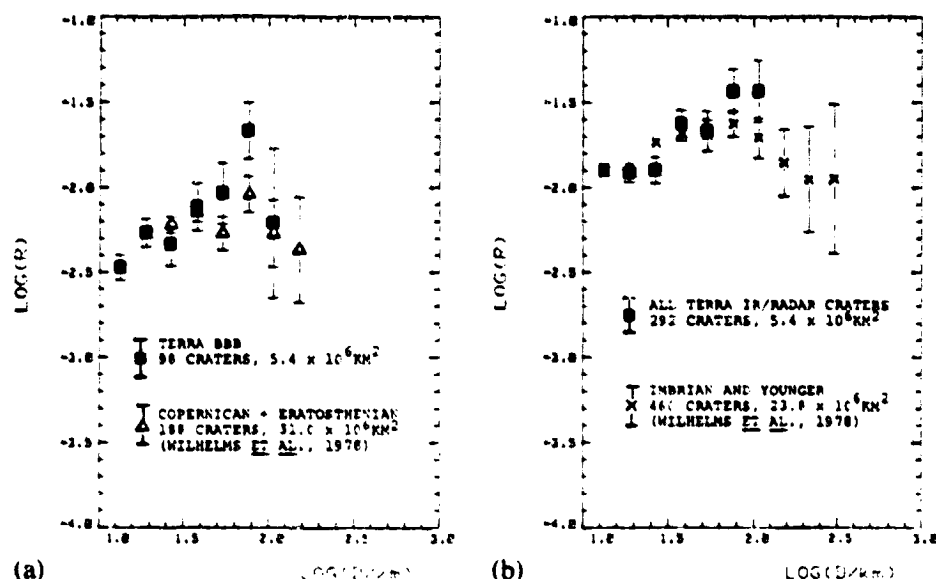


Fig. 8a. Relative size-frequency distributions for terra BBB and (Copernican & Eratosthenian) craters of Wilhelms *et al.* (1978).

Fig. 8b. Relative size-frequency distributions for all terra infrared/radar craters and Imbrian and younger craters of Wilhelms *et al.* (1978).

A more detailed insight into the age distributions of our radar-infrared bright craters as a function of the more populous crater classes is found in Figs. 6 and 7. The diameter-frequency distributions on the terra of BBB, FBB and FFB craters have positive slopes in this size range. The FBB crater distribution, in contrast, has a negative slope indicating that smaller craters dominate this population.

To investigate the slopes of these crater distributions, we assumed that the crater populations could be approximated by a linear relationship on a $\log(R)$ - $\log(D)$ plot. We used least squares methods to estimate crater densities at 10 km and 100 km diameters (Table 2). Crater data of Wilhelms *et al.* (1978) were similarly fitted to characterize cratering in the Nectarian and later ages. A chi-squared estimate of goodness-of-fit to the assumed straight line distributions was also computed. All fits were good except for the Nectarian and younger distribution which shows a marked deviation from the straight line relationship. This behavior was also noted by Wilhelms *et al.* (1978), who concluded that the impacting population in the Nectarian times was deficient in smaller bodies. Finally, in order to conveniently compare the various crater populations, the crater densities at 10 km and 100 km diameter were expressed as percentages of the Imbrian and younger values.

The data shown in Table 2 suggest that smaller craters evolve faster than larger craters. Note that terra BBB and FBB craters at 10 km diameter occur as fre-

quently as Copernican and Eratosthenian craters. In contrast, terra BBB craters at 100 km are twice as abundant as the Copernican and Eratosthenian craters and must therefore comprise a number of Imbrian craters also. All infrared and radar craters at 10 km diameters comprise 65 percent of post-Imbrian craters; this implies that one-third of these smaller post-Imbrian craters have evolved to FFF craters. In contrast, all infrared and radar craters at 100 km diameter are 1.4 times as abundant as the Imbrian and younger craters; this implies that some larger radar bright craters are pre-Imbrian.

The data shown in Table 2 suggest that smaller craters and larger craters evolve to different classes. There are few FFB craters at 10 km diameter and few FFB craters at 100 km. This implies that smaller FBB craters on the terra evolve to FBF craters, while larger FBB craters evolve to FFB craters.

The general features of the data shown in Table 2 are corroborated by comparing the statistics of the terra and mare craters shown in Fig. 6. The preservation of some Imbrian craters in the 100 km diameter range as BBB craters implies that BBB populations on the Terra will exceed those on the maria; this is confirmed by the data in Fig. 6. However, at 10 km diameter, where only

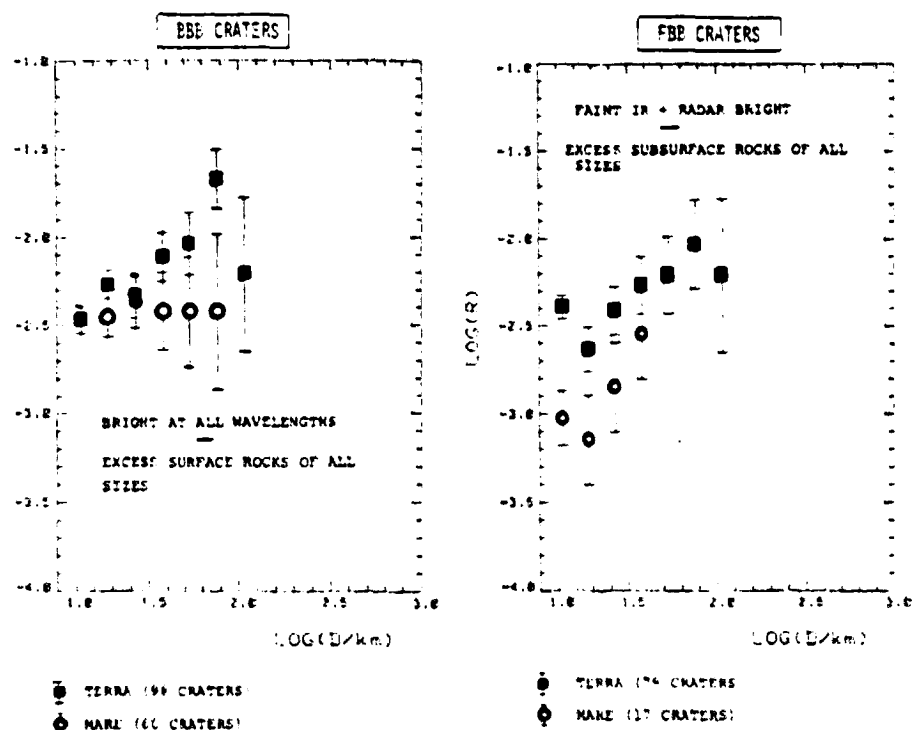


Fig. 6. Relative size-frequency distributions for the BBB and FBB craters. All of these craters except the Mare BBB show a size dependence different than the population of Imbrian and younger craters, which is approximately a horizontal line in these plots (Fig. 5a). Mare area was $4.4 \times 10^6 \text{ km}^2$; terra area was $5.4 \times 10^6 \text{ km}^2$.

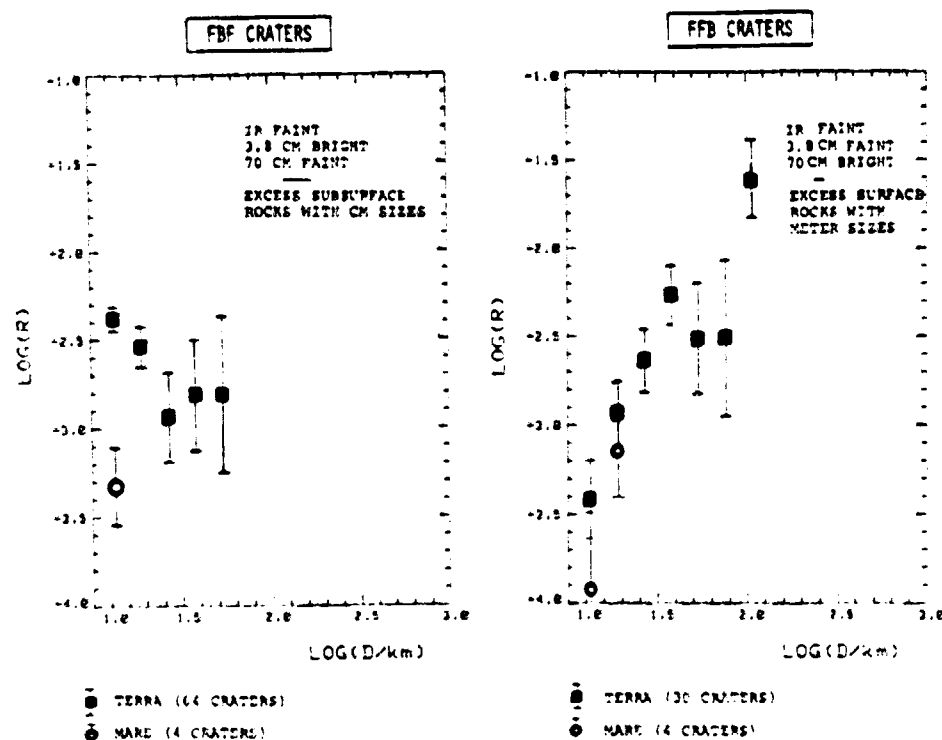


Fig. 7. Relative size-frequency distributions for the FBF and FFB craters. These craters occur primarily in the terra and have size dependences different than the population of Imbrian and younger craters, which would plot approximately as a horizontal line in these plots. Mare area was $4.4 \times 10^6 \text{ km}^2$; terra area was $5.4 \times 10^6 \text{ km}^2$.

Eratosthenian and younger craters are preserved as BBBs, we expect that BBB populations of mare and terra will be similar because all these BBBs formed since the maria. FBB craters are found on the maria with populations consistent with the hypothesis that smaller craters evolve faster than larger ones. All other crater classes are effectively absent on the mare. In addition, Fig. 8 shows that diameter distributions for all infrared and radar craters on the mare are nearly identical to the Copernican and Eratosthenian craters of Wilhelms *et al.* (1978). This suggests that there are few, if any, FFF craters on the mare with diameters greater than 12 km.

In summary, it appears that evolution of infrared and radar bright craters is size dependent. Smaller craters with diameters between 10 and 30 km tend to evolve from BBB to FBB to FBF to FFF craters. Larger craters with diameters larger than 30 km diameter tend to evolve from BBB to FBB to FFB to FFF craters. The ages associated with these crater classes are summarized in Table 3.

Table 2. Relative crater frequencies from linear least square fit to crater data.

Crater class	R(D)		R(D) × 10 ⁴		Least square fit
	[R(Imbrian and Younger)]				Chi-squared probability
	D=10 km	D=100 km	D=10 km	D=100 km	
Terra					
BBB	15.4%	66.6%	29.2	133.3	59.0%
Terra					
FBB	15.9%	26.4%	30.1	52.8	33.5%
Terra					
FBF	32.9%	1.4%	62.4	2.7	84.0%
Terra					
FFB	1.7%	57.8%	3.3	115.6	42.1%
Terra					
BBB + FBB + FBF + FFB	65.9%	152.2%	125.0	304.4	—
*Copernican & Eratosthenian	32.77%	31.6%	62.1	63.2	46.3%
*Imbrian & Younger	100.0%	100.0%	189.7	200.0	59.15%
*Nectarian & Younger	252.3%	375.7%	478.6	753.4	0.015%

* From Wilhelms *et al.* (1978)

DISCUSSION

To completely explain the formation and evolution of the infrared and radar signatures of craters is far beyond the scope of this paper. However, we will try to identify some possibly productive lines of future inquiry. Here we concentrate on explanations for (1) the typical behavior of large craters which have an evolution sequence BBB/FBB/FFB/FFF; (2) the typical behavior of small craters which evolve FBB/FBB/FFB/FFF; and (3) the faster rates of evolution of small craters. We will not discuss less common radar-infrared signatures.

First, it is useful to discuss how a typical terra region has evolved under the influence of impact gardening. Today, the terra has a uniform infrared and radar response, the end product of a deep gardening by impacting bodies. Except near very large craters which excavated bedrock beneath the megaregolith, the blocks now found at the surface and those mixed with finer debris to some depth are breccias and impact melts formed by the compaction and fusion of finer debris and smaller blocks by impacting events. Although the depth of the regolith continues to grow at a modest rate, the average size-frequency distribution of particles at shallow depths, less than a few tens of meters, has reached a steady state

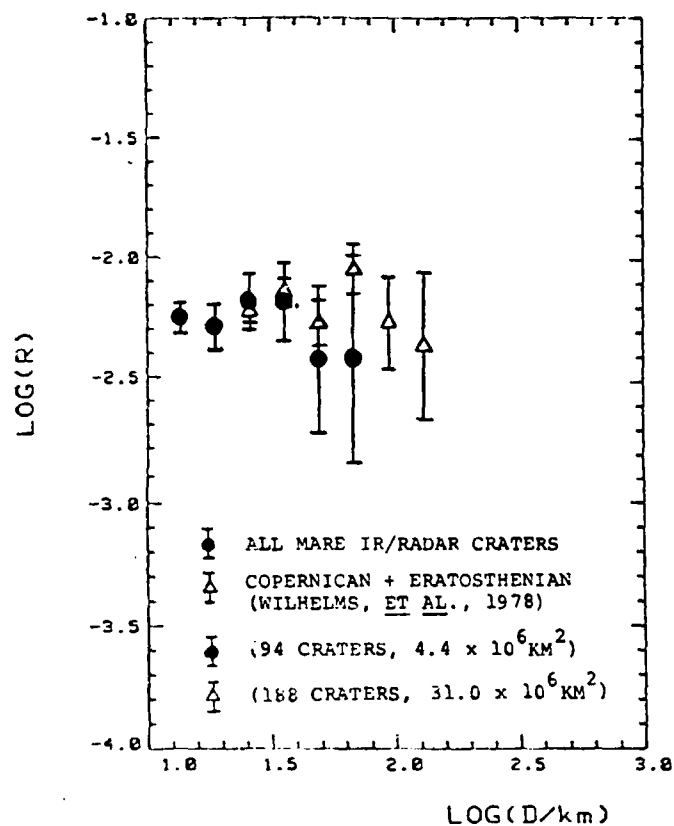


Fig. 8. Relative size-frequency distributions for all mare infrared/radar craters and (Copernican + Eratosthenian) craters of Wilhelms *et al.* (1978).

Table 3. Crater ages for IR-radar craters.

Crater class	Terra crater age	
	Smaller craters 10 km < diam. < 30 km	Larger craters 30 km < diam.
BBB	Copernican	Mostly Copernican and Eratosthenian; a few Imbrian
FBB	Eratosthenian	Imbrian
FBF	Imbrian	—
FFB	—	Mostly Imbrian; some pre-Imbrian

condition and the infrared and radar signatures of this surface have also reached steady state.

The formation of a large crater on the terra surface locally disturbs this steady state situation. An heterogeneous mix of blocks is excavated from depth and an impact melt is deposited on the floor of the pristine crater. Photogeological mapping and studies of the orbital infrared data show that the floors of large craters do not have uniform properties but are irregularly divided into units of distinct physical properties (Mendell and Low, 1975). We infer that older crater floors evolved from pristine floors primarily under the influence of impact gardening processes (Quaide and Oberbeck, 1975; Hörz *et al.*, 1975; Thompson *et al.*, 1974). However, endogenic processes may have been important, particularly for those craters that rim the maria and now constitute fractured floor craters (Schultz, 1976). Mass movement of debris from crater walls onto floors may have mantled the pristine surface (Mendell, 1976). Finally, ejecta from large basin-forming events such as Orientale and Imbrium have influenced the evolution of older craters (Moore *et al.*, 1974). All of these effects are potentially important in the evolution of the radar-infrared crater signatures.

How do the radar-infrared signatures of the floor of a pristine crater evolve under the action of impact gardening alone? Only some very qualitative ideas can be offered at present. First, initial conditions are important. If the floor is composed of a solidified impact melt then the signatures of the pristine surface and the subsequent evolution of the signatures may be different than if the floor is initially composed of debris. If the floor consists of a thin layer of impact melt overlying debris, still more complex patterns in the evolution of radar-infrared signatures can be expected.

Consider the evolution of a crater floor mantled with impact melt. The thickness of impact melt originally occupying the floor of large craters is dependent on crater diameter. Lange and Hawke (1979) show that the volume of impact melt generated is approximately $(1.8 \times 10^{-4}) D^{3.4} \text{ km}^3$ where D is crater diameter in kilometers. Some of this melt is deposited beyond the crater rim. The melt that remains in the interior of the crater probably occupies only a fraction of the crater floor. To first order, the thickness of the melt deposit on the floor of a crater can be estimated by assuming that the melt volume described above occupies a disk with diameter D . Thus, the depth of impact melt on the floor of a crater is $(0.28)D^{1.4}$ meters. Table 4 shows that this melt thickness will vary from 7 meters for a 10 km crater to 177 meters for a 100 km crater.

The radar-infrared signature of the melt will change in a complex manner as an impact regolith develops on it. Initially, the high thermal inertia of exposed impact melt will give rise to a strong thermal infrared contrast as reported by Schultz and Mendell (1978) for young craters such as Aristarchus and Olbers A. Next, the thermal signature will decline in response to comminution of the uppermost layer by small scale impact cratering. As the regolith gets deeper, large blocks of material generated by deeper cratering events into the impact melt may dominate the surface particle size distribution and re-enhance the thermal IR signature. The re-enhancement of the thermal signature, if real, has not been

Table 4. Predicted time scale for decay of radar anomalies as a function of crater diameter.

Crater diameter	Melt thickness (in meters)	Crater† age (by)	Regolith† depth (H_{med}) (in meters)	$\left(\frac{H_{med}}{T_m}\right)$	$\left(\frac{H_{med}}{D_{3.8}}\right)^*$	$\left(\frac{H_{med}}{D_{70}}\right)^*$	Predicted signatures	
							3.8 cm	70 cm
10	7.0	0.8	1.0–1.4	0.14	0.8	0.5	B	B
		3.55	4.8–5.7	0.7	4.0	0.24	F	B
		3.95	18.0–25.8	2.6	15.0	0.9	F	F
		4.2	43.5–105.0	6.2	36.0	2.2	F	F
30	26.8	0.8	1.0–1.4	0.04	0.8	0.05	B	B
		3.55	4.8–5.7	0.18	4.0	0.24	F	B
		3.95	18.0–25.8	0.67	15.0	0.9	F	B
		4.2	43.5–105.0	1.60	36.0	2.2	F	F
100	176.7	0.8	1.0–1.4	0.005	0.8	0.05	B	B
		3.55	4.8–5.7	0.03	4.0	0.24	F	B
		3.95	18.0–25.8	0.10	15.0	0.9	F	B
		4.2	43.5–105.0	0.25	36.0	2.2	F	F

† Relationship of age to regolith determined from data of Shoemaker and Morris (1970), Shoemaker *et al.* (1970), Boyce (1976), Boyce and Johnson (1977). Crater ages are 0.8 b.y. (Copernicus), 3.55 b.y. (Mare Tranquillitatis at Apollo 11), 3.95 b.y. (Imbrian ejecta blanket) and 4.2 b.y. (Nectarian ejecta blanket). These times can be crudely referenced to the geological periods used in the text: the Nectarian period starts at 4.2 b.y., the Imbrian at 3.95 b.y. and the Copernican Eratosthenian at about 3 b.y. The range of regolith depths cited reflects uncertainties in the estimates. We have used minimum values in our calculations.

* Penetration depth ($D_{3.8}$ and D_{70}) at 3.8 cm and 70 cm are assumed to be 1.2 m and 20 m respectively.

resolved in the thermal signatures that we have investigated. With further regolith development the block population of the surface layers of the regolith will decline as new blocks from the substrate are excavated less frequently.

The radar scattering from pristine impact melt would be expected to be small initially but to increase rapidly as blocks are produced by impact cratering. As the regolith thickens, the decline in the block population at the surface will be followed by a decline just beneath the surface. In a very thick regolith, the material in the upper layers will be reduced to the steady state condition. Consequently, an early decline in the infrared signature will be followed by a decline in the 3.8 cm signatures and finally a fall in the 70 cm signature (see Fig. 3).

We expect that the evolution of the radar signature, the contrast between the crater floor and the surrounding terra, will depend in part on the thickness of the melt layer. In small craters, the depth of the regolith formed on the crater floor may exceed the impact melt thickness and will entirely destroy the coherent structure of the melt layer. In addition, Gault *et al.* (1974) show that material buried at depths significantly shallower than the median regolith depth will be turned over many times during the history of that surface. Consequently, rocks derived from the destruction of an impact melt layer by a deep regolith will be

returned to the surface frequently where they are rapidly destroyed. As a result the radar signature from a small crater floor originally mantled by impact melt will disappear when the median regolith thickness is a few times the melt thickness.

In a larger crater, by contrast, the impact melt is so thick that it can survive impact gardening for all post-Imbrian to post-Nectarian time; thus, fresh rocks will continue to be broken away from the impact melt. However, those within 10 meters or so of the surface will be destroyed in the manner described above. Consequently, the radar signature will again disappear as the regolith deepens, but the time scale for the signature to disappear will depend on the radar penetration depth and not on the thickness of impact melt.

In Table 4 we have attempted to assemble these ideas into a crude prediction of the time scale for decay of the radar anomalies. Regolith depths have been estimated from crater diameter-frequency curves using a model relationship between the diameter (C_c) of change in slope of the curve (Boyce and Johnson, 1977) and the median regolith depth determined from various theoretical and experimental studies (Shoemaker *et al.*, 1970; Quaide and Oberbeck, 1975). The relationship between impact melt thickness (T_m), median regolith depth (H_{med}), and radar penetration depths at 3.8 cm and 70 cm ($D_{3.8}$ and D_{70}) is characterized by three ratios (H_{med}/T_m , $H_{med}/D_{3.8}$, and H_{med}/D_{70}). Radar signatures disappear when either H_{med}/T_m exceeds two, or the other ratios exceed unity. Craters as young as Copernicus will have very shallow regoliths and still preserve the 3.8 cm signatures. In the case of the 70 cm signatures, there is a dependence on size and age. The small craters are radar bright until the regolith development as reflected in the index (H_{med}/T_m) comminutes the layer of impact melt. For very large craters (H_{med}/T_m) is always less than unity and the radar penetration depth is important. Assuming (H_{med}/D_{70}) = 1 denotes the change from a bright crater to a faint crater, then there are still some large pre-Imbrian craters that are bright, in agreement with our observations.

The premature loss of the 70 cm signature and the accompanying extended survival of 3.8 cm signatures in the small FBF craters is not explained by the model just described. One possibility is that impact melt is not exposed on the crater floor. Lange and Hawke (1979) report that many impact craters in the size range 15 to 30 km show no photogeological evidence of impact melt in the crater floor. They cite evidence for mantling of the melt layer, by material derived from wall slumping. They also point out that in larger craters this mantling process is not as effective, although Mendell (1976) feels that wall slumping is an important floor modifier for all craters. Possibly, the debris layers that mantle the floors of the smaller craters are dominated by centimeter-sized particles which provide a strong 3.8 cm radar signature but no 70 cm signature.

It may also be possible to account for the occurrence of FBF craters purely in terms of impact gardening. Conceivably, the particle size distributions in some phases of regolith development are dominated by the small blocks resulting in an FBF signature. To seriously evaluate these various possibilities it is necessary to quantitatively model the evolution of particle sizes in all phases of regolith

development using techniques such as those developed by Quaide and Oberbeck (1974), Housen *et al.* (1979), and Langevin and Arnold (1977). In addition, a model for predicting the diffuse radar scattering from fragmental debris layer is needed.

SUMMARY

A comparison of the statistics of the infrared and radar bright craters on the terra with the statistics for craters assigned to different geologic epochs, has provided insights into the evolution of rock populations in the first few meters of the lunar subsurface. The statistics for the infrared and radar craters are consistent with the following evolution: (I) Craters are formed as BBB (bright at all wavelength) craters with excess populations of surface and subsurface rocks. (II) BBB craters evolve to FBB (faint IR, bright radar) craters with average surface rocks and excess subsurface rocks of all sizes. (III) FBB craters evolve further to either FBF or FFB craters, which have enhanced radar signatures at only one radar wavelength. These FBF and FFB craters have excess subsurface rocks of either centimeter or meter sizes. (IV) FBF and FFB craters evolve finally to the FFF crater which is faint at all wavelengths and has no excess surface or subsurface rocks.

These infrared and radar signatures evolve with different rates and along different paths depending upon crater size. Smaller craters with diameters of 10 to 30 km evolve primarily to FBF craters, while larger craters with diameters of 30 km and larger evolve primarily to FFB craters. In addition, smaller craters evolve faster than larger craters. The association of these infrared and radar bright craters with various geologic epochs is given in Table 3.

The initial conditions and subsequent evolution of radar-infrared crater signatures of the crater floors depends upon a number of lunar surface processes, including impact melt generation, debris blanketing, impact gardening, and crater wall collapse. We investigated the initial formation and subsequent gardening on an impact melt as one possible evolution scenario. This yielded an evolution of BBB to FBB to FFB to FFF craters which was size-dependent and agreed with the crater ages derived from the large crater statistics. However, this failed to predict the evolution through the FBF class observed for smaller craters. Clearly, we need to develop more quantitative descriptions of the evolution of particle sizes in regoliths and of the radar signatures corresponding to the various stages of evolution. Further studies along these lines could enable us to use radar and infrared signatures as a tool for understanding how various surface processes affected the lunar highland crust.

Acknowledgments—The catalog of infrared and radar craters used here was originally compiled by Wm. James Roberts of the Planetary Science Institute. The generation of this catalog relied heavily upon the infrared and radar images of the moon generated by the NASA Apollo Experiment S-217. Ms. Amelia Vetrone generated the crater statistic plots. Reviews by Fred Hörz and Peter Schultz provided many improvements to this paper. The work reported here was funded by NASA Contract NASW 3205.

REFERENCES

- Arthur D. W. G., Agnieray A. G., Horvath R. A., Wood C. A., and Chapman C. R. (1963) The system of lunar craters, Quadrant I. *Commun. Lunar and Planetary Lab., Univ. Arizona* 2, 71-78.
- Arthur D. W. G., Agnieray A. G., Horvath R. A., Wood C. A., and Chapman C. R. (1964) The system of lunar craters, Quadrant II. *Commun. Lunar and Planetary Lab., Univ. Arizona* 3, 1-2.
- Arthur D. W. G., Agnieray A. G., Pellicori R. H., Wood C. A., and Weller T. (1965) The system of lunar craters, Quadrant III. *Commun. Lunar and Planetary Lab., Univ. Arizona* 3, 61-62.
- Arthur D. W. G., Pellicori R. H., and Wood C. A. (1966) The system of lunar craters, Quadrant IV. *Commun. Lunar and Planetary Lab., Univ. Arizona* 4, 1-2.
- Boyce J. M. (1976) Ages of flow units in the lunar nearside maria based on Lunar Orbiter 14 photographs. *Proc. Lunar Sci. Conf. 7th*, p. 2717-2728.
- Boyce J. M. and Johnson D. A. (1977) Ages of flow units in Mare Crisium based on crater data. *Proc. Lunar Sci. Conf. 8th*, p. 3495-3502.
- Crater Analysis Group (1979) Standard techniques for presentation and analysis of crater size-frequency data. *Icarus* 37, 467-474.
- Gault D. E., Hörz F., Brownlee D. E., and Hartung J. B. (1974) Mixing of the lunar regolith. *Proc. Lunar Sci. Conf. 5th*, 2365-2386.
- Hörz F., Schneider E., Gault D. E., Hartung J. B., and Brownlee D. E. (1975) Catastrophic rupture of lunar rocks: A Monte Carlo simulation. *The Moon* 13, 235-258.
- Housen K. R. and Wilkening L. L., Chapman C. R., and Greenberg R. (1979) Asteroid regoliths. *Icarus* 39, 317-351.
- Lange M. A. and Hawke B. R. (1979) The generation of lunar impact melts: A comparison of theoretical and observational results (abstract). In *Papers Presented to the Conference on the Lunar Highlands Crust*, p. 98-100. Lunar and Planetary Institute, Houston.
- Langevin Y. and Arnold J. R. (1977) The evolution of the lunar regolith. *Ann. Rev. Earth Planet. Sci. Lett.* 5, 449-489.
- Mendell W. W. (1976) Degradation of large, Period II lunar craters. *Proc. Lunar Sci. Conf. 7th*, p. 2703-2716.
- Moore H. J., Hodges C. A., and Scott D. H. (1974) Multiring basins—illustrated by Orientale and associated features. *Proc. Lunar Sci. Conf. 5th*, p. 71-100.
- Quaide W. and Oberbeck V. (1975) Development of the mare regolith: Some model considerations. *The Moon* 13, 27-55.
- Schultz P. H. (1976) Floor-fractured lunar craters. *The Moon* 15, 241-273.
- Schultz P. H. and Mendell W. (1978) Orbital infrared observations of lunar craters and possible implications for impact ejecta emplacement. *Proc. Lunar Planet. Sci. Conf. 9th*, p. 2857-2883.
- Shoemaker E. M. and Morris E. C. (1970) Physical properties of the lunar regolith determined from Surveyor television observations. *Radio Sci.* 5, 129-155.
- Shoemaker E. M., Hait M. H., Swann G. A., Schleicher D. L., Schaber G. G., Sutton R. L., Dahlen D. H., Goddard E. N., and Waters A. C. (1970) Origin of the lunar regolith at Tranquility Base. *Proc. Apollo 11 Lunar Sci. Conf.*, p. 2399-2412.
- Shorthill R. W. (1973) Infrared atlas charts of the eclipsal moon. *The Moon* 7, 22-45.
- Thompson T. W. (1974) Atlas of lunar radar maps at 70 cm wavelength. *The Moon* 10, 51-85.
- Thompson T. W., Masursky H., Shorthill R. W., Tyler G. L., and Zisk S. H. (1974) A comparison of infrared, radar and geologic mapping of lunar craters. *The Moon* 10, 87-117.
- Thompson T. W., Masursky H., Shorthill R. W., and Zisk S. H. (1979) Blocky craters: Implications about the lunar megaregolith. *Moon and Planets* 21, 319-342.
- Wilhelms D. E., Oberbeck V. R., and Aggarwal H. R. (1978) Size-frequency distributions of primary and secondary lunar impact craters. *Proc. Lunar Planet. Sci. Conf. 9th*, p. 3735-3762.
- Zisk S. H., Pettengill G. H., and Catuna G. W. (1974) High resolution radar map of lunar surfaces of 3.8 cm wavelength. *The Moon* 10, 17-50.

APPENDIX D

Abstracts from:

DPS Meeting
Tucson, Arizona
14-17 Oct. 1980

and

LPSC Meeting
Houston, Texas
16-20 March 1981

Lunar Craters with Radar-Bright Ejecta,

T. THOMPSON, Plan. Sci. Inst., S. ZISK, NEROC Haystack Obser., R. SHORTHILL, Univ. of Utah Res. Inst., P. SHULTZ, Lunar and Plan. Inst., J. CUTTS, Plan. Sci. Inst. - Some 120 lunar craters with diameters between 1 and 64Kms are surrounded by ejecta which has strong radar echoes at 3.8cm wavelength. The bright radar haloes are up to twenty times the diameter of the central crater. Most crater ejecta deposits with these characteristics have no similar 70cm radar enhancement. Some have warmer eclipse temperatures, others do not. Many of them have full moon rays, but some do not. Significantly, craters with the 3.8cm ejecta enhancement occur equally frequently in mare and terra but are only 1% of the abundance of the photogeologically determined mare population. We interpret this crater population as a steady-state population reflecting a balance between the production of new craters with radar bright ejecta deposits and the obliteration of the radar bright ejecta signatures of older craters by meteoritic gardening. Craters with an IR ejecta enhancement appear to be a subset steady population comprized of still younger craters and established by more rapid degradation of the ejecta signature. For both the IR and 3.8cm radar populations rate of evolution appears to be size dependent. Ages have been inferred for craters using expected impacting rates for Apollo-Amor objects over the last 10^7 to 10^9 years. Implications for regolith gardening processes are also examined.

Radar Craters on Venus: A steady state population. J.A. CUTTS, T.W. THOMPSON, B.H. LEWIS, Planet. Sci. Inst., - Images of the surface of Venus acquired with the Arecibo observatory (Campbell et al.) reveal bright ring-shaped structures which have been interpreted as possible impact craters (Science 193 1424-1424). From more recent studies of these (Pettin-gill et al., Scientific American 243, No. 2, 53-65, 1980, Campbell and Burns, J. Geophys. Res. in press) it has been concluded that Venus has more extensive crater ejecta deposits than does the Moon, Mercury or Mars and that the crater population is small and consistent with a surface only 600 million to 1 billion years old. We have performed a comparison of the ring features in the Venus radar imagery and the appearance and populations of radar signatures of lunar craters. Ring widths in the Venus crater is found to be comparable to the radar width of fresh large lunar craters. However, the floors of fresh lunar craters are comparable bright to the ejecta and so lunar radar craters do not have a ring-shaped appearance. The populations of lunar radar craters are in a steady state because of the destruction of the radar signature by meteoroidal bombardment. We have investigated the possibility that Venus radar crater populations are also in a steady state established by planet wide deposition of a fraction of the material ejected by large impact craters. This model would not require widespread re-surfacing of Venus to have occurred less than a billion years ago. We have performed a Monte Carlo simulation of the process and we find that it requires approximately 1% of the material excavated to be distributed globally for the observed Venus crater populations to be reproduced. Examples of the Monte Carlo models are presented and discussed.

YOUNG LUNAR CRATER EJECTA CHARACTERISTICS FROM RADAR, INFRARED AND VISUAL OBSERVATIONS: T.W. Thompson and J.A. Cutts, Planetary Science Inst., Pasadena, CA 91101; P.H. Schultz, Lunar and Planetary Inst., Houston, TX 77058; R.W. Shorthill, Univ. of Utah Research Inst., Salt Lake City, UT 84108; and S.H. Zisk, NEROC Haystack Obs., Westford, MA 01886

ABSTRACT: A small fraction of lunar craters with diameters between 1 and 20 kilometers have haloes of extensive enhanced 3.8cm radar echoes associated with their ejecta. The physical properties of these ejecta have been characterized via various infrared, radar and visual observations. These haloes have little or no 70cm radar enhancements and this implies that the 3.8cm radar enhancements arise primarily from centimeter-sized roughness associated with small rocks and blocks. In some cases these haloes have strong infrared signatures while others do not. Strong infrared signatures imply large numbers of surface rocks.

These craters with 3.8cm radar occur less frequently than post-mare craters. Comparison of size-frequency distributions with lunar mare distributions suggests that the age of these craters with radar bright haloes are 1.3 to 3.3×10^8 years. Craters with strong infrared signatures are on the order of 10^7 years. These ages are consistent with predicted rates for the breakdown of blocks and the reworking of the lunar regolith and the production of craters from Apollo-Amor objects.

INTRODUCTION: The first resolution radar maps of the moon obtained in the 1960's showed a number of bright haloes which had diameters ten to twenty times that of the central crater. Eighteen of these interesting features were studied by Thompson et al. (1974). They showed that these haloes were likely strewn fields of centimeter-sized rubble based upon an absence of a bright 70cm radar halo.

This report describes a systematic study of these craters. Some 120 of these craters have been cataloged for that portion of the earth-visible lunar surface which is covered by the currently available LAC charts. More detail on this study is given by Thompson et al. (1980), who used earth-based infrared and 70cm radar observations as complements to the 3.8cm radar observations. This use of remote observations to deduce crater ejecta characteristics follows that of Schultz and Mendell (1978), who studied the crater Aristaschus and a number of small mare craters in Oceanus Procellarum.

RADAR-BRIGHT HALO CRATER CATALOG: The 120 craters with 3.8cm radar bright haloes were selected solely upon their sizes in 3.8cm radar images of the moon (Zisk et al. 1974). The halo size had to be 20km or greater for smaller craters (with diameters less than 10km) or the halo size had to be twice the crater diameter for larger craters (with diameters larger than 10 kilometers). The 20km limit was chosen so that these haloes were covered by a few resolution cells in the earth-based 70cm and infrared eclipse observations described by Thompson (1974) and Shorthill (1973). The limit of having 3.8cm radar haloes being twice the crater diameter concentrated our attention on

LUNAR CRATER EJECTA FROM RADAR OBS.

Thompson, T.W. et. al.

craters with diameters between one and twenty kilometers with a few examples of young craters up to 45 kilometers in diameter.

Some of the cataloged crater characteristics include size and peak strength in the earth eclipse temperature, 3.8cm and 70cm radar images. Crater sizes were taken from the LPL Catalog or Lunar Orbiter IV photographs. The size of bright albedo areas in full moon and Lunar Orbiter IV photographs were also cataloged.

BRIGHT-HALO CRATER CHARACTERISTICS: The remotely sensed signatures for these craters can be summarized as follows. As expected, the 3.8cm sizes and strengths were large. The ratio (3.8cm halo diameter/crater diameter) was as large as 20 to 40 for smaller craters with diameters less than 4kms. The 70cm radar images showed no haloes for craters smaller than about 10kms while some larger craters had extensive haloes. The 70cm radar strengths were consistent with a model where the strong echoes were confined to crater interior and rim wall. The 70cm radar signatures were similar to orbital infrared signatures (this is expected since they respond to similar rock sizes).

Eclipse infrared signals showed a range of responses. In some cases, the stronger infrared signatures were consistent with haloes which were approximately half as large as the 3.8cm images. In other cases, the weaker infrared signatures were consistent with a model where the infrared enhancement was confined to the crater interior. Some 38 craters with diameters less than 8 kilometers had the strong signatures while the remaining 82 craters had weaker earth-based infrared responses.

These craters also had a range of visual responses in full moon and Lunar Orbiter IV photographs. Most craters had bright haloes extending beyond the crater in the full moon photographs. Surprisingly, a few craters had bright full moon albedos confined to the crater interior. A few craters, like Moltke and Copernicus H, had dark haloes in the full moon photographs. And, as expected, several of these craters had bright albedo haloes in the low-sun Lunar Orbiter IV photographs.

These remote sensing signatures combined with high resolution lunar surface photography (Schultz, 1976) suggests that crater ejecta size changes with crater size and range from the central crater. Smaller craters with sizes of 1 to 2 kilometers have abundant meter-sized blocks in their ejecta out to about 5 crater radii while smaller centimeter-sized blocks occur at ranges of 5 to 20 or 40 crater radii. Larger craters with diameters from 1 to 2 kilometers to about 10 kilometers have abundant meter-sized blocks in the near rim regions out to only about 0.5 crater radii. For these larger craters, there appears to be a inner zone out to about 5 crater radii where there are abundant blocks up to a few tens of centimeters in size and an outer zone beyond 5 crater radii up to about 10 or 20 crater radii where centimeter-sized blocks are abundant.

AGE RELATIONSHIPS: The size-frequency distributions for these craters provide further insights into these craters. In particular, we compared the size-frequency distributions of the craters with 3.8cm radar bright haloes with a size-frequency distribution for craters in Oceanus Procellarum with ages of

LUNAR CRATER EJECTA FROM RADAR OBS.

Thompson, T. W. et al.

3.3 By. For craters with diameters of 4 kilometers, the radar bright halo craters occur 25 times less frequently, suggesting an age of 1.3×10^8 years. Similarly, for craters with diameters of 32 kilometers, the radar bright halo craters occur 10 times less frequently suggesting an age of 3.3×10^8 years. Those craters with large infrared sizes and strengths occur even less frequently suggesting ages of 10^7 years for these craters.

These age determinations suggest that the craters with radar bright haloes may be a steady-state population reflecting a balance between the production of fresh craters and the destruction of the infrared and radar signatures by small scale cratering. The ages of craters given above are consistent with models for surface rock breakdown by Hbrz et al. (1974) and regolith gardening by Gault et al. (1974). Also, large craters appear to have longer lifetimes. In addition, the number of craters with radar bright ejecta is near that predicted for impacts by Apollo-Amor objects in 10^7 to 3×10^8 years using the formula given by Shoemaker (1977).

SUMMARY: Various remote sensing signatures at infrared, radar and visual wavelengths suggest that young lunar craters with diameters between 1 and about 10 kilometers have ejecta which has abundant centimeter-sized blocks and which extends beyond the crater by many crater radii. Abundant meter-sized ejecta is confined to the near rim regions and extends no further than 0.5 crater radii for craters with diameters greater than 2 kilometers and may extend up to about 5 crater radii for craters with diameters of 1 kilometer. The numbers of these craters suggest that extensive 3.8cm radar haloes have ages on the order of 1.3 to 3.3×10^8 years. Similarly, craters with extensive infrared haloes have ages of about 10^7 years. These ages are consistent with models for lunar surface processes and predictions for impacts by Apollo-Amor objects in these time periods.

ACKNOWLEDGEMENTS: Crater population data for the lunar maria was provided by W.K. Hartmann. A portion of this research was done while two (R.W.S. and T.W.T.) were Visiting Scientists at the Lunar and Planetary Inst., which is operated by Universities Space Research Assoc. under Contract No. NSR-09-051-001 with NASA. Two of us (T.W.T. and J.A.C.) were funded in part by NASA Grant NASW 3383.

REFERENCES:

- Gault, D.E. et al. (1974) Proc. Lunar Sci. Conf. 5, p.2365-2388.
 Hbrz, D.E. et al. (1974) The Moon 13, p. 235-258.
 Schultz, P.H. (1976) Moon Morphology, Univ. of Texas Press.
 Schultz, P.H. & Mendell, W. (1978) Proc. Lunar Sci. Conf. 9, p. 2857-2883.
 Shoemaker, E.M. (1977) in Impact & Explosion Cratering, Pergamon Press, p. 617-628.
 Shorthill, R.W. (1973) The Moon 7, p. 22-45.
 Thompson, T.W. (1974) The Moon 10, p. 51-85.
 Thompson, T.W. et al. (1974) submitted to Icarus.
 Zisk, S.H. et al. (1974) The Moon 10, p. 17-50.

APPENDIX E

CRATER CATALOGS ON SAI'S DEC-10 COMPUTER

Study of the infrared and radar behaviors of lunar craters is facilitated by computerized crater catalogs on SAI's DEC-10 computer in La Jolla. These catalogs can be queried via a telephone modem located in our Pasadena office.

There are two crater catalogs - one catalog of 120 craters was generated via the LPI Visiting Scientist Study. This catalog was carefully checked against the original data sets before it was committed to a computer disk data set. The other catalog of 1310 craters was originally generated as a computer deck via the Megaregolith Study. This catalog was improved by adding a basin index describing whether mare craters were in a basin or in an irregular mare (i.e. in deep or thin mare). Also, the Lunar Orbiter IV photographs for these 1310 craters were computed in order to provide rapid searches for photographs of these craters.

Both catalogs have a common goal of having selenographic, radar-infrared and photogeological descriptors for the lunar craters, as shown in Table D-1. These descriptors can be divided into three classes: (1) general selenographic information, (2) IR and radar characteristics, and (3) photogeologic indices. Each of these classes are described below.

The general selenographic information for a lunar crater includes LPL catalog number, name, position and diameter. Position is given in either latitude and longitude or the direction-cosines X_s , Y_s , Z_s ($X_s = \sin(\text{lon}) \cos(\text{lat})$, $Y_s = \sin(\text{lat})$, $Z_s = \cos(\text{lon}) \cos(\text{lat})$). These direction cosines are useful for deriving a number of supplementary items. For example, angle of incidence for earth-based observations is approximately $\arccos(Z_s)$.

The IR and radar signatures of lunar craters provides a second class of information. The most important data is the IR and radar strengths for the crater interiors. In addition to strengths, other IR/radar specific data includes ZAC (3.8cm radar) map numbers, LAC (70cm) map numbers and angle of incidence.

Various photogeological indices provides a third class of information. These include ages derived either from the LPL catalog or the USGS maps, as well as various information about photography (either Apollo, Lunar Orbiter or full-moon plates from the Consolidated Lunar Atlas).

Specific implementations of these general goals is given in Tables D-2 and Table D-3. The lunar basin index in the 1310 crater catalog was computed using the parameters shown in Table D-4.

TABLE E-1: OVERVIEW OF LUNAR IR/RADAR CRATER DATA BASESI. General Selenographic Information

LPL Number

Crater Name

Crater Position (latitude and longitude)

Crater Position (direction cosines, Xs, Ys, Zs)

II. IR/Radar Data

Strengths (IR, 3.8cm, 70cm)

Sizes (IR, 3.8cm, 70cm)

Map Information (LAC number, ZAC number)

Bright Ejecta Index = Fuzzy Index

Angle of Incidence

IR Resolution

III. Photogeologic Indices

Ages (LPL and USGS)

Background = Mare/Terra Index

= Basin Index

LPL Class

Full-Moon Appearance

Fractured-Floor Index

Depth-to-Diameter Ratio

Detailed Study Index

LO IV Photo Information (plate/position)

Apollo Photo Index

Consolidated Lunar Atlas Information
(for full-moon photos)

TABLE E-2: FORMAT FOR FCAT. DATA

LINE	VARIABLE	FORMAT	DESCRIPTION
1	LPLN	I6	LPL catalog number
	CNAME(16)	3X,30A1	Crater name
	DLON	3X,F6.2	Longitude (In DEG.)
	DLAT	F6.2	Latitude (In DEG.)
	DIAM	F6.2	Diameter (In KMS)
	XS	F6.3	Dir. cosine XS= $\cos(\beta) \sin(\lambda)$
	YS	F6.3	Dir. cosine YS= $\sin(\beta)$
	ZS	F6.3	Dir. cosine ZS= $\cos(\beta) \cos(\lambda)$
2	LPLN	I6	LPL number
	IDIR	I6	IR Diam. (kms)
	ID38	I6	3.8cm Diam. (kms)
	ID70	I6	70cm Diam. (kms)
	ISIR	I6	IR strength
	IS38	I6	3.8cm strength
	IS70	I6	70cm strength
	HSTAR	1X, 4S	IR bright index
	LACN	I6	LAC chart number
	NUMZAC	I6	Number of ZAC charts
	ZACN(4)	4F6.2	ZAC chart numbers
3	LPLN	I6	LPL number
	NUMLO4	I6	Number of Lunar Orbiter-IV prints
	LO4PP(20)	5(I4,1HH, I1, I4, A1, I2, 5X)	Lunar Orbiter-IV photo info LO4PP(1,6,etc.)=Frame # LO4PP(2,7,etc.)=1,2, or 3 LO4PP(3,8,etc.)=Atlas Page # LO4PP(4,9,etc.)=A→M Located LO4PP(5,10,etc.)=1→16 Index

TABLE E-2 (Cont'd)

LINE	VARIABLE	FORMAT	DESCRIPTION
4	LPLN	I6	LPL number
	LAGE	I6	LPL catalog age
	LCCASS	A6	LPL catalog description
	HBACK	A6	Crater background (' mare' or 'terra')
	HMT	A6	Mare/Terra Index (M or T)
	NMAP	I6	Number of Apollo missions
	MAP(3)	3I6	Apollo missions
	1DFM		Size in full moon
	1DLO4		Lunar Orbiter-IV ray size
5	LPLN	I6	LPL number
	IOUT	I6	Catalog entry numbers
	COM(30)	3X,30A1	Comments
	NUMCAT	3X, I6	Number of consolidated Lunar Atlas plates
	IPCAP(8)	4(3X,A1,I2)	Consolidated Lunar Atlas Plate numbers
			IPCAP(1,3,etc.)=A thru H IPCAP(2,4,etc.)=1 thru 6

Notes: (1) Formats are Modulo-6

(2) FCAT. DAT has 120 entries

TABLE E-3: PIRC3.TWT FORMAT

LINE	VARIABLE	FORMAT	DESCRIPTION
1	LPLN	I6	LPL Number (NUMERIC)
	LPLA	A1	LPL Number (ALPHA)
	CNAME(16)	1X,16A1	Crater Name
	DLON	F6.1	Crater Longitude (DEG.)
	DLAT	F6.1	Crater Latitude (DEG.)
	DIAM	F6.2	Crater Diameter (KMS)
	XS	F6.3	Dir. cosine XS = $\cos(\beta)\sin(\lambda)$
	YS	F6.3	Dir. cosine YS = $\sin(\beta)$
	ZS	F6.3	Dir. cosine ZS = $\cos(\beta)\cos(\lambda)$
	ICC	I6	Catalog Entry Number
2	LPLN	I6	LPL Number
	INIR	I6	IR Strength Index
	IN38	I6	3.8cm Radar Strength Index
	IN70	I6	70cm Radar Strength Index
	H1,H2,H3	3X,3A1	IR/Radar Index (FFF+BBB)
	S	F6.2	Normalized Strength
	LACN	I6	LAC Chart Number
	ZACN	F6.2	ZAC Chart Number
	ANGINC	F6.1	Angle of Incidence
	HF	5X,A1	Fuzzy Index (F = FUZZY)

TABLE E-3 (Continued)

LINE	VARIABLE	FORMAT	DESCRIPTION
3	LPLN	I6	LPL Number
	LAGE	I6	LPL Age Class
	HMT	5X,A1	Mare/Terra Index (M or T)
	HBASIN(2)	2A6	Basin Indices
	DDRAT	F6.3	Depth/Diam. Ratio
	FFIND	A6	Fractured Floor Index
	FMIND	A6	Full-Moon Index
	DSIND	A6	Detailed Study Index
4	LPLN	I6	LPL Number
	NLOPIC	I6	Number of Lunar Orbiter IV Photos
	4(PIC ID's)	4(3X,I3, 1HH,I1,	Frame Number, subframe number (1, 2 or 3)
		1H,A1,I2)	Atlas Page Number Atlas Position Index (A-G) Atlas Position Index (1-12)

- NOTES: (1) Most variables have formats MODULO 6.
 (2) Variable HF is unreliable (does not correspond to fuzzy catalog).
 (3) The following variables are currently undefined:
 DDRAT & FFIND &
 FMIND & DSIND
 (4) Variables HBASIN is either 'TMARE' or 'TERRA' if outside all basins.
 (5) PIRC3.TWT has 1310 entries.

TABLE E-4: BASIN CHARACTERISTICS

BASIN	RADIUS (km)	LONG. CENTER	LAT. CENTER	COMPUTER NAME	COMPUTER INDEX
Orientale	195 310	-95.0	-20.0	ORIEN	1
Imbrium	335 485	-19.0	+37.0	IMBRM	2
Crisium	225 335	+59.0	+17.0	CRISM	3
Humorum	210 280	-39.0	-24.0	HUMOR	4
Nectarus	200 300	+34.0	-16.0	NECTR	5
Serenitatis	155 340	+19.0	+26.0	SEREN	6
Fecunditatis	120 120	+51.0	- 3.0	FECUN	7
Tranquillitatis (West)	140 140	27.0	9.0	TWEST	8
Tranquillitatis (East)	120 120	38.0	11.0	TEAST	9
Nubium	180 180	-17.0	-19.0	NUBUM	10